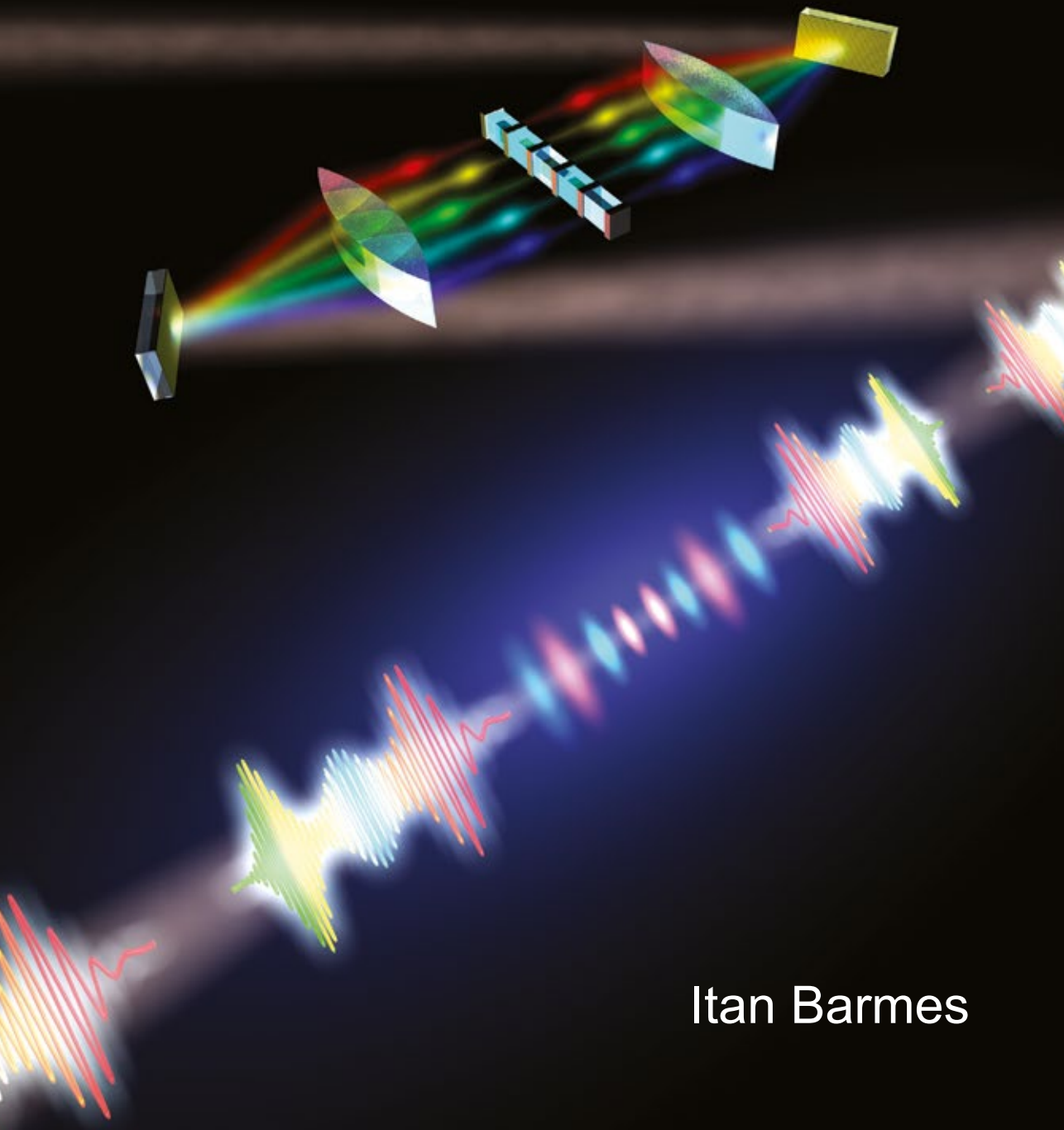


Coherent control and high-precision spectroscopy with an optical frequency comb



Itan Barmes

Coherent control and
high-precision spectroscopy
with an optical frequency
comb

VRIJE UNIVERSITEIT

**Coherent control and high-precision
spectroscopy with an optical frequency comb**

ACADEMISCH PROEFSCHRIFT

ter verkrijging van de graad Doctor aan
de Vrije Universiteit Amsterdam,
op gezag van de rector magnificus
prof.dr. V. Subramanian,
in het openbaar te verdedigen
ten overstaan van de promotiecommissie
van de Faculteit der Exacte Wetenschappen
op donderdag 8 juni 2017 om 11.45 uur
in de aula van de universiteit,
De Boelelaan 1105

door

Itan Barmes

geboren te Rehovot, Israël

promotor: prof.dr. K.S.E. Eikema
copromotor: dr. S.M. Witte

Believe what you like, but don't believe everything you read without questioning it.

Pauline Baynes

This thesis was reviewed by the members of the reviewing committee:

Prof. Dr. T. Baumert	(University of Kassel)
Prof. Dr. J.L. Herek	(University of Twente)
Prof. Dr. H.B. van Linden van den Heuvell	(University of Amsterdam)
Prof. Dr. P.J.G. Mulders	(Vrije Universiteit Amsterdam)
Dr. L. Willmann	(University of Groningen)



The work described in this thesis was performed as part of the research program of the Netherlands Organization for Scientific Research (NWO) and was carried out at the LaserLaB, Vrije Universiteit, Amsterdam. Investment support was provided by the EC's Seventh Framework Programme LASERLAB EUROPE and the Foundation for Fundamental Research on Matter (FOM).

The cover shows an illustration of a pulse shaper, a device that was heavily used in the work leading to this thesis. In the back there are two camera images of the fluorescence emitted by Rb atoms when excited by counterpropagating shaped frequency comb laser pulses.

Printed by: Ipskamp Printing, Enschede
ISBN: 978-94-028-0639-7

Contents

1	Introduction	1
1.1	Precision spectroscopy	2
1.2	Coherent quantum control	3
1.3	Frequency comb lasers	4
1.4	Coherent control with frequency combs	6
1.5	Outline of this thesis	7
2	Theoretical background	9
2.1	Propagation of electromagnetic waves in vacuum	10
2.2	Propagation in transparent media	11
2.3	Properties of ultrashort pulses	12
2.4	Spectral phase shaping	15
	Linear spectral phase	16
	Quadratic spectral phase	16
	Sinusoidal spectral phase	17
	V-shaped spectral phase	20
2.5	From pulse pairs to frequency combs	21
2.6	Light-matter interaction	26
3	Coherent control with pairs of shaped pulses	29
3.1	Introduction	30
3.2	Experimental Setup	30
3.3	Single pulse excitation	32
	Nonresonant TPA	33
	Resonant TPA	34
3.4	Double-pulse excitation	37
	Nonresonant double-pulse TPA	38
	Resonant TPA	42
3.5	Conclusion	44

4	High-precision spectroscopy with counterpropagating femtosecond pulses	45
4.1	Introduction	46
4.2	Setup	47
4.3	Background reduction	48
4.4	Counterpropagating excitation	50
4.5	Spectroscopy and systematic effects	53
4.6	Conclusion	55
5	Spatial and spectral coherent control with frequency combs	57
5.1	Introduction	58
5.2	Theory	58
5.3	Setup	60
5.4	Spatial control with sinusoidal phase modulation	60
5.5	Spatial selectivity of atomic excitation	63
5.6	Background-reduced spectroscopy	63
5.7	Conclusion	64
5.8	Supplementary information	65
	Derivation of Eq. 5.1	65
	Variation of the modulation frequency	66
	Spatially separated excitation of different atomic species	67
	Analysis of the spectroscopy results	67
6	Counterpropagating resonant TPA	73
6.1	Introduction	74
6.2	Experimental setup	75
6.3	Part 1: Spectral properties of two-photon excitation	75
	Nonresonant pathways	76
	Resonant pathways	77
	Experimental results	79
6.4	Part 2: Spatial properties of the excitation pattern	79
6.5	Part 3: Spectral properties at different spatial locations	82
6.6	Conclusion	84
7	Periodic Spectral Phase Modulation: an Alternative Parametrisation for Coherent Control Experiments	87
7.1	Introduction	88
7.2	Sinusoidal spectral phase	89
7.3	Periodic spectral phase with even functions	89
7.4	Periodic spectral phase with odd functions	92
7.5	Coherent control with periodic functions - Nonresonant TPA	93
7.6	Conclusion	97

Bibliography	99
List of Publications	113
Summary	115
Samenvatting	119
Acknowledgements	123

Introduction

The work presented in this thesis describes a new technique for performing direct frequency comb spectroscopy measurements in a counterpropagating pulse geometry. By employing methods from coherent quantum control we are able to perform precision measurements with improved accuracy. This also allows us to investigate the quantum interference between various pathways in two-photon excitation and generate complex excitation patterns that shed light on the interplay between resonant and nonresonant pathways.

In this chapter we provide a general introduction to the fields of coherent quantum control and high-precision laser spectroscopy, and present some of the elements in both fields that were combined to achieve our results.

1.1 Precision spectroscopy

Spectroscopy is the science of studying the structure of matter by its interaction with electromagnetic radiation. The beginning of this field dates back to the 17th century where Isaac Newton observed the refraction of white light through a prism. Later, it was shown that light-matter interaction can provide information about the internal structure of matter. Light that passes through a certain substance will be absorbed at specific wavelengths, which can be observed as dark lines in its spectrum. One of the goals in this field has always been to improve the resolution of spectroscopic measurements. Without a doubt, the invention of the laser in 1960 [1] has revolutionized the field of optical spectroscopy by providing a coherent light source with remarkable properties. Generally, lasers are categorized into 2 main types. The first type is pulsed lasers that, depending on the pulse duration, emits a large bandwidth of frequencies. The first demonstration of a laser by Maiman [1] used a flashlamp-pumped rod of Ruby to emit pulses with wavelength around 694.3 nm. As the energy of the laser is concentrated in a short pulse, the peak intensity can be very high, enabling the observation of nonlinear effects. The other type is a continuous wave (cw) laser [2] which ideally emits a single frequency.

With the development of tunable narrowband lasers, the field of atomic and molecular spectroscopy has come to full development. These light sources provided excellent resolution and allowed the excitation of single transitions with high accuracy. In spectroscopy of light atoms, the limiting factor of the measurement accuracy was often the Doppler broadening of the atomic transition. Scientists therefore developed techniques to perform sub-Doppler spectroscopy with e.g. counterpropagating laser beams [3, 4, 5, 6] or by cooling the atoms in a magneto-optical trap [7, 8, 9]. Precision spectroscopy has also played an important role in testing fundamental theories such as quantum electrodynamics (QED). QED provides corrections to the energy level structure due to 'virtual particles' of atoms and molecule, which can be accurately calculated for atoms such as hydrogen and helium. Precision measurements of these atoms [10, 11, 12, 13] have verified the QED corrections and initiated a continuous competition between theoreticians and experimentalists to push for better accuracies in order to find discrepancies with QED that could lead to discoveries of, yet, unknown physics.

The continuously improving accuracy of precision spectroscopy has interesting applications for time measurements. Presently the definition of time is based on a microwave transition in the ground state of cesium-133. A second is equal to 9 192 631 770 oscillations of this transition. A way to build a clock that provides better accuracy is to find a transition at an optical, or even higher frequency, with an extremely narrow linewidth. These transitions can be

measured accurately using ultrastable cw lasers and the transition frequencies can be used as a new standard for measuring time. Such transitions have been measured with ions [14, 15] and optical lattices [16, 17] with accuracies in the order of 10^{-18} . Measurements with optical atomic clock are currently used to investigate fundamental questions in physics [18, 19, 20] and hold promise to unravel hidden physical phenomena.

1.2 Coherent quantum control

Alongside the development of laser spectroscopy for high-precision measurements, scientists have also realized that lasers could be used for the manipulation of chemical reaction, and in particular the selective breaking of chemical bonds. It was suggested that the energy of a cw laser, tuned to the characteristic frequency of a chemical bond, would be absorbed in a selective way, leading the bond to break. The first experiments were conducted with ultrafast lasers to display such effects [21]. However, it was eventually shown that the deposited energy quickly dissipates, causing the rovibrational temperature to increase, which results in breaking of the weakest bond [22, 23] rather than the targeted one.

Despite the failure of these initial ideas, the concept of controlling and manipulating quantum processes with coherent light sources has sparked the imagination of many scientists and eventually led to the development of the field of coherent quantum control [24, 25, 26, 27]. One of the fundamental concepts of this field is the role of quantum interference in controlling atomic and molecular systems. In the 1980's several research groups have proposed methods to control molecular reactions, using either coupled cw lasers [28, 29] or trains of pulses with a precisely controlled time delay [30, 31]. Soon these predictions were verified in a series of experiments that demonstrated control over population transfer in bound-to-bound transitions [32], control of energy and angular distribution of photoionized electrons [33, 34], time-resolved spectroscopy [35] and many more.

A major challenge in this type of experiments is that the number of degrees of freedom in a molecular system strongly outweighs the number of control parameters available in the laser system. For this reason, the level of control remains limited and therefore inhibits real life applications of these methods. In order to gain better insight into the properties of quantum interference, some researchers have chosen simpler (atomic) systems with fewer degrees of freedom. Mainly cesium and rubidium atoms were used due to their specific energy level structure and the availability of laser systems at the required excitation frequencies. Furthermore, it was identified that two-photon transitions are very suitable for coherent control experiments with broadband pulses. This is

because many pairs of frequencies can excite the transition simultaneously. The quantum interference between these pathways can be manipulated using pulse shapers [36, 37] that provide control over the amplitude, phase and polarization of the individual frequencies. This enabled the study of a wide variety of quantum interference phenomena, such as two-photon transitions [38, 39, 40], strong field effects [41, 42, 43, 44, 45], temporal focusing [46, 47, 48] to name a few.

The spectral resolution achieved in these experiments is determined by the resolution of the pulse shaper, which is typically on the order of tens of GHz. This is many orders of magnitude worse than the resolution achieved in high-precision spectroscopy experiments, and it is therefore no surprise that there has been little overlap between these fields. This has changed with the invention of the frequency comb laser, which combines the broadband operation of pulsed lasers and the high spectral resolution of cw lasers, and that is the topic of the next section.

1.3 Frequency comb lasers

The development of the frequency comb laser is closely related to the advances in precision spectroscopy. With the development of stabilized narrowband laser sources it was possible to perform spectroscopy on a large variety of systems. However, in order to measure the absolute frequency of atomic and molecular transition it is necessary to compare the laser frequency to a primary standard. This standard is provided by a cesium clock at 9.2 GHz and is far away from the optical frequencies used in optical spectroscopy. A direct comparison between these frequencies is therefore not feasible and some way had to be found to bridge the gap. One solution that was developed was based on a "frequency chain" [49] where a series of tunable lasers was phase-locked to each other to provide a bridge from the rf frequency of the cesium clock all the way to infrared and optical frequencies. This technique enabled some very important measurements [50, 51]. However, these frequency chains were complex, expensive and usually had to be built differently for each application.

A much easier and more versatile solution was invented based on an optical frequency comb [52, 53, 54, 55, 56]. The concept behind a frequency comb is that a train of pulses with a constant time separation, and a fixed phase relation between consecutive pulses, results in a spectrum that consists of equidistant narrow modes. The relation between the temporal and spectral properties of the frequency comb is shown in Fig. 1.1. As the repetition frequency and the carrier-envelope offset frequency are both in the rf domain, they can easily be locked to a frequency generator and stabilized against a cesium clock (in practice locking the carrier-envelope offset frequency is quite non-trivial as we

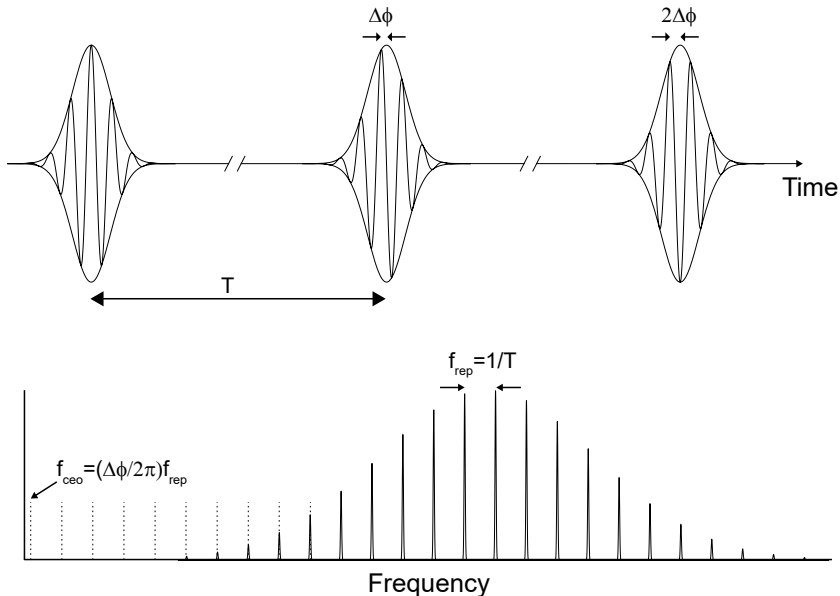


Figure 1.1: The relation between the temporal and spectral properties of a frequency comb. The absolute frequencies of the comb modes are unambiguously defined by the time separation of consecutive pulses and the carrier to envelope phase slip between neighboring pulses.

will see the next chapter). The frequency comb can then bridge the gap all the way to the optical frequency and in this way provides a ruler for accurately measuring absolute frequencies in the optical domain. One can safely say that the optical frequency comb has revolutionized the field of precision spectroscopy and enabled absolute frequency measurements with unprecedented accuracy.

Initially the frequency comb laser was used solely as a frequency ruler. However, researchers quickly saw the advantages of using the frequency comb pulses for attosecond physics [57], and to excite atomic and molecular transitions. The latter is a form of direct frequency comb spectroscopy (DFCS) which was demonstrated by Marian *et al* [58] with precise measurements of one- and two-photon transitions in Rb atoms. Many experiments followed, showing DFCS in atoms [59, 60, 61] ions [62] and molecules [63]. A major advantage of this method is that a cw excitation laser is no longer needed. Furthermore, a frequency comb laser can be used for different transitions due to the large bandwidth of the comb pulses. Arguably the biggest advantage of DFCS is that the high peak intensity of the frequency comb pulses enables up-converting its

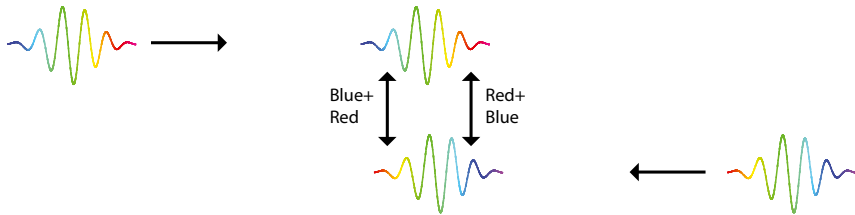


Figure 1.2: An illustration of the interaction between counterpropagating chirped pulses. The spread of frequencies under the broadened envelope results in combinations of red and blue frequencies (each frequency from a different pulse) to overlap at different positions of the pulse overlap.

frequency via nonlinear optical effect to perform spectroscopy in wavelength regions that are inaccessible to traditional lasers [64, 65].

1.4 Coherent control with frequency combs

With the emergence of DFCS, the application of coherent control techniques for frequency comb excitation became a natural step. Stowe *et al* [66, 67] have investigated the resonant two-photon excitation of cold Rb atoms in a magnetic optical trap (MOT) under the influence of shaped frequency comb pulses. They have shown that the increased resolution of the frequency comb laser enables the observation of new coherent control effects.

Another important experiment that combines frequency combs and coherent control has been conducted by Reinhardt *et al* [68]. In this experiment they have investigated the effect of chirp on two-photon excitation in the counter-propagating geometry. This geometry is especially interesting as it can be used to cancel the first-order Doppler effect [69, 4, 70, 71], and therefore enable sub-Doppler spectroscopy. Reinhardt *et al* have shown that the two-photon signal decreases as a function of chirp. This publication has triggered our interest as we were, at that time, considering a similar effect. Our intuition told us that chirping the pulses should not affect the total signal. For chirped pulses the frequencies are spread over the lengthened pulse, as shown in Fig. 1.2. When two counterpropagating chirped pulses overlap at the collision point, every pair of frequencies overlaps at a different position over the extended overlap region. We therefore expected the excitation to be spread over a larger spatial region but the total signal should stay the same as the excitation with Fourier-limited pulses, which is in contradiction with Reinhardt's result. This discrepancy

stimulated us to tackle this problem in a more rigorous way and we developed a model for the expected excitation pattern from counterpropagating pulses. Our model not only showed that chirped pulses should not affect the total signal, but also predicted that the total signal is completely unaffected by the spectral phase. We verified this in a series of measurements and also showed how this technique can be implemented in order to perform DFCS with unprecedented accuracy. We later extended this concept to resonant two-photon transitions where our method enables high-resolution control of the competition between resonant and nonresonant pathways. Finally, the insights gained from these experiments have been used by other members of our team to demonstrate the first realization of Ramsey-comb spectroscopy [72].

1.5 Outline of this thesis

This thesis is organized in the following way. Chapter 2 lays the theoretical foundations needed for the experiments discussed in the following chapters. Chapter 3 describes an experiment using two pulses with a variable time delay and illustrates the equivalence between the copropagating and counterpropagating geometries. Chapter 4 describes an experiment where pulse shaping has been used to eliminate the Doppler-broadened background in a two-photon transition for high-precision DFCS. In chapter 5 we discuss the mathematical model for counterpropagating excitation and show experimentally how a sinusoidal spectral phase can generate complex excitation patterns with distinct excitation regions. In chapter 6 we extend this concept to resonant two-photon transitions. We show that different quantum pathways react differently to the Doppler effect, and use this to investigate the interplay between resonant and nonresonant pathways. Finally, in chapter 7 we describe mathematically how periodic spectral phase shaping can generate extended pulse sequences and discuss their unique symmetry properties. A simulation is presented how such a phase mask can be of interest for experiments of quantum control landscapes.

Theoretical background

This chapter provides a theoretical background of the techniques used in the remainder of this thesis. We begin with a general description of electromagnetic waves and their propagation through vacuum and linear media. The work presented in this thesis deals exclusively with the manipulation of ultrashort pulses and their interaction with matter. We therefore first lay out the mathematical formalism to describe the properties of ultrashort pulses in both the time and frequency domains. Consequently we give explicit examples of various pulse shapes, some of which are used in the experiments described in later chapters. Finally we discuss the coherent addition of ultrashort pulses which forms the basis for describing frequency comb lasers.

2.1 Propagation of electromagnetic waves in vacuum

Throughout history light has been the subject of intense scientific research due to its intriguing properties and its eminent impact on everyday life. However, it was only in the 19th century that the origin of light was truly understood when James C. Maxwell identified light as an electromagnetic wave, thereby unifying the fields of optics and electromagnetism. In his theory the propagation of electromagnetic waves is described by the wave equation which, in vacuum, reads:

$$\frac{\partial^2 E(t, z)}{\partial z^2} - \epsilon_0 \mu_0 \frac{\partial^2 E(t, z)}{\partial t^2} = 0, \quad (2.1)$$

where ϵ_0 and μ_0 are the electric permittivity and magnetic permeability in vacuum, respectively. Note that, for notational simplicity, we have considered only a single spatial dimension and have neglected the magnetic field component. A particular solution of this equation is a monochromatic wave travelling with the speed of light $c = 1/\sqrt{\mu_0 \epsilon_0}$. The electric field oscillates with angular frequency ω and has a wavenumber $k = \omega/c$. This wave can be written as:

$$E(t, z) = A_\omega \cos(\omega t - kz), \quad (2.2)$$

where the propagation is in the positive z direction. As the wave equation is linear, any superposition of monochromatic waves is also a solution of this equation. The most general solution can therefore be written as:

$$E(t, z) = \int_{-\infty}^{\infty} d\omega A(\omega) e^{i(\omega t - kz)}, \quad (2.3)$$

where the function $A(\omega)$ represents the complex amplitudes of the different waves. If the function $A(\omega)$ is peaked around a central frequency ω_0 then the electric field assumes the shape of a wave packet with ω_0 as its carrier frequency.

Waves and wave packets can be represented either in the time or the frequency domain. Using the definition of the Fourier transformation we can identify the Fourier transform of the electric field as:

$$\tilde{E}(\omega, z) = \mathcal{FT}\{E(t, z)\} = 2\pi A(\omega) e^{-ikz}. \quad (2.4)$$

In the frequency domain we see that a wave packet is characterized at the origin ($z=0$) by $A(\omega)$ and the propagation in space is described by a spectral phase term. The propagation in vacuum amounts to an accumulating linear spectral phase, which is the time-domain equivalent of multiple waves travelling with the same velocity, leaving the shape of the wave packet unchanged. However, propagation through any other medium results in a nonlinear spectral phase term, causing waves to travel at different velocities. In this case the shape of the wave packet can change during propagation.

2.2 Propagation in transparent media

When light travels through a transparent dielectric medium the oscillating electric field polarizes the atoms in the medium. In turn, these oscillating dipoles also emit electromagnetic radiation. To account for this effect the wave equation has to be modified to:

$$\frac{\partial^2 E(t, z)}{\partial z^2} - \epsilon_0 \mu_0 \frac{\partial^2 E(t, z)}{\partial t^2} = \mu_0 \frac{\partial^2 P(t, z)}{\partial t^2}, \quad (2.5)$$

where $P(t, z)$ is the polarization field. In the regime of high field intensities this equation is responsible for nonlinear optical effects, such as harmonic generation, parametric amplification etc. In the experiments described in this thesis we have used moderate to low field intensities, excluding these effects. At low intensities the polarization field is assumed to be linear with respect to the electric field strength and can be written in the following way:

$$P(t, z) = \epsilon_0 \int_{-\infty}^t dt' \chi_e(t - t') E(t, z), \quad (2.6)$$

where χ_e is the electric susceptibility of the medium. Inserting Eq. 2.6 into the modified wave equation and performing a Fourier transformation leads to:

$$\frac{\partial^2 E(\omega, z)}{\partial z^2} + [1 + \chi_e(\omega)] \frac{\omega^2}{c^2} E(\omega, z) = 0. \quad (2.7)$$

The solution of this modified wave equation has the same form as Eq. 2.4,

$$\tilde{E}(\omega, z) = 2\pi A(\omega) e^{-ik(\omega)z}, \quad (2.8)$$

with the only difference that the wave number k is now a function of angular frequency, and is equal to:

$$k(\omega) = n(\omega)\omega/c, \quad (2.9)$$

where $n(\omega)$ is the refractive index. Light propagating through a transparent medium is therefore characterized by the accumulation of spectral phase $\phi(\omega)$ which takes the following form:

$$\phi(\omega) = k(\omega)z = (n(\omega)\omega/c)z. \quad (2.10)$$

In the visible and infrared spectral regions the refractive index of most transparent media is a monotonously increasing function that deviates only slightly

from a linear function. It is therefore a good approximation to write the spectral phase as a Taylor series around a central frequency ω_0 :

$$\phi(\omega) = \phi(\omega_0) + \phi'(\omega_0)(\omega - \omega_0) + \frac{1}{2}\phi''(\omega_0)(\omega - \omega_0)^2 + \dots \quad (2.11)$$

For most practical purposes it is sufficient to consider the spectral phase up to second order. The influence of the different orders on the properties of the wave packet is discussed in detail in section 2.4.

For some applications we would like to modify the spectral phase in ways that are impossible by simple propagation through a linear medium. Mathematically this is achieved by turning $A(\omega)$ into a complex function $A(\omega) = |A(\omega)| e^{i\phi_{mod}(\omega)}$, or in other words modulating the spectral phase with a phase mask $\phi_{mod}(\omega)$. In practice, such a spectral phase modulation can be implemented with devices called pulse shapers [73, 36]. For example, simple pulse shapers can be used to counteract the effect of pulse broadening in order to bring them back to their original shape [74]. Furthermore, computer-controlled pulse shapers can be implemented to dynamically search for an optimal pulse shape via a closed-loop learning algorithm [75, 76, 77, 78]. In more sophisticated schemes other degrees of freedom can be controlled such as spectral amplitude and polarization [79, 80, 81, 82]. This is, however, beyond the scope of this work and we will focus here exclusively on the manipulation of the spectral phase.

2.3 Properties of ultrashort pulses

In this section we present a mathematical formalism for describing ultrashort pulses both in the time and frequency domains. The starting point of this formalism is the Fourier representation of the electric field:

$$E(t) = \frac{1}{2\pi} \int_{-\infty}^{\infty} d\omega \tilde{E}(\omega) e^{i\omega t}. \quad (2.12)$$

Note that for notational simplicity we have discarded the spatial coordinate of the electric field. As was mentioned earlier, the function $\tilde{E}(\omega)$ provides information about the amplitudes and phases of the individual spectral components and can be calculated from the inverse Fourier transformation

$$\tilde{E}(\omega) = \int_{-\infty}^{\infty} dt E(t) e^{-i\omega t}. \quad (2.13)$$

Even though the electric field $E(t)$ is a measurable quantity, and therefore must be a real-valued function, it is frequently advantageous to represent the electric

field with a complex function. To this end we note that for any real-valued function in the time domain, its spectrum $\tilde{E}(\omega)$ must obey the condition

$$\tilde{E}(\omega) = \tilde{E}^*(-\omega), \quad (2.14)$$

where $*$ denoted complex conjugation. This relation suggests that knowledge of the spectrum for either positive or negative frequencies is sufficient to unambiguously characterize the electric field. We therefore separate the spectrum into two parts

$$\tilde{E}(\omega) = \tilde{E}^+(\omega) + \tilde{E}^-(\omega), \quad (2.15)$$

with $\tilde{E}^+(\omega)$ and $\tilde{E}^-(\omega)$ defined as

$$\begin{aligned} \tilde{E}^+(\omega) &= \tilde{E}(\omega) \text{ for } \omega > 0 \text{ and} \\ &0 \text{ for } \omega < 0, \end{aligned} \quad (2.16)$$

and

$$\begin{aligned} \tilde{E}^-(\omega) &= \tilde{E}(\omega) \text{ for } \omega < 0 \\ &0 \text{ for } \omega > 0. \end{aligned} \quad (2.17)$$

This allows us to define a complex-valued temporal function:

$$E^+(t) = \frac{1}{2\pi} \int_{-\infty}^{\infty} d\omega \tilde{E}^+(\omega) e^{i\omega t}, \quad (2.18)$$

that contains only positive frequencies but still holds all the information about the original function $E(t)$. As this function is complex-valued it can be expressed in terms of its amplitude and phase

$$E^+(t) = |E^+(t)| e^{i\phi(t)}. \quad (2.19)$$

Rewriting the temporal phase as a combination of a linear and a nonlinear term we can express the electric field as:

$$\begin{aligned} E^+(t) &= |E^+(t)| e^{i\omega_0 t} e^{i\phi_{nl}(t)} \\ &= \chi^+(t) e^{i\omega_0 t}, \end{aligned} \quad (2.20)$$

where $\chi^+(t)$ is the complex envelope function that encompasses both the (real) pulse envelope function as well as the nonlinear temporal phase terms, and ω_0 is the carrier frequency. Similarly, the positive frequency spectral function $\tilde{E}^+(\omega)$ can also be written as an amplitude and phase functions

$$\tilde{E}^+(\omega) = |\tilde{E}^+(\omega)| e^{-i\phi(\omega)}. \quad (2.21)$$

$|\tilde{E}^+(\omega)|$ is the spectral amplitude function, related to the spectral intensity $I(\omega) = |\tilde{E}(\omega)|^2$ which is typically measured with an optical spectrum analyser and $\phi(\omega)$ is the spectral phase function.

We make use of the formalism derived above to illustrate the relation between the temporal and spectral properties of short pulses. Consider a pulse with a Gaussian envelope

$$E^+(t) = e^{-2\ln(2)\left(\frac{t}{\Delta t}\right)^2} e^{i\omega_0 t}, \quad (2.22)$$

where Δt is the full-width-half-maximum (FWHM) duration of the pulse intensity, as depicted in Fig. 2.1. For this pulse the nonlinear phase terms are set to zero making the temporal envelope $\chi^+(t)$ a real function. The spectrum corresponding to this pulse is easily calculated by Fourier-transforming Eq. 2.22:

$$\tilde{E}^+(\omega) = e^{-\frac{\Delta t^2}{8\ln(2)}(\omega - \omega_0)^2}, \quad (2.23)$$

where constant proportionality factors were omitted for simplicity. The FWHM of the temporal and spectral intensities are related by

$$\Delta t \Delta \omega = 4 \ln 2, \quad (2.24)$$

which is called the time-bandwidth product. This relation shows that the bandwidth required to sustain an ultrashort pulse is inversely proportional to the pulse duration. For example, a Gaussian pulse of 10 fs duration has a spectral bandwidth of 44 THz (about 100 nm bandwidth around 800 nm central wavelength). The value of the time-bandwidth product derived in Eq. 2.24 is a specific result for a Gaussian spectrum and will be different for any other spectral shape even if the spectral width is the same. To illustrate this we consider a rectangular spectrum (flat-top) with the same FWHM as in the previous example:

$$\begin{aligned} \tilde{E}(\omega) &= 1 \text{ for } \omega_0 - \frac{\Delta\omega}{2} < \omega < \omega_0 + \frac{\Delta\omega}{2} \\ &0 \text{ elsewhere,} \end{aligned} \quad (2.25)$$

as shown in Fig.2.1. The Fourier transform of this rectangular function is

$$E(t) = \frac{\Delta\omega}{2\pi} e^{i\omega_0 t} \text{sinc}\left(\frac{\Delta\omega t}{2}\right). \quad (2.26)$$

In the case of a flat-top spectrum the time bandwidth product can be numerically evaluated and is equal to 5.56, which is more than 100% larger than the case of a Gaussian pulse. The difference in both shape and duration are depicted in Fig. 2.1.

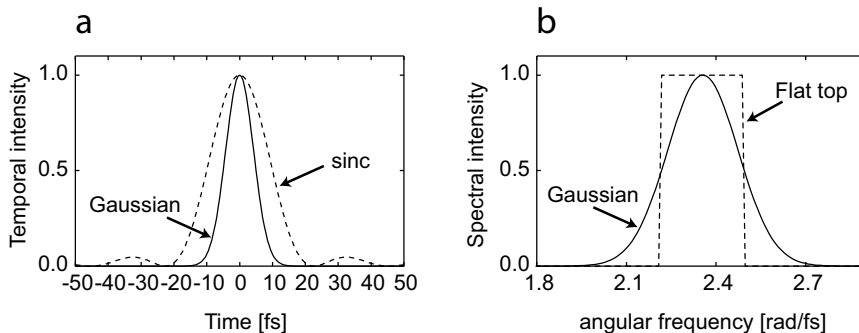


Figure 2.1: Spectral and temporal properties of different pulse envelopes. (a) Temporal intensity of a Gaussian (solid line) and a sinc (dashed) pulse. (b) the corresponding spectra. All functions are scaled to a maximum value of 1 for an easy comparison of their FWHM. Even though the FWHM of both spectra is the same (about 44 THz), the pulse duration can differ significantly (10 fs for the Gaussian pulse and 20.1 fs for the sinc pulse).

The equality sign in the time bandwidth is a special case when no nonlinear phases are considered. Such pulses are called Fourier transform limited. Any addition of nonlinear phases (either in the time or frequency domains) will increase the time bandwidth product, which indicates that a pure phase modulation in one domain results in amplitude broadening in the other domain. An example of this broadening effect is given in the following section.

2.4 Spectral phase shaping

With the fundamentals of ultrashort pulses explained in the previous section, we now turn to discuss how these pulses can be shaped using spectral phase modulation. We begin with a linear and a quadratic phase term and then continue to more complex phase patterns such as sinusoidal phase modulation and a V-shaped phase mask. For each case a phase mask $\phi_{mod}(\omega)$ is applied to an initially Fourier-limited pulse, characterized by a spectrum $E_{in}^+(\omega)$. The electric field of the shaped pulse is then calculated using:

$$E_{out}^+(t) = \frac{1}{2\pi} \int d\omega \tilde{E}_{in}^+(\omega) e^{-i\phi_{mod}(\omega)} e^{i\omega t}. \quad (2.27)$$

Linear spectral phase

In an earlier section we have shown that the propagation of pulses through a transparent medium can be expressed as a spectral phase function and can be written as a Taylor expansion. If higher-order dispersion terms are compensated for (made to vanish), then the propagation is described by a linear spectral phase. This is, for example, the case in a dispersion-compensated laser cavity. The electric field of a pulse that is subjected to a linear spectral phase of the form:

$$\phi(\omega) = \phi_0 + T(\omega - \omega_0), \quad (2.28)$$

can be easily calculated using Eq. 2.27:

$$\begin{aligned} E_{out}^+(t) &= \frac{1}{2\pi} \int d\omega \tilde{E}_{in}^+(\omega) e^{-i(\phi_0 + T(\omega - \omega_0))} e^{i\omega t} \\ &= e^{-i(\phi_0 - T\omega_0)} \int d\omega \tilde{E}_{in}^+(\omega) e^{i\omega(t-T)} \\ &= e^{i(T\omega_0 - \phi_0)} E_{in}^+(t - T). \end{aligned} \quad (2.29)$$

This result shows that a linear phase mask does not change the pulse envelope, regardless of its original shape. The control parameter T induces a time translation of the pulse envelope, while ϕ_0 changes the phase of the carrier frequency. In ultrashort optics the phase of the carrier with respect to the pulse envelope, also called the carrier-envelope phase (CEP), is a very important property. A zero CEP is defined when the peak of the envelope coincides with the peak of the carrier frequency, which is the case for the unmodulated pulse $E_{in}^+(t)$. After a linear phase mask is applied, the pulse has accumulated a CEP equal to $\Delta\phi_{CEP} = T\omega_0 - \phi_0$. In the case of a laser cavity T and ϕ_0 are related to the group and phase velocity, respectively. A difference between these two velocities leads to a CEP difference between consecutive pulses. This is an important property of frequency comb lasers, as will be explained in more details in a later section.

Quadratic spectral phase

We continue the previous discussion by considering the second-order term in the Taylor expansion. In many cases, including this term is sufficient to describe the propagation of pulses through optical elements such as lenses. As opposed to a linear spectral phase where the pulse envelope does not change, a quadratic phase leads to a frequency-dependent delay of the different spectral components (also called group-delay dispersion or GDD) and therefore alters the shape of the pulse envelope. To illustrate this effect we consider a Gaussian pulse as

defined in Eq. 2.22 and apply a quadratic spectral phase mask:

$$\phi(\omega) = \frac{1}{2}\phi_2(\omega - \omega_0)^2. \quad (2.30)$$

Again, the electric field of the shaped pulse can be calculated using Eq. 2.27:

$$\begin{aligned} E_{out}^+(t) &= \int d\omega e^{-\frac{\Delta t^2}{8 \ln 2}(\omega - \omega_0)^2} e^{-i\frac{1}{2}\phi_2(\omega - \omega_0)} e^{i\omega t} \\ &= e^{-\frac{t^2}{4\beta\gamma}} e^{i\omega_0 t} e^{iat^2} \end{aligned} \quad (2.31)$$

with

$$\beta = \frac{\Delta t^2}{8 \ln 2}, \quad \gamma = 1 + \frac{\phi_2^2}{4\beta^2}, \quad a = \frac{\phi_2}{8\beta^2\gamma}. \quad (2.32)$$

A Gaussian pulse under the influence of a quadratic spectral phase remains Gaussian, albeit with an increased pulse duration. The FWHM pulse duration of the stretched pulse is given by:

$$\Delta t_{out} = \Delta t_{in} \sqrt{1 + \left(4 \ln 2 \frac{\phi_2}{\Delta t_{in}^2}\right)^2}. \quad (2.33)$$

This relation shows that the stretching effect of GDD becomes increasingly more prominent as the original pulse duration is shorter. For example, a pulse passing through 1 cm of BK7 glass will experience a quadratic spectral phase with $\phi_2 = 440 \text{ fs}^2$. A transform-limited pulse of 10 fs will then stretch to about 122 fs. However, if the TL pulse was 100 fs in duration then the same GDD coefficient would have a negligible effect, stretching the pulse to 101 fs. In addition to a longer pulse duration, a quadratic spectral phase also leads to a time-dependent carrier frequency. From the definition of the instantaneous frequency $\omega_i = \frac{\partial \phi}{\partial t}$ we see that the spectral components are spread linearly under the pulse envelope. Such a pulse is said to be *linearly chirped*.

Sinusoidal spectral phase

The expansion of the spectral phase in a Taylor series is a good approximation when the coefficients of the expansion decrease rapidly. This is, however, not the case for highly oscillatory or periodic functions. It is therefore important to understand the influence of sinusoidal phase masks on ultrashort pulses. We consider the sinusoidal phase mask:

$$\phi(\omega) = A \sin(T(\omega - \omega_0) + \varphi_0) \quad (2.34)$$

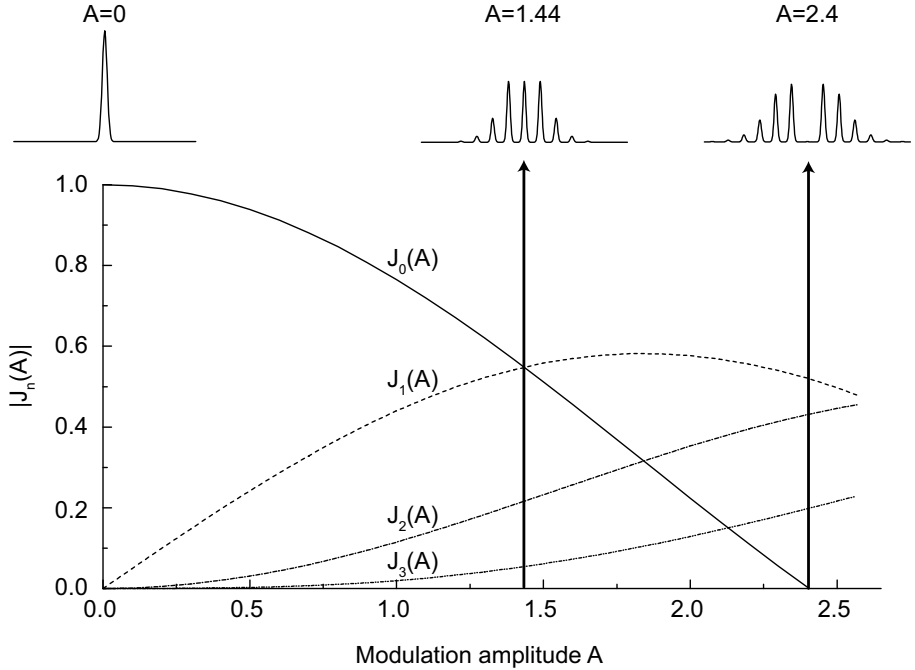


Figure 2.2: Amplitude of individual subpulses due to a sinusoidal spectral phase modulation. The amplitude of the n^{th} subpulse in the sequence is given by the Bessel function $|J_n(A)|$. The complete pulse sequence is illustrated for $A=0$, $A=1.44$ and $A=2.4$.

where A , T and φ_0 are the amplitude, frequency and phase of the modulation, respectively. As opposed to previous examples, the Fourier transform of the modulated spectrum

$$E_{out}^+(\omega) = e^{-iA \sin(T\omega + \varphi)} E_{in}^+(\omega) \quad (2.35)$$

cannot be Fourier-transformed directly. To rewrite the spectrum in a more convenient way we use the Jacobi-Anger relation

$$e^{iA \sin(\theta)} = \sum_{n=-\infty}^{\infty} J_n(A) e^{in\theta}, \quad (2.36)$$

where $J_n(A)$ is the Bessel function of the first kind and order n . The decomposition of a sinusoidal phase into a sum of linear phases makes the Fourier

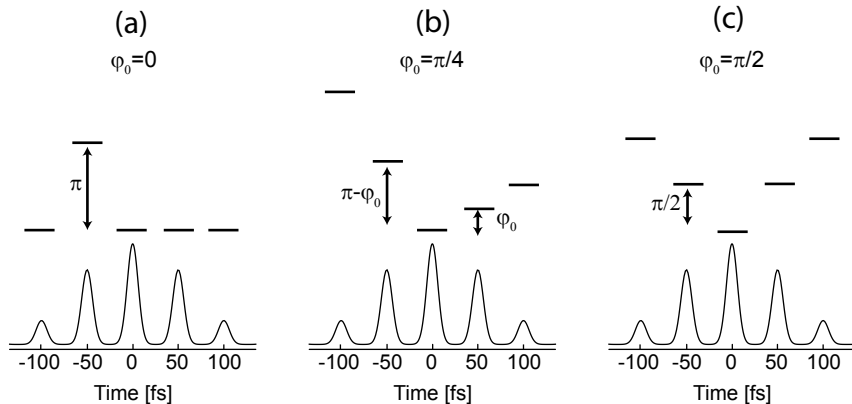


Figure 2.3: Temporal amplitude and phase of pulse sequences due to a sinusoidal spectral phase mask. The FWHM duration of the subpulses is 10 fs and the sinusoidal phase modulation is $\phi_{mod}(\omega) = A \sin(T(\omega - \omega_0) + \varphi_0)$, with $A = 1.2$ and $T = 50$ fs. The various temporal phase patterns correspond to (a) $\varphi_0 = 0$ (sine modulation), (b) $\varphi_0 = \pi/4$, and (c) $\varphi_0 = \pi/2$ (cosine modulation).

transformation of the spectrum a trivial task. In the time domain the shaped pulse is then:

$$E_{out}^+(t) = e^{i\omega_0 t} \sum_{n=-\infty}^{\infty} J_n(A) e^{-in\varphi} \chi_{in}^+(t - nT) \quad (2.37)$$

This result shows that a sinusoidal spectral phase produces a sequence of subpulses separated by a time T . If T is chosen to be larger than the duration of the unmodulated pulse, such that the subpulses are well separated, then the envelope of each subpulse is identical to the unmodulated pulse. The amplitude of the n^{th} subpulse is equal to $|J_n(A)|$, which is graphically depicted in Fig. 2.2. As the modulation amplitude A is increased, the energy of the central pulse is distributed in pre and post pulses. For example, at $A = 1.44$, where $J_0(A) = J_1(A)$ the amplitude of the first prepulse is equal to the central pulse. A further increase of A reduces the amplitude of the central pulse even more until it is completely diminished at approximately $A = 2.4$. We note that the amplitude of all subpulses are connected through a single parameter and cannot be tuned individually. Additional degrees of freedom can be introduced for increased flexibility, which is the topic of Chapter 7.

From Eq. 2.37 we also see that the subpulses in the sequence acquire differ-

ent absolute optical phases. For postpulses ($n > 0$), a linear change in optical phase occurs where every two consecutive subpulses differ by φ_0 . For prepulses ($n < 0$) an additional oscillating π phase jump is added due to the relation $J_{-n}(A) = (-1)^n J_n(A)$, such that adjacent prepulses have a $\pi - \varphi_0$ phase difference. Examples of these temporal phase patterns are shown in Fig. 2.3. For $\varphi_0 = 0$ the origin of the sine modulation is centred around the carrier frequency ω_0 , and the phase modulation is an odd function. In this case all postpulses have zero phase, whereas prepulses alternate between 0 and π (Fig. 2.3a). This is a unique situation where the complex envelope function is real. Any nonzero value of φ_0 turns the envelope into a complex function, as shown in Fig. 2.3b for $\varphi_0 = \pi/4$. A special case of a complex field is $\varphi_0 = \pi/2$, where the pure cosine modulation is a even function with respect to the carrier frequency and the temporal phase patterns becomes symmetric with respect to the central pulse, as shown in Fig. 2.3c. An interesting property of a cosine modulation is that the second harmonic of the field becomes a real function. The symmetry properties of even and odd spectral phase functions have intriguing consequences for the way ultrashort pulses interact with matter. This will be discussed extensively in later chapters and plays a central role in this thesis.

V-shaped spectral phase

In the previous section we have seen that pulse sequences can be generated with a sinusoidal spectral phase modulation. The envelope and the carrier frequency of the subpulses are the same as for the unmodulated pulse, which indicates that they have the same frequency content. However, for some applications it is necessary to create subpulses with different frequency contents. We consider a V-shaped spectral phase mask:

$$\phi(\omega) = T/2|\omega - \omega_0|, \quad (2.38)$$

which is composed of two linear functions with opposite slopes. For a qualitative description of this phase mask we recall that a linear spectral phase results in a group delay $T = \frac{\partial\phi(\omega)}{\partial\omega}$. It is then clear that all frequencies above ω_0 are translated in an opposite direction to the frequencies below ω_0 . The result is a pulse pair consisting of a "red" and a "blue" subpulse (red and blue with respect to ω_0). As the slope increases the two subpulses move further apart. For a more quantitative analysis we consider a V-shaped spectral phase mask applied to a flat-top spectrum as defined in Eq. 2.25. In the time domain the electric field can be written as:

$$E^+(t) = \int_{-\infty}^{\infty} d\omega E_{in}^+(\omega) e^{-iT/2|\omega - \omega_0|} e^{i\omega t}. \quad (2.39)$$

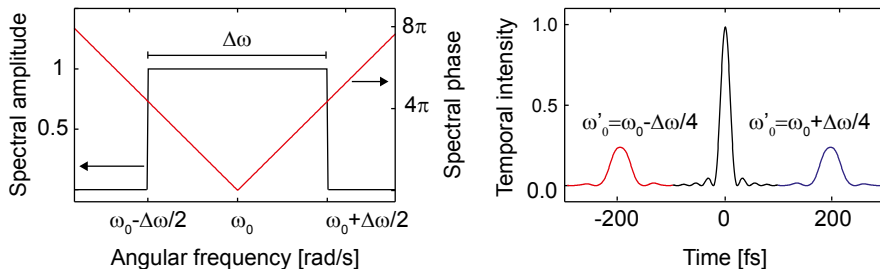


Figure 2.4: Spectral and temporal properties of a V-shaped phase modulation. A V-shaped spectral phase mask of the form: $\phi_{mod}(\omega) = T/2|\omega - \omega_0|$ with $T = 400$ fs is applied to a flat-top spectrum. The unmodulated pulse duration is equal to 20 fs (black line). A V-shaped spectral phase splits the pulse into a red and a blue pulse pair (red and blue lines). The pulse duration of each subpulse is doubled and the carrier frequency is shifted.

This integral can be quite complicated or even analytically unsolvable in some cases. However, for a flat-top spectrum the integration can be performed directly and the electric field becomes:

$$\begin{aligned}
 E^+(t) = & \frac{1}{2} \text{sinc} \left(\frac{\Delta\omega}{4} (t + T/2) \right) e^{it(\omega_0 - \frac{\Delta\omega}{4})} e^{-iT \frac{\Delta\omega}{4}} \\
 & + \frac{1}{2} \text{sinc} \left(\frac{\Delta\omega}{4} (t - T/2) \right) e^{it(\omega_0 + \frac{\Delta\omega}{4})} e^{-iT \frac{\Delta\omega}{4}}.
 \end{aligned} \tag{2.40}$$

As expected, the electric field is split into two parts representing the two subpulses, as graphically shown in Fig. 2.4. The first element for both subpulses is a time-shifted sinc function such that the time separation is equal to T . Note that each subpulse contains only half of the spectrum leading to a double pulse duration with respect to the unmodulated pulse. The second element represents the carrier frequency which is now the central frequency of the split spectrum. Finally, the third element is a common phase term which shifts the CEP of both red and blue subpulses by the same amount.

2.5 From pulse pairs to frequency combs

So far we have discussed the manipulation of a single pulse using the frequency domain modulation of its spectral phase, while leaving the spectral amplitude unchanged. We now turn to describe the coherent addition of ultrashort pulses

in the time domain and its effect on the spectral properties in the frequency domain. We begin with a simple case of a pulse pair where both pulses have the same envelope shape and amplitude. The pulses are separated by a time T and have a CEP difference of $\Delta\phi$. This pulse pair can be written as:

$$E_{\text{pair}}(t) = \frac{1}{2} \left(E_s(t + T/2)e^{i\Delta\phi/2} + E_s(t - T/2)e^{-i\Delta\phi/2} \right), \quad (2.41)$$

where $E_s(t)$ is the electric field of a single pulse. We derive the spectral properties of this pulse pair by Fourier transforming Eq. 2.41. The spectrum is then given by:

$$\begin{aligned} \tilde{E}_{\text{pair}}(\omega) &= \frac{1}{2} \tilde{E}_s(\omega) \left(e^{i(\omega T + \Delta\phi)/2} + e^{-i(\omega T + \Delta\phi)/2} \right) \\ &= \tilde{E}_s(\omega) \cos\left(\frac{\omega T + \Delta\phi}{2}\right). \end{aligned} \quad (2.42)$$

A graphic representation of the temporal and spectral properties of the pulse pair is shown in Fig. 2.5. In the frequency domain a pulse pair is characterized by a sinusoidal modulation of the spectral intensity, creating a "fat" mode structure with a frequency separation of $\omega_{rep} = 2\pi/T$ between the modes. The parameter T can be tuned to change the time separation between the pulses and therefore also the frequency separation between the modes. A larger time separation between the pulses increases the amplitude modulation and therefore the number of modes within the width of the spectrum. The appearance of a mode structure is even more pronounced when looking at the spectral phase. While the spectral phase across each mode is constant, a sharp jump occurs between the modes where the spectral intensity vanishes, leading to a π phase jump between adjacent modes. An overall frequency shift of the whole mode structure can be introduced by tuning $\Delta\phi$. In this way the lowest frequency mode (also called the carrier envelope offset frequency ω_{CEO}) is equal to $\omega_{CEO} = \Delta\phi/T$.

The previous discussion can be extended to account for long (and even infinite) trains of pulses. Provided that the pulses are regularly spaced and the CEP slip between consecutive pulses remains constant, we can write the electric field of the pulse train as:

$$E_{\text{train}}(t) = \sum_{n=0}^{N-1} E(t - nT)e^{-in\Delta\phi}, \quad (2.43)$$

where N is the total number of pulses. Note that we have used a slightly different representation than in Eq. 2.41 for reasons of mathematical simplicity.

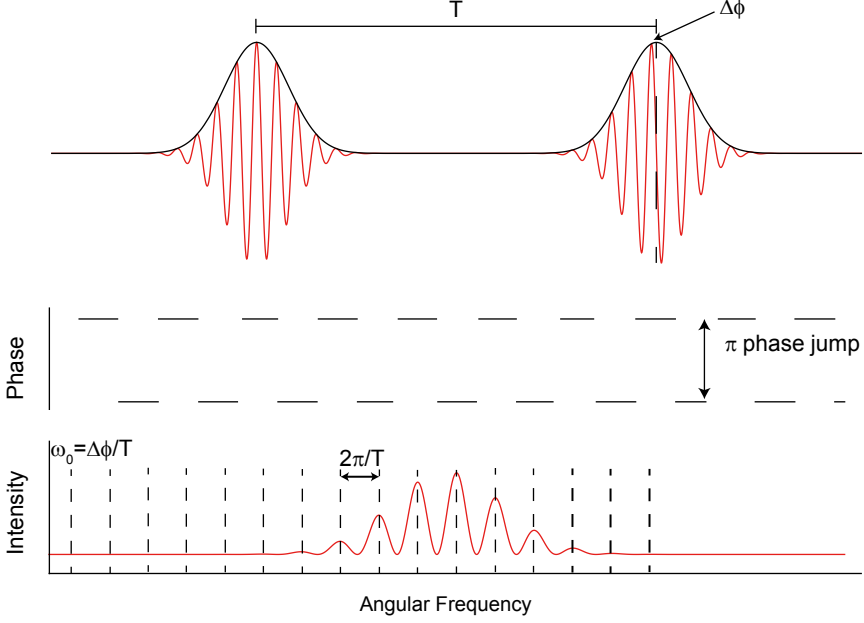


Figure 2.5: The temporal and spectral properties of a pulse pair. Two pulses separated by a time T and a CEP difference of $\Delta\phi$ result in a sinusoidally modulated spectral intensity and a block-wave spectral phase pattern. The position of the peaks is fully determined by T and $\Delta\phi$.

For this train of N pulses the Fourier transform of the electric field is given by:

$$\begin{aligned}
 E_{\text{train}}(\omega) &= E_s(\omega) \sum_{n=0}^{N-1} e^{-in(\omega T + \Delta\phi)} \\
 &= E_s(\omega) \frac{e^{-iN(\omega T + \Delta\phi)} - 1}{e^{-i(\omega T + \Delta\phi)} - 1} \\
 &= E_s(\omega) \frac{\sin [N(\omega T + \Delta\phi)/2]}{\sin [(\omega T + \Delta\phi)/2]} e^{-i\frac{N-1}{2}(\omega T + \Delta\phi)}.
 \end{aligned} \tag{2.44}$$

The spectral intensity and phase of Eq. 2.44 are shown in Fig. 2.6 for $N = 2, 3, 10, 11$ (The linear spectral phase component was omitted for simplicity and will be ignored in the following discussion). From this figure we see that an increasing number of pulses results in the narrowing of the spectral modes. This is also accompanied by the appearance of $N-2$ side peaks between neighbouring

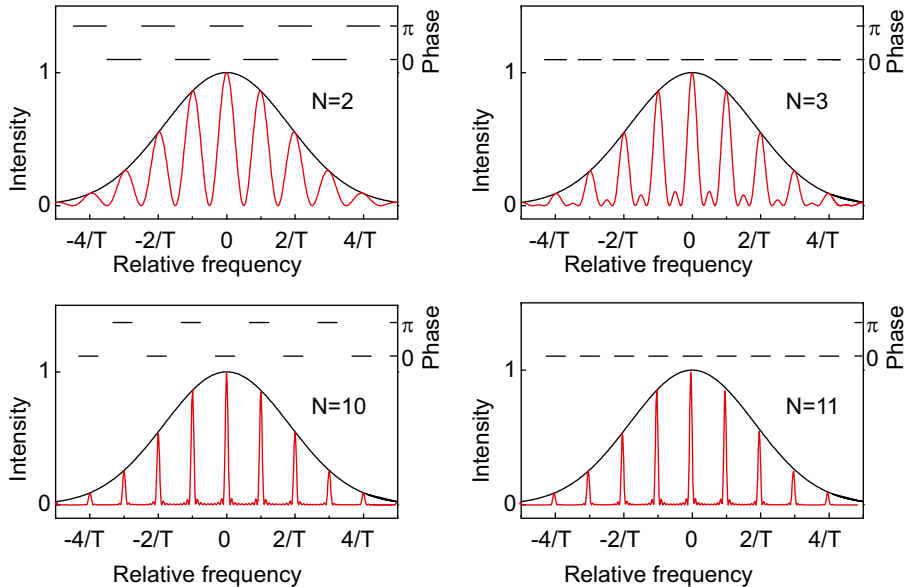


Figure 2.6: Spectral intensity and phase of a pulse train with N pulses. As the number of pulses increases, the spectral modes become narrower. The spectral phase pattern is flat for an odd number of pulses and displays an alternating π -step pattern for an even number of pulses.

modes. The spectral phase still displays a π phase jump between the modes (including the side peaks). If we only consider the main peaks then two different spectral phase patterns appear, depending on whether N is even or odd. For an even number of pulses, neighbouring modes are out of phase, as was explicitly shown for $N = 2$. Conversely, an odd number of pulses results in all modes having the same phase, as clearly shown in the lower part of Fig. 2.6. At the limit of an infinite pulse train ($N \rightarrow \infty$) the modes become infinitely narrow and the side peaks have negligible amplitude. The spectrum then consists of a comb-like pattern and is therefore called a *frequency comb* (see Fig. 1.1 for the relation between the spectral and temporal properties of the frequency comb). The absolute frequencies of all the modes are fully determined by two parameters and are expressed in the comb equation:

$$\omega_n = \omega_{CEO} + n \times \omega_{ref}, \quad (2.45)$$

where n is an integer. We note that at the limit of $N \rightarrow \infty$ the difference

between an even or odd number of pulses only reflects the (arbitrary) choice of the origin ($T=0$) and does not have any physical significance. In fact, to adhere to the definition of a frequency comb, the phase relation between the different modes does not have to assume any specific form, as long as this relation is fixed.

Even though the concept of a frequency comb is mathematically straightforward and has been known for many years, it is far from trivial to realize experimentally. A frequency comb laser is based on a modelocked oscillator that produces ultrashort (femtosecond) pulses. Such a laser, with a typical cavity length of several meters, emits a regular train of pulses separated by approximately 10 ns (leading to a $2\pi \times 100$ MHz repetition frequency). However, due to mechanical vibrations, thermal drift, and nonlinear optical effects in the laser cavity, the modes are not fixed in frequency and the comb structure can be washed out. It is therefore necessary to actively stabilize both ω_{CEO} and ω_{rep} . The repetition frequency can be stabilized by controlling the laser cavity length, which is accomplished by mounting one of the cavity mirrors on a piezo-electric transducer. The laser repetition frequency is measured with a photodiode and this signal is mixed with an ultrastable rf generator. An error signal, that is proportional to the difference between the frequencies, is fed back to a piezo-electric transducer which actively keeps the cavity length fixed. The more challenging task is to stabilize the carrier-envelope offset frequency, which is determined by the difference between the phase and group velocity in the laser cavity. The problem is that a direct measurement of ω_{CEO} is impossible because the spectral intensity at this frequency is negligible. However, an indirect measurement is made possible using an f-2f measurement [55]. In this technique the sum-frequency of the modes is generated, and then mixed with the original frequency comb. Provided that the original spectrum is octave-spanning, the spectral overlap between the fundamental and upconverted spectra yields a mixing signal that contains (among other combinations with ω_{rep}) the frequency ω_{CEO} . This mixing signal is then also compared to an ultrastable rf generator and can be used to actively stabilize the frequency comb. The active stabilization is accomplished by controlling the intensity of the pump laser which, via nonlinear effects, changes the group- and phase-velocity of the pulse circulating in the cavity.

As was mentioned above, an important requirement for the stabilization of a frequency comb laser is that its spectrum is octave-spanning [83, 84]. Most lasers, however, only have a moderately broad spectrum and have to be spectrally broadened outside the laser cavity. This is made possible by coupling ultrashort pulses into a photonic crystal fibre (PCF) [85, 86, 87]. The strong confinement in the fibre enables the generation of new frequencies via nonlinear effects and therefore broadens the spectrum. Careful tailoring of the dispersion properties of these fibers helps to maintain the high peak intensity

of the pulses during propagation, which is essential for inducing these nonlinear effects. The development of PCF's has lifted the last obstacle and paved the way for the realization of frequency comb lasers [56, 54].

Frequency comb lasers are versatile tools with a wide range of applications. In the field of high precision spectroscopy frequency combs are used for the calibration of the absolute frequency of cw laser, replacing cumbersome frequency chains [49]. The increased accuracy has led to precision measurements reaching accuracies of 2×10^{-18} . Furthermore, frequency combs have found applications in attoscience [88] and distance measurements [89], achieving precision and control that were previously thought impossible. The importance of the frequency comb in science has received its highest recognition in 2005 when John L. Hall and Theodor W. Hänsch were awarded the Nobel prize, where the development of the frequency comb was explicitly mentioned.

2.6 Light-matter interaction

For the experiments in this thesis the interaction between light and matter can be described in the semi-classical approach where the energy of the atom is quantized and the light is a classical field. The quantization of the atom leads to a discretized energy spectrum where the state of the atom is represented by a wave function $\psi = \sum a_m |\psi_m\rangle$, where $|\psi_m\rangle$ is the m^{th} eigenstate and a_m is the quantum mechanical amplitude of the corresponding energy state. The probability of an atom being at an energy level $|\psi_m\rangle$ is calculated by the square of the amplitude $P_m = |a_m|^2$. When the atom interacts with a fast oscillating electric field, the time-dependent perturbation can cause the quantum mechanical amplitude to vary in time and the atom will therefore undergo a transition to a different energy level. In the simple case of a two-level system, perturbation theory dictates that the quantum-mechanical amplitude of the excited state a_f is [90]:

$$a_f(t) = \frac{\mu_{fg}}{i\hbar} \int_{-\infty}^t dt_1 \epsilon(t_1) e^{i\omega_{fg}t_1}, \quad (2.46)$$

where ϵ is the electric field, μ_{fg} is the dipole matrix element and ω_{fg} is the resonance frequency $\omega_{fg} = (E_f - E_g)/\hbar$. We are interested in the excitation probability after the pulse has past ($t = \infty$). To simplify this expression we use the definition of the Fourier transformation, which leads to:

$$\begin{aligned} a_f(\infty) &= \frac{\mu_{fg}}{i\hbar} \int_{-\infty}^{\infty} d\omega \tilde{E}(\omega) \int_{\infty}^{\infty} dt_1 e^{i(\omega_{fg}-\omega)t_1} \\ &= 2\pi \frac{\mu_{fg}}{i\hbar} \tilde{E}(\omega_{fg}). \end{aligned} \quad (2.47)$$

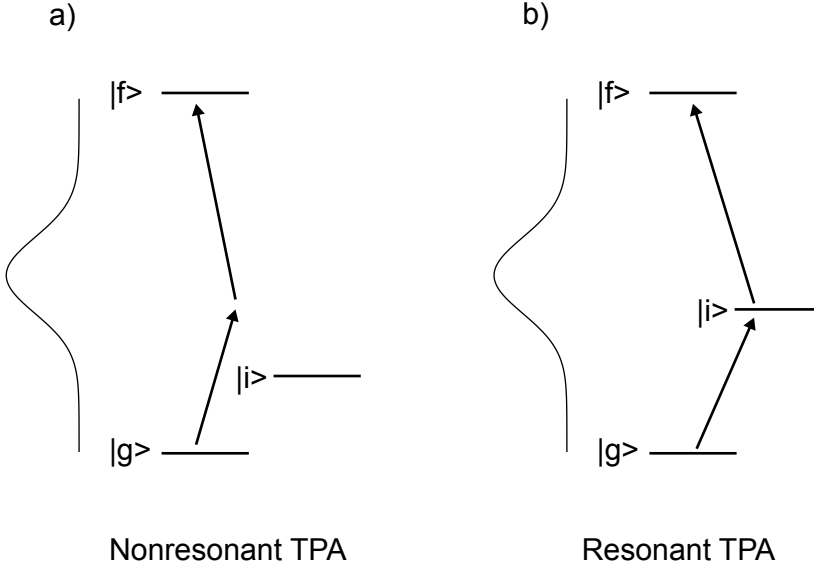


Figure 2.7: In case of two-photon excitation (TPA) a 3-level system with a ground ($|g\rangle$), intermediate ($|i\rangle$) and final ($|f\rangle$) state the atom can be excited to the final state in two different pathways, either with two photons $\omega_{i,g} + \omega_{f,i}$ or with any other combination of $\omega_1 + \omega_2 = \omega_{f,g}$. (a) In the nonresonant excitation scheme the laser spectrum does not include ω_i and only (multiple) nonresonant pathways are involved in the excitation. (b) In the resonant excitation scheme the laser spectrum covers ω_i such that both resonant and nonresonant pathways need to be considered.

This result shows that long after the pulse has passed, the transition probability only depends on the spectral amplitude of the field at the transition frequency. For a typical atomic transition with a linewidth of 1 GHz (including Doppler broadening), less than 0.1% of the pulse bandwidth actually contributes to the atomic transition. This shows that ultrashort pulses are very inefficient in driving one-photon transitions.

The situation changes considerably for a 3-level system, where the excitation to the upper state occurs via an intermediate level and is induced by two photons. From second-order perturbation theory we find that the quantum mechanical amplitude of the upper state can be written as [91]:

$$a_f(t) = -\frac{\mu_{f,i}\mu_{i,g}}{\hbar^2} \int_{-\infty}^t dt_1 \int_{-\infty}^{t_1} dt_2 \epsilon(t_1)\epsilon(t_2) e^{i\omega_{f,i}t_1} e^{i\omega_{i,g}t_2}, \quad (2.48)$$

where $\omega_{i,g}$ is the transition frequency from the ground state to the intermediate state and $\omega_{f,i}$ is the transition frequency from the intermediate state to the upper state. As in the case of a one-photon transition we can simplify this equation by Fourier-transforming the electric field and considering the limit of $t \rightarrow \infty$. We consider separately two limiting cases, depending whether the pulse spectrum can directly excite the intermediate state. In the nonresonant case (Fig. 2.7a) the spectral amplitude of the pulse at $\omega_{i,g}$ is zero, and therefore the intermediate state is not directly excited. In this case the transition amplitude can be written as:

$$a_f^{(2)}(\infty) \propto \int_{-\infty}^{\infty} d\omega A(\omega_t/2 + \omega) A(\omega_t/2 - \omega) e^{i[\phi(\omega_t/2+\omega) + \phi(\omega_t/2-\omega)]}. \quad (2.49)$$

This intuitive form of the two-photon amplitude shows that the excitation occurs for pairs of photons that add up to the transition frequency. Each pair contributes equally to the excitation and the total signal depends on the quantum interference between these contributions. For transform-limited pulses all spectral components are in phase which leads to perfect constructive interference and the excitation probability reaches its maximal value. The total signal depends only on the total energy of the pulse rather than the spectral amplitude of individual components. By using spectral phase shaping the relative phase between the individual contributions can be manipulated, enabling the control of the total signal [38, 91, 92].

In the other limiting case resonant two-photon excitation is achieved if the pulse spectrum contains the transition frequency to the intermediate state $\omega_{i,g}$, as illustrated in Fig. 2.7b. Both resonant and nonresonant pathways need to be considered and the transition amplitude can be written as [39]:

$$a_f^{(2)}(\infty) \propto i\pi \tilde{E}(\omega_{i,g}) \tilde{E}(\omega_{f,i}) + PV \int_{-\infty}^{\infty} \frac{d\omega}{\omega_{i,g} - \omega} \tilde{E}(\omega) \tilde{E}(\omega_{f,g} - \omega), \quad (2.50)$$

where PV represents the Cauchy principle value integral. The first term in Eq. 2.50 represents the stepwise excitation via the intermediate state while the second term is equal to the sum of all nonresonant pathways. As evident by comparing Eq. 2.49 and 2.50, the resonant excitation scheme will react differently to pulse shaping than its nonresonant counterpart. For example, the denominator in the second term of Eq. 2.50 leads to destructive interference between different photon pairs. Furthermore, the contributions of the first and second terms in Eq. 2.50 are perpendicular to each other, leading to a nontrivial interference. An immediate consequence of this observation is that a transform-limited pulse does not lead to optimal excitation. It has been shown by several research groups that by applying pulse shaping techniques the resonant two-photon signal can be strongly enhanced with respect to transform-limited pulses [93, 39, 40, 94].

Coherent control with pairs of shaped pulses

In this chapter we present an in-depth theoretical and experimental analysis of resonant and nonresonant two-photon absorption, induced by two time-delayed shaped laser pulses. Excitation in this scheme can occur via two photons from a single pulse or a combination of one photon from each pulse. The quantum interference between these two contributions is analysed, which enables us to identify the origin of the oscillations in the two-photon signal. The interplay between these contribution is manipulated by introducing a spectral phase mask that splits each pulse into a two-colour pulse pair. This phase mask enables us to either completely eliminate the signal or, in some cases, increase the signal beyond the level achieved with transform-limited pulses. The insight gained from these results can be used to investigate more complicated configurations, as will be shown in later chapters.

3.1 Introduction

The main theme of the work presented in this thesis is the use of pulse shaping techniques to manipulate the quantum pathways of two-photon transitions in a counterpropagating geometry. An important feature of this excitation scheme is that the transition can occur either by two photons from the same pulse (independent of the other pulse) or by one photon from each pulse (which results in a spatial dependence of the signal). Measuring such a signal proves to be a challenge as the overlap region of femtosecond pulses is in the order of tens of micrometers, which is very difficult to image onto a camera. The signal is also expected to oscillate on the submicrometer level which is impractical to image in our experimental conditions. An additional complication arises due to the different dependence of the quantum pathways on the Doppler effect, which must be incorporated into the model of the transition probability.

Here we gain insight into the excitation process in the counterpropagating geometry by investigating a comparable system, namely, the excitation of two-photon transitions with a pair of copropagating pulses that are separated by a variable time delay. The analogy between these two systems is illustrated in Fig. 3.1. In the counterpropagating geometry, an atom displaced by Δx from the pulse collision point will undergo the same excitation as in the copropagating geometry when the pulses are separated by $\Delta T = 2\Delta x/c$. Therefore, the excitation with counterpropagating pulses can be simulated with two copropagating pulses by performing a complete scan of the time delay T . This allows us to carefully investigate the interference between the various quantum pathways with a simple setup. A pulse pair can be easily created with a Michelson interferometer and the variable time delay can be controlled with a much better resolution than the spatial resolution of a camera. Furthermore, the Doppler effect is the same for all quantum pathways in the copropagating geometry, making a model for the transition probability easy to develop.

3.2 Experimental Setup

The laser system used in this experiment is derived from a home-built Ti:sapphire oscillator with central wavelength of 760 nm. To accommodate both resonant and nonresonant excitation schemes the cavity dispersion was adjusted to support broadband operation of about 120 nm FWHM. The laser pulses are then directed into a dispersion free 4f pulse shaper [73], consisting of a pair of 1200 lines/mm gratings and $f=25$ cm cylindrical mirrors. A computer-controlled spatial light modulator (SLM), placed at the Fourier plane of the pulse shaper, is used to imprint a spectral phase mask. The shaped pulses then pass through a Michelson interferometer where one of the mirrors is mounted on a computer

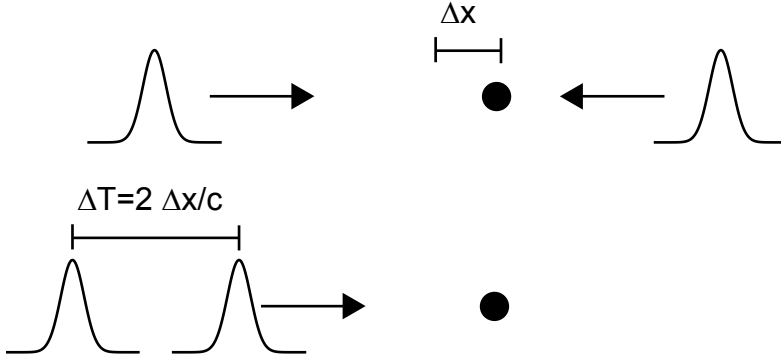


Figure 3.1: Comparison between the counterpropagating geometry and two copropagating pulses. The position along the propagation dimension is mapped onto a time delay between the pulses. Therefore, the excitation with counterpropagating pulses can be simulated with a scan of the time delay between a copropagating pulse pair. The major difference between these geometries is the response to the Doppler effect, which will be discussed in a later chapter.

controlled translation stage with a spatial resolution of about 10 nm. Each time-delayed shaped pulse pair is focused in a Rb vapour cell which is heated to a temperature of 70°C in order to increase the atomic density and therefore the signal. For all the measurements in this chapter we excite the $5S \rightarrow 7S$ two photon transition at 2×760 nm. The relevant intermediate level for this transition is the $5P$, which is split into two levels at 780 nm and 795 nm. We perform both nonresonant and resonant measurements; both these schemes are illustrated in Fig. 3.2. In the nonresonant excitation scheme we placed a hard aperture at the Fourier plane of the pulse shaper to limit the spectrum to about 20 nm at 760 nm, thereby not exciting any intermediate resonances. For resonant excitation a double aperture is used that creates a spectrum with two regions of 16 nm bandwidth, centred at 795 nm and 728 nm. This choice of the clipped spectrum ensures that only a single intermediate resonance is excited. Atoms excited to the upper level decay back to the ground state via the $6P$ level. The 420 nm photons emitted in this process are detected with a photomultiplier tube (PMT).

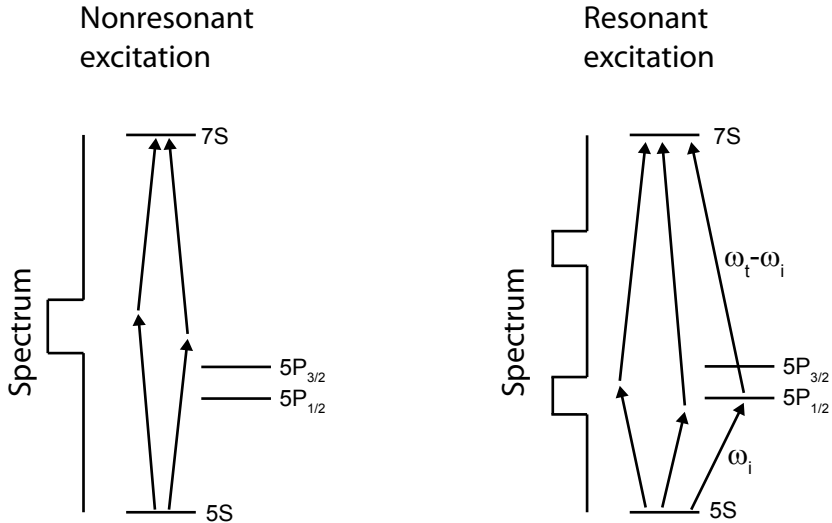


Figure 3.2: Nonresonant and resonant excitation schemes. In the nonresonant excitation scheme the laser spectrum does not include ω_i and only nonresonant pathways are considered. In the resonant excitation scheme ω_i and $\omega_t - \omega_i$ are covered by the laser spectrum and both resonant and nonresonant pathways contribute to the excitation.

3.3 Single pulse excitation

In the first set of measurements we investigate the effect of spectral phase shaping of a single pulse on the two-photon signal. This is realized by blocking one arm of the interferometer and applying a spectral phase mask:

$$\varphi(\omega) = \tau|\omega - \omega_t/2|. \quad (3.1)$$

As was mentioned earlier this phase mask splits a transform-limited pulse into a red-blue pulse pair with an interpulse time delay of 2τ . The central frequency of the phase mask was chosen at half the transition frequency $\omega_t/2$ such that the pairs of frequencies involved in the excitation are spatially separated. For each of the measurements the signal is recorded as a function of the control parameter τ . This is done in both the resonant and nonresonant cases. We

analyse the results in both the time and the frequency domain in order to give an intuitive interpretation as well as a robust and quantitative analysis.

Nonresonant TPA

In the nonresonant excitation scheme the laser spectrum does not contain the frequencies needed to excite the atom to the intermediate state, therefore only the upper state is populated. It has been shown by Meshulak et al [38] that in this case the two-photon signal is maximal for transform-limited (TL) pulses and pulse shaping can only reduce the total signal. To understand the effect of a V-shaped spectral phase on the TPA signal we first consider the situation in the time domain. As mentioned earlier this phase mask splits a TL pulse into a red-blue pulse pair. It is therefore clear that a temporal overlap between the red and the blue subpulses is necessary for the two-photon transition to take place. The spectrum used for this measurement has a flat-top shape with a bandwidth of 20 nm and is centred around 760 nm. The red and blue subpulses, each having a 10 nm bandwidth, have a sinc-like temporal envelope with a pulse duration of about 170 fs.

A measurement of the signal strength as a function of τ is shown in Fig. 3.3. As expected, the maximal signal is achieved for zero separation ($\tau=0$) and is reduced as the separation between the subpulses increases. However, the overlap between the red and blue subpulses is not the only parameter that determines the signal strength. For a separation of 100 fs we see that the overlap is still substantial while the signal is zero. Furthermore, increasing the pulse separation of 150 fs results in an increase of the signal.

For a more rigorous approach we consider the situation in the frequency domain. An analytical expression for the TPA signal is acquired by inserting the phase mask in Eq. 3.1 into Eq. 2.49, leading to:

$$S = |a_f|^2 \quad (3.2)$$

$$a_f \propto \int_{-\infty}^{\infty} d\omega A(\omega_t/2 + \omega) A(\omega_t/2 - \omega) e^{i2\tau|\omega|}.$$

For this derivation we assume that the decay time of the upper state is much longer than the pulse duration of the pulse. This equation shows the summation of the photon pairs that sum up to the transition frequency. At $\tau=0$ all frequency pairs have the same phase and the quantum interference is perfectly constructive, leading to maximal signal strength. As τ increases, the frequency pairs acquire different phases and the interference becomes destructive, hence reducing the total signal. The first minimum at 100 fs is the point where the spectral phase at the edge of the spectrum reaches π . At this point each pair with a certain phase has a complementary pair with the opposite phase, leading to perfect destructive interference and therefore vanishing signal strength. In

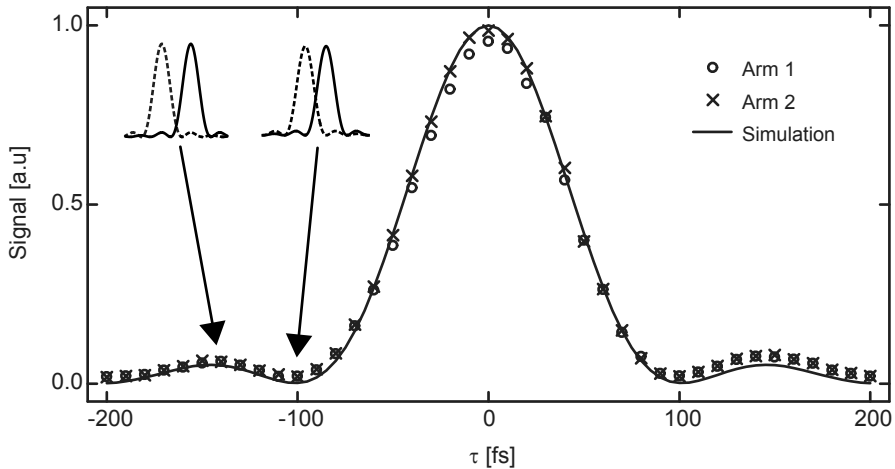


Figure 3.3: Experimental results and numerical simulation of the nonresonant TPA. The control parameter is the slope of the V-shaped phase mask as defined in Eq. 3.1. The measurement was done separately for either arm of the interferometer, showing no differential power or chirp imbalance. For two time delays ($\tau = -100$ fs and $\tau = -140$ fs) the temporal intensity of the red (dashed line) and blue (solid line) subpulses is shown. This shows that the temporal overlap of the subpulses is not the only parameter that determines the signal strength and we need to consider the quantum interference between all photon pairs that contribute to the excitation.

the case of a flat-top spectrum, the integral in Eq. 3.2 can be easily solved and is equal to:

$$a_f \propto \Delta\omega e^{i\tau\Delta\omega/2} \text{sinc}\left(\frac{\tau\Delta\omega}{2}\right). \quad (3.3)$$

Interestingly, the signal is an exact reconstruction of the temporal intensity profile of the unshaped pulse with the same FWHM. However, this is only true in the specific case of a flat-top spectrum and can not be generalized to other spectral shapes.

Resonant TPA

The situation changes considerably for the resonant excitation scheme where the intermediate state is actually populated during the excitation. This happens when the laser spectrum covers the transition frequency to one or more

intermediate states (for simplicity we will only consider a single intermediate level). Besides the nonresonant pathways, which were discussed in the previous section, we need to include the resonant pathway that occurs via stepwise excitation with photon frequencies ω_i and $\omega_t - \omega_i$. Because the atom is actually excited to the intermediate state, the requirement for temporal overlap of the photon pair is lifted. However, the order in which these two photons arrive at the atom becomes important. Clearly, ω_i has to arrive before $\omega_t - \omega_i$ for the stepwise excitation to occur. In the present case of the $5S \rightarrow 7S$ transition the relevant intermediate level is the $5P_{1/2}$ at 795 nm, with the complementary wavelength at 728 nm. This means that stepwise excitation only takes place if the red photon (795 nm) is in front of the blue (728 nm). For the following measurements the spectrum of the laser was clipped at the Fourier plane of the pulse shaper, with two regions of 16 nm width around the wavelengths 795 nm and 728 nm.

The effect of a V-shaped spectral phase on the resonant TPA signal is shown in Fig. 3.4. As predicted, the order of the red-blue subpulses determines the signal strength. For a negative V-shaped phase mask the blue photon is contained in the leading subpulse and is not resonant with any state for an atom that is in the ground state. The atom is later excited to the intermediate level by the red subpulse but this does not contribute to the signal as only atoms in the upper state are detected by our PMT. On the other hand, for a positive V-shaped phase, the atom is excited first to the intermediate level with the red photon and subsequently to the upper state with the blue photon, resulting in a strong TPA signal. One of the most intriguing properties of resonant TPA is that transform-limited pulses do not result in maximal signal [39] (as opposed to nonresonant TPA). For the measurement presented here we indeed see a fivefold increase in signal for a positive V-shaped phase with respect to transform-limited pulses. This raises some questions that cannot simply be answered within the current time-domain analysis. For example, what is the nature of the quantum interference between the resonant and nonresonant pathways? To answer this question we analyse the resonant TPA process in the frequency domain.

In the frequency domain the upper state population is described by Eq. 2.50. For the double flat-top spectrum used here the integration over the nonresonant pathways can be limited to the small region around ω_i . Furthermore, we write the integral separately for contributions below and above the resonance.

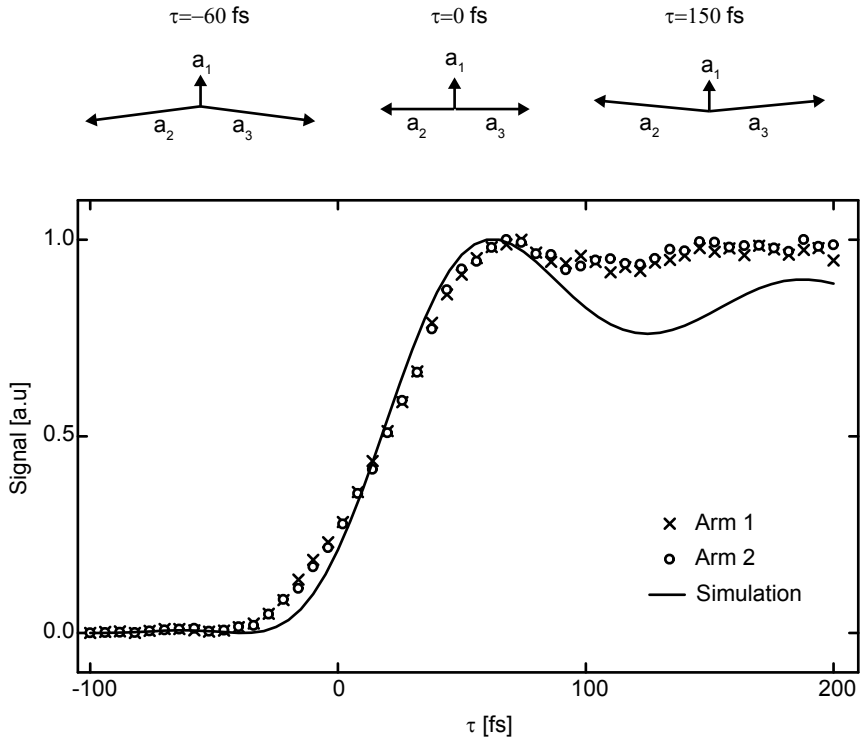


Figure 3.4: Experimental results and numerical simulation of resonant TPA. The signal is recorded as a function of τ , defined in Eq. 3.1. The measurement was done separately for each arm of the interferometer, showing no differential power or chirp imbalance. To show the interaction between resonant and non-resonant pathways, the different contributions a_1 , a_2 and a_3 are drawn in the complex plane for 3 different values of τ .

Finally, inserting the expression for the V-shaped spectral phase we get:

$$\begin{aligned}
 |a_f|^2 &\propto |a_1 + a_2 + a_3|^2 \\
 a_1 &= i\pi e^{2i\tau|\frac{\omega_t}{2} - \omega_i|} \\
 a_2 &= \int_{\omega_i - \Delta\omega/2}^{\omega_i} \frac{d\omega}{|\omega - \omega_i|} e^{2i\tau|\frac{\omega_t}{2} - \omega|} \\
 a_3 &= \int_{\omega_i}^{\omega_i + \Delta\omega/2} \frac{d\omega}{|\omega - \omega_i|} e^{2i\tau|\frac{\omega_t}{2} - \omega|}.
 \end{aligned} \tag{3.4}$$

The 3 components a_1 , a_2 and a_3 represent the amplitudes of the different quantum pathways. a_1 is the resonant term, a_2 is the sum of nonresonant pathways where the photon energies are from opposite sides of the intermediate resonance and a_3 is the sum of nonresonant pathways where the photon energies are from the same side of the intermediate resonance. The upper state population is proportional to the square of the vector sum of these terms. For a better understanding of the quantum interference between these terms it is instructive to visualize these contributions in the complex plane for different values of τ . The magnitude and direction of these terms is depicted in Fig. 3.4 for $\tau = -60 \text{ fs}$, $\tau = 0 \text{ fs}$ and $\tau = +150 \text{ fs}$. For a transform-limited pulse ($\tau = 0$) the amplitudes a_2 and a_3 are equal in magnitude and opposite in direction and therefore cancel each other completely. In this case only the resonant pathway contributes to the excitation. When τ is negative both a_2 and a_3 rotate away from a_1 and not only cancel each other but also cancel a_1 , leading to zero signal. On the other hand, for positive τ , a_2 and a_3 rotate towards a_1 and therefore enhance the signal. This analysis might not be as intuitive as the time-domain description, but it provides insight into how the different pathways interfere. It also reveals the potential for additional enhancement of the signal with different pulse shapes. This however goes beyond the scope of the present work and is described elsewhere [39]. For the purpose of the present work we conclude that a V-shaped spectral phase is an effective tool to either enhance or completely eliminate the resonant TPA signal.

3.4 Double-pulse excitation

In the previous section we saw that the application of a V-shaped spectral phase mask is an effective tool for controlling the resonant and nonresonant TPA signal. We now extend the discussion to include a second shaped pulse with a time delay T . The pulses are generated in a Michelson interferometer and are therefore exact copies. The combination of a Michelson interferometer and a V-shaped phase mask results in a train of 4 subpulses with two control parameters τ and T , as depicted in Fig. 3.5. In the following measurements

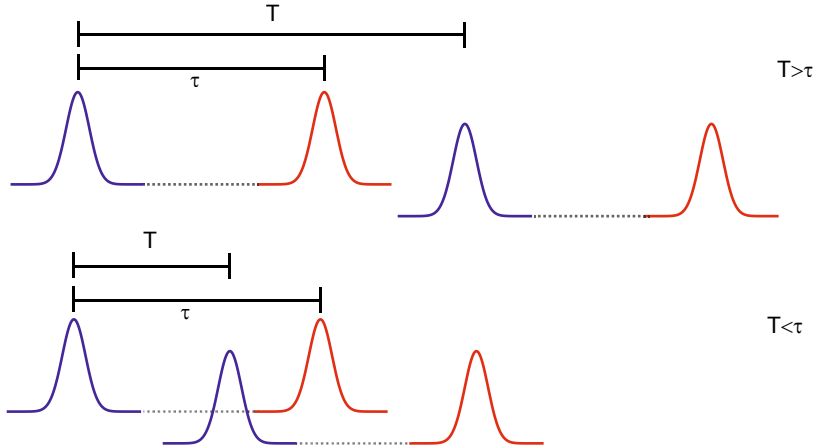


Figure 3.5: Pulse sequences generated by a combination of a Michelson interferometer and a V-shaped spectral phase mask. The ratio between the two control parameters and the sign of τ determine the ordering of the red and blue subpulses.

we record the TPA signal as a function of the time delay T . This is done for various values of τ and in particular for values where the single pulse signal is either eliminated or strongly enhanced.

Nonresonant double-pulse TPA

We begin with the simple case of two transform-limited pulses with a variable time delay T . This is the broadband equivalent of Fourier transform spectroscopy [95]. As in the single pulse measurement, we limit the spectrum to about 20 nm which correspond to a pulse duration of 80 fs. The experimental result and numerical simulation are shown in Fig. 3.6(a,b), showing excellent agreement. The simulation was performed using the substitution $A(\omega) \rightarrow A(\omega) \cos(\omega T/2)$ in Eq. 3.2 and setting $\tau = 0$. In the inset of Fig. 3.6 we see that the oscillation period for small T (smaller than the pulse duration) is approximately 2.5 fs while for large T the period is reduced to half at 1.25 fs. These values correspond well with the transition frequency ω_t . A similar measurement on Cs atoms has been performed by Blanchet et al [96] where the different oscillation period were explained with the difference between optical and quantum interference. For small T , optical interference between the two pulses results in a modulation of the laser intensity. The modulation period is

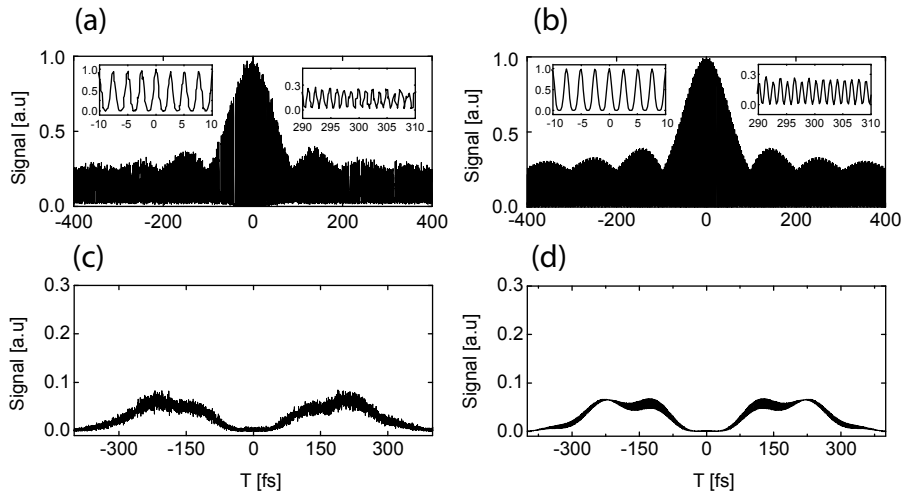


Figure 3.6: Nonresonant TPA induced by two time-delayed shaped pulses. Experimental results (a) and the numerical simulation (b) for transform-limited pulses. Experimental results (c) and a numerical simulation (d) for shaped pulses with $\tau=100$ fs.

equal to the inverse of the central laser frequency ω_0 , hence the observed signal oscillation. On the other hand, for large T , there is no optical interference and the optical intensity is constant. In this case the oscillations are attributed to quantum interference where the phase between the two pulses is either in phase with the wave function evolution (maximal atomic excitation) or out of phase (zero signal). Even though this interpretation is successful in explaining the observed signal this is only true in the specific case of a single upper state, and when the central optical frequency is equal to $\omega_t/2$. We find that the argument made by Blanchet et al, that only optical interference is responsible for the oscillation in the centre, incorrect and is not necessarily true in the general case. In order to trace the true origin of the oscillation frequency for all values of T we developed a rigorous and quantitative analysis in the frequency domain. This analysis is also easy to use in combination of additional spectral phase shaping.

In the frequency domain an interferometer is equivalent to a sinusoidal modulation of the spectral amplitude $A(\omega) \rightarrow A(\omega) \cos(\omega T/2)$. In the general case, however, the two pulses can have a carrier-envelope phase difference which is represented in a shift of the spectral amplitude modulation $A(\omega) \rightarrow A(\omega) \cos((\omega - \omega_{ref})T/2)$. Taking that into account, the TPA signal can be

written as:

$$|a_f|^2 \propto |a_1 + a_2|^2, \quad (3.5)$$

where

$$a_1 = \cos((\omega_t/2 - \omega_{ref})T) \times \int d\omega A(\frac{\omega_t}{2} + \omega)A(\frac{\omega_t}{2} - \omega) \exp \left[i \left(\phi(\frac{\omega_t}{2} + \omega) + \phi(\frac{\omega_t}{2} - \omega) \right) \right] \quad (3.6)$$

and

$$a_2 = \int d\omega A(\frac{\omega_t}{2} + \omega)A(\frac{\omega_t}{2} - \omega) \exp \left[i \left(\phi(\frac{\omega_t}{2} + \omega) + \phi(\frac{\omega_t}{2} - \omega) \right) \right] \times \cos(\omega T). \quad (3.7)$$

For the experimental results using an interferometer we need to set $\omega_{ref} = 0$. However, as we will see later, ω_{ref} plays an important role in the oscillation frequency of the signal. The terms a_1 and a_2 represent the different quantum paths to the upper state. a_1 accounts for the contributions of two photons from the same pulse while a_2 refers to excitation with photons that originate from separate pulses. Even though these two terms look quite similar, they present a very different behaviour as a function of T . For a_1 it results in a constant oscillation where the amplitude of the oscillation is equal to the single pulse integral (Eq. 3.2) and the oscillation frequency is $\omega_t/2 - \omega_{ref}$. On the other hand, a_2 has the form of an overlap integral and does not have fast oscillations as a function of T . The oscillation frequency of the signal is therefore solely dependent on $\omega_t/2 - \omega_{ref}$, and in the case of an interferometer the frequency is equal to $\omega_t/2$ rather than the laser central frequency, as was asserted by Blanchet et al [96].

To further illustrate the difference oscillation period of the signal in Fig. 3.6 we calculate both the transition amplitude and transition frequency. In general, the transition amplitude is complex-valued. However, for transform limited pulses both a_1 and a_2 are real. The results are shown in Fig. 3.7. The transition amplitude in the upper panel clearly shows the individual contribution of a_2 (dashed line) and the superimposed oscillation from a_1 (ω_{ref} was set to zero). This also explains the different oscillation periods of the transition probability (lower panel). For small T the transition amplitude is positive and therefore the transition probability has the same oscillation period. However, for large T the transition amplitude oscillates between positive and negative values such that the transition probability oscillates with a doubled frequency.

An advantage of the frequency domain equations developed here is that the effect of spectral phase shaping can be easily incorporated, and the effect on a_1

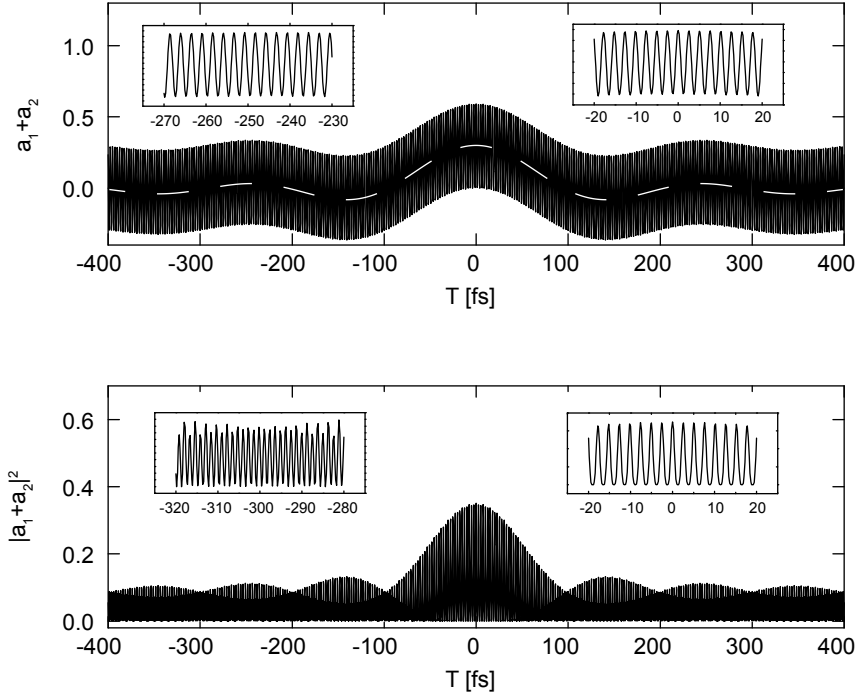


Figure 3.7: The transition amplitude (upper panel) and transition probability (lower panel) of nonresonant TPA with transform limited pulses.

and a_2 is easily understood. As mentioned earlier the term a_1 oscillates with an amplitude that is equal to the single pulse signal. From Fig. 3.3 we learned that a V-shaped phase mask with $\tau=100$ fs completely eliminates the single pulse signal. In the present case this means that a_1 becomes negligible and the total signal only depends on a_2 . Even though the integral in a_2 cannot be solved analytically for a V-shaped phase, it is clear that we can only expect nonzero signal when $T \approx \tau$. The experimental results and numerical simulation of the signal when applying a V-shaped phase with $\tau=100$ fs is shown in Fig. 3.3 (c,d). We see indeed that the fast oscillations are eliminated and that two broad peaks appear when $T \approx \tau$. In the time domain this result can also be explained by the temporal overlap between red and blue subpulses when $T \approx \tau$. The ability to eliminate the single pulse signal while generating strong signal at two different time delays T and $-T$ proves to be very useful for high precision spectroscopy and spatial coherent control, as we will see in the following chapters.

Resonant TPA

The last case we consider in this chapter is resonant TPA with two, shaped and time delayed, pulses. This case is more complex than the ones considered earlier as we need to consider both resonant and nonresonant pathways, as well as photon pairs from the same pulse or from different pulses. We use the results from previous sections and the intuition we developed in order to analyse the TPA signal for both transform limited pulses and pulses subjected to a V-shaped phase mask.

Following the same steps as in the previous section we derive an expression for the transition probability of resonant TPA with two pulses:

$$|a_f|^2 \propto |a_1 + a_2 + a_3 + a_4|^2, \quad (3.8)$$

$$a_1 = i\pi A(\omega_i)A(\omega_0 - \omega_i) \cos\left(\frac{\omega_t}{2}T\right) e^{i2\pi\left|\frac{\omega_t}{2} - \omega_i\right|}, \quad (3.9)$$

$$a_2 = i\pi A(\omega_i)A(\omega_0 - \omega_i) \cos\left((\omega_t/2 - \omega_i)T\right) e^{i2\pi\left|\frac{\omega_t}{2} - \omega_i\right|}, \quad (3.10)$$

$$a_3 = \cos(\omega_t T/2) \int \frac{d\omega}{\omega_i - \omega} A(\omega)A(\omega_t - \omega) e^{i2\pi\left|\frac{\omega_t}{2} - \omega\right|}, \quad (3.11)$$

$$a_4 = \int \frac{d\omega}{\omega_i - \omega} A(\omega)A(\omega_t - \omega) \cos\left((\omega_t/2 - \omega)T\right) e^{i2\pi\left|\frac{\omega_t}{2} - \omega\right|}. \quad (3.12)$$

The first two terms a_1 and a_2 represent the stepwise excitation via the intermediate resonance while a_3 and a_4 account for nonresonant pathways. Furthermore, for a_1 and a_3 the two photons originate from the same pulse while for a_2 and a_4 the photons of each pair come from different pulses. For transform limited pulses ($\tau = 0$) we know that the integral over the nonresonant pathways above and below the intermediate resonance cancel each other. Therefore, both a_3 and a_4 have negligible contribution to the signal. Considering only the resonant pathways, the transition amplitude will consist of a beat between the transition frequency ω_t and the difference between the two resonant frequencies $\omega_t - 2\omega_i$. These characteristic frequencies are expected to be present in the signal along with cross terms, as a consequence of the nonlinear nature of the TPA process. An interesting observation is that no signature of the pulse overlap at the origin is expected, as opposed to nonresonant TPA signal (Fig. 3.6). The experimental results and numerical simulations of the signal are presented in Fig. 3.8, showing excellent agreement. For transform limited pulses we indeed see that there is no increase in signal strength in the region where the pulses overlap. The oscillations also present the expected behaviour with a fast oscillation corresponding to $\omega_t/2$ and a beat period that is equal to the difference between the two steps of the resonant pathway.

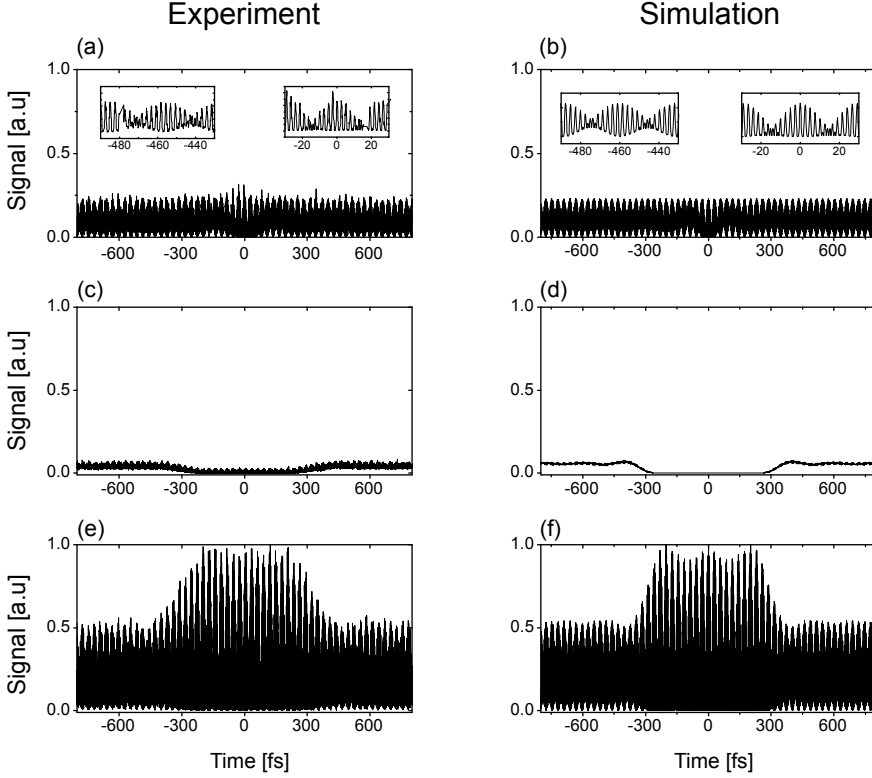


Figure 3.8: Experimental results of the resonant TPA signal for transform limited pulses (a,b), negative V-shaped phase $\tau = -150$ fs (c,d) and positive V-shaped phase $\tau = +150$ fs (e,f).

In a previous section it was shown that a V-shaped phase mask rotates the nonresonant contributions and that their total magnitude is no longer negligible. For the present case this means that all 4 amplitude terms need to be considered, which makes it difficult to predict the signal without an elaborate numerical simulation. A much more intuitive picture of the signal strength is acquired in the time domain. As was shown in Fig. 3.5 we have two red-blue pulse pairs leading to 4 possible combinations that enable stepwise excitation. The contrast of the signal can be predicted by counting the number of combinations of red and blue subpulses that have the right orientation. For a negative V-shaped phase mask and close to the origin ($-\tau > T > \tau$), the two blue subpulses are in front of the red subpulses and the total signal is then zero. This

is clearly shown in the results in Figs. 3.8(c,d) where the slope of the phase was set to $\tau = -150$ fs. Beyond the turning point ($T = \pm\tau$) the red subpulse of the leading pair passes the blue subpulse of the trailing pair and one combination of red and blue subpulses drives the transition. It is interesting to note that a negative V-shaped phase does not result in signal oscillation. In order to significantly increase the signal we can invert the V-shaped phase, which also inverts the order of the subpulses. As shown in Figs. 3.8(e,f), a positive V-shaped phase results in maximal signal contrast in the centre ($\tau > T > -\tau$). In this region all red subpulses are in front of the blue subpulses and therefore all 4 combinations contribute to the signal. The order of the pulses changes when T is increased beyond the turning point ($T = \pm\tau$), where only 3 combinations of subpulses excite the stepwise excitation. The reduction of the signal agrees very well with the expected ratio of $(3/4)^2$. These results clearly demonstrate how a combined time and frequency domain analysis unravels all the features of the signal.

3.5 Conclusion

In this chapter we presented an in-depth analysis of resonant and nonresonant TPA when excited with either a single shaped pulse or a pair of copropagating shaped pulses. We have shown that a V-shaped spectral phase mask is an effective tool to manipulate the the different quantum pathways and control both the oscillation frequency and the envelope of the signal. Excellent agreement was found between the experimental results and the numerical simulations. We have shown that a time and frequency domain analysis provides an intuition to the TPA process, as well as quantitative analysis. The results and concepts presented in this chapter will serve as the basis for the following chapters.

High-precision spectroscopy with counterpropagating femtosecond pulses

An experimental realization of high-precision direct frequency comb spectroscopy using counterpropagating femtosecond pulses on two-photon atomic transitions is presented. Doppler broadened background signal, hampering precision spectroscopy with ultrashort pulses, is effectively eliminated with a simple pulse shaping method. As a result, all four 5S-7S two-photon transitions in a rubidium vapour are determined with both statistical and systematic uncertainties below 10^{-11} , which is an order of magnitude better than previous experiments on these transitions.

4.1 Introduction

One of the hallmarks of laser spectroscopy has been the theoretical prediction [97] and the experimental realization [69, 4] of two-photon Doppler-free spectroscopy using continuous wave (CW) lasers in a counterpropagating beam geometry. In this method, the Doppler shift due to the velocity of an atom in the lab frame is compensated by an opposite shift from a counterpropagating beam. Therefore Doppler-free signals can be obtained, even without the use of laser cooling and trapping techniques. A classic example of Doppler-free two-photon excitation with high accuracy is 1S-2S spectroscopy in hydrogen [11]. Doppler-free two-photon spectroscopy has been essential in the determination of the Rydberg constant and proton charge radius [98], accurate tests of quantum electrodynamics, and the detection of possible drifts in fundamental constants [99]. An extension of the Doppler-free method to nanosecond pulses [100] has been implemented for high-precision spectroscopy in, for example, molecular hydrogen [101] and muonium [102]. A more recent development in precision spectroscopy is the realization of the optical frequency comb, which revolutionized the field of precision measurements [103, 89]. An optical frequency comb is based on the precise phase relation of a train of ultrashort pulses and acts as a frequency ruler, connecting the rf and optical frequency domains. In the field of precision spectroscopy, optical frequency combs were initially used as a referencing tool for a separate CW excitation laser. Subsequently, frequency combs were used to induce transitions directly for precision measurements [58, 60, 62], which marked the beginning of a new field of direct frequency comb spectroscopy (DFCS). The high peak intensity of ultrashort pulses from frequency comb lasers also facilitates frequency conversion via nonlinear processes, paving the way for high-precision spectroscopy in wavelength regions where CW lasers do not exist [104, 64, 65, 63].

Combining DFCS with Doppler reduction using counter propagating beams has therefore drawn significant attention. One approach is to drive the transition via an intermediate resonance (stepwise excitation) which enhances signal strength [105, 61]. The signal is then indeed free of Doppler broadening, however, due to the imbalance between the two frequencies the line centre is shifted. Furthermore, population transfer to the intermediate level complicates assessment of systematic effects. Alternatively, nonresonant excitation is also possible on two-photon transitions. Pairs of modes from the comb laser can then combine to the same total energy, so that the full comb spectrum contributes to the signal [106, 71]. In this scheme, Doppler-free excitation only occurs in the region of space where the counterpropagating pulses overlap. For pulses of typical frequency comb lasers with a duration in the femtosecond range, this zone is limited to tens of micrometers in length, while Doppler-broadened ex-

citation with copropagating photons can take place over the whole beam path. Therefore, a dominating and detrimental background of Doppler-broadened signal impairs high-precision DFCS. Recently it was shown that the Doppler-broadened background can be reduced by stretching the pulses with group-velocity dispersion [107], and that it can even be completely eliminated using concepts from quantum coherent control [108]. In the latter case sophisticated pulse shaping techniques with a spatial light modulator were employed.

In this letter, we demonstrate a general method that enables high-resolution DFCS on two-photon transitions in a counterpropagating geometry. We introduce a simple and flexible split-pulse technique to eliminate the Doppler-broadened background. Combined with the versatility of DFCS we acquire signal with excellent signal-to-noise (SNR) ratio and low sensitivity to systematic effects. We demonstrate the possibilities of this method by performing absolute frequency measurements on the 5S-7S transitions in rubidium. The resulting accuracy of the 4 measured transitions (2 hyperfine transitions in 2 Rb isotopes) is an order of magnitude better than previous demonstrations with either DFCS [59] or CW lasers [109].

4.2 Setup

The experimental setup is shown schematically in Fig. 4.1. The frequency comb used in this experiment is based on a mode-locked Ti:sapphire oscillator with a pulse repetition rate that can be tuned between 140 and 180 MHz. It has a central wavelength of 760 nm, and a full width half maximum (FWHM) bandwidth of approximately 40 nm. The spectrum is composed of a large collection of equidistant narrow modes which are described by the comb equation $f_n = f_0 + n \times f_{rep}$. Here f_0 is the carrier-envelope offset frequency, f_{rep} is the repetition frequency, and n is an integer mode number with a typical value of 10^6 . Both comb parameters (f_{rep} and f_0) are locked to low-noise rf generators, which themselves are referenced to a GPS-disciplined Rb atomic clock (better than 2×10^{-12} fractional accuracy).

Both the ground (5S) and excited (7S) states are split due to the hyperfine interaction. Selection rules dictate that only transitions between levels with the same hyperfine quantum number ($\Delta F=0$) are allowed. A simplified level structure of rubidium is shown as an inset of Fig. 4.1. The spectroscopy is conducted in a commercial glass cell containing the two stable isotopes ^{85}Rb and ^{87}Rb . The transitions are induced by focusing frequency comb pulses in the middle of the cell with $f=150$ mm lenses to a beam size of about $100 \mu\text{m}$ at the focus. A mirror reflects the pulses back so that consecutive pulses overlap at the focus. Excitation to the 7S is monitored by detecting the 420 nm fluorescence from cascade decay via the 6P state with a photomultiplier tube (PMT).

4. HIGH-PRECISION SPECTROSCOPY WITH COUNTERPROPAGATING FEMTOSECOND PULSES

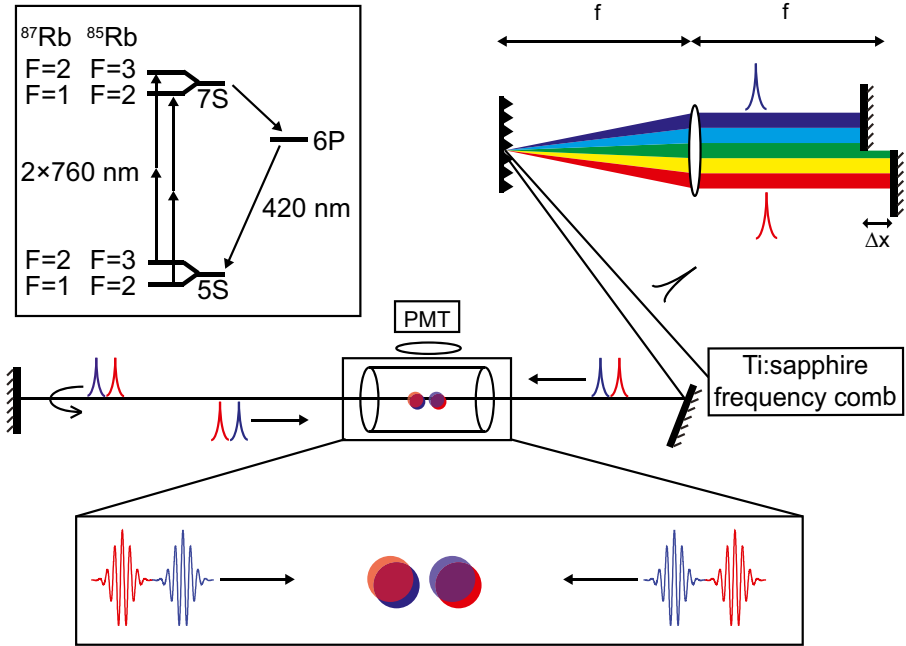


Figure 4.1: A schematic of the shaping and spectroscopy setup. Each frequency comb pulse is split into a red and a blue subpulse in a simplified shaping apparatus. A delay between the subpulses reduces single-sided excitation while not affecting the total counterpropagating signal (localized in two separate excitation regions). The inset shows a simplified level scheme of atomic rubidium.

4.3 Background reduction

Atomic excitation with counterpropagating femtosecond pulses presents a challenge as the (Doppler broadened) single-sided signal is not confined to the small overlap region and will therefore obscure the counterpropagating signal. To eliminate this background signal we apply a group delay between the lower and upper half of the spectrum, effectively splitting each pulse into a "red" and a "blue" subpulse with a relative delay on a picosecond time scale. As a combination of red and blue subpulses are simultaneously needed to induce the transition, increasing the time delay between them will diminish the single-sided signal. We achieve this situation with a particularly simple pulse shaper configuration, consisting of a grating, a lens and two mirrors (see Fig. 4.1). Each frequency comb pulse is spatially dispersed using the first half of a zero-

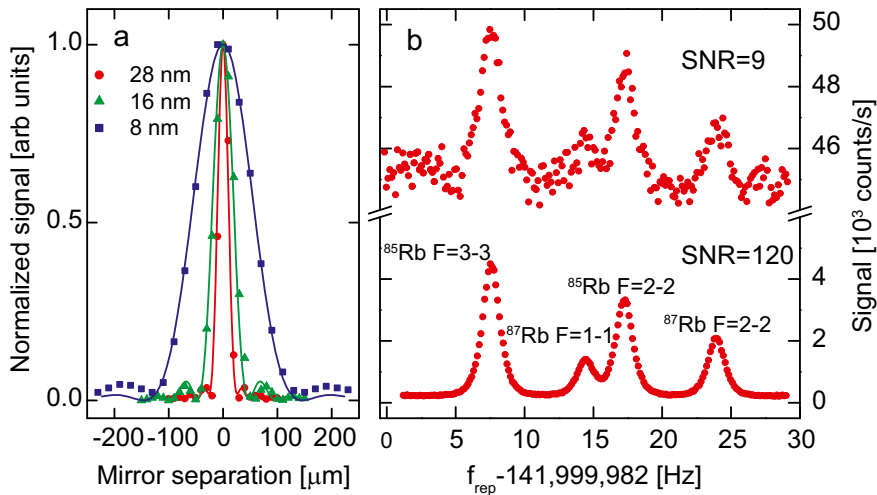


Figure 4.2: (a) Normalized excitation rates of single-sided signal as a function of the mirror separation in the shaping setup. A suppression of better than 98% is achieved for the various spectral widths. (b) A scan over all 4 5S-7S transitions, with (lower curve) and without (upper curve) background suppression, demonstrating the dramatic improvement in SNR. The SNR of the background-free measurement is only limited by shot-noise fluctuations. The traces were taken with a spectral bandwidth of 28 nm and an integration time of 3 seconds per point.

dispersion 2f-2f configuration. The laser light is reflected back at the Fourier plane using two separate mirrors to form the desired red and blue subpulses, each containing half of the original spectrum. The time delay between the two subpulses is adjusted by displacing one of the two mirrors, while the bandwidth of each subpulse can be controlled by placing a hard aperture in the Fourier plane (not shown in the figure). Throughout the measurements the laser spectrum did not exceed 40 nm in order to avoid the single-photon excitation to the 5P state at 780 nm.

We test this principle by blocking the returning beam in Fig. 4.1, so that only single-sided excitation is induced. The Doppler width of the relevant transitions at room temperature is about 1 GHz, which is much larger than the spacing between the comb modes. This washes out the comb structure and the resulting signal generates a background that is independent of the comb parameters f_0 and f_{rep} . In Fig. 4.2a the single-sided signal is plotted as a function of the

time delay between the subpulses for various spectral widths, together with numerical simulations (the solid lines) based on a framework developed in [91]. A larger temporal separation is needed for elimination of the single-sided signal when the pulses have a smaller bandwidth (because the pulse duration is then longer). This measurement can be seen as a type of cross correlation between the two subpulses. However, it is important to note that the two-photon signal does not simply depend on the pulse duration and intensity. For example, adding higher odd-order dispersion lengthens the pulses but does not change the total two-photon signal [38, 108]. For the investigated spectral bandwidths we find a background reduction of at least 98% (this number is limited by measurement noise), for a mirror separation of less than 150 μm . A small mirror separation is advantageous in order to prevent deformation of the laser beam after the shaping apparatus.

4.4 Counterpropagating excitation

With the single-sided signal effectively eliminated, we add the back-reflected beam in Fig. 4.1. Red and blue subpulses from opposite directions now overlap in two separate spatial regions and induce counterpropagating signal. The counterpropagating beam geometry reduces the original 1 GHz Doppler width to below the value of f_{rep} so that excitation only takes place if combinations of modes are resonant with the transition frequency f_t . A scan over the various 5S-7S transitions is achieved by taking small steps of the repetition frequency f_{rep} . Such a scan is presented in Fig. 4.2b where a significant improvement in SNR is clearly visible when single-sided excitation is eliminated.

The peaks in Fig. 4.2b correspond to values of the comb parameters (f_{rep} , f_0 and n) for which $f_t/2$ coincides with one of the comb modes or is exactly between two modes. As a consequence, a scan of f_{rep} results in a periodic signal with periodicity of $f_{rep}/2$ (for an overview of DFCS see [110]). Furthermore, whenever two photons of a single mode sum up to the transition frequency ($f_t = f_n + f_n$) then other pairs of modes are also resonant ($f_t = f_{n-k} + f_{n+k}$), which means that all of the comb modes participate in the excitation. For each pair of frequencies (f_1, f_2) the line shape can be described as a Voigt profile (convolution of a Gaussian g_D and a Lorentzian g_b), with a Gaussian width of $2\sqrt{\ln 2} \frac{u}{c} |f_1 - f_2|$. $u = \sqrt{2k_B T/M}$ is the most probable velocity of atoms with mass M at temperature T . The line profile in this situation is equal to [105]:

$$\begin{aligned}
 |a_f^{(2)}|^2 &\propto \left(\frac{|E(f_1)|^2 |E(f_2)|^2}{(f_1 - f_i)^2 ((f_t - f_1 - f_2)^2 + 1/4\tau_f^2)} \right) * g_D, \\
 g_D &= \exp \left[- \left(\frac{c}{u} \right)^2 \left(\frac{f_t - (f_1 + f_2)}{f_1 - f_2} \right)^2 \right],
 \end{aligned} \tag{4.1}$$

where E is the spectral amplitude and τ_f is the decay time from the excited state. In this derivation it was assumed that no intermediate levels (f_i) are populated. Extending this equation to account for all possible mode combinations is achieved by replacing the single frequencies (f_1, f_2) with the comb equation and summing over all comb modes. This leads to the following equation:

$$\begin{aligned}
 |a_f^{(2)}|^2(f_{rep}) &\propto \\
 \sum_{n_1, n_2} &\left(\frac{|E(f_{n_1})|^2 |E(f_{n_2})|^2}{(f_{n_1} - f_i)^2 ((f_t - f_{n_1} - f_{n_2})^2 + 1/4\tau_f^2)} \right) * g_D, \\
 g_D &= \exp \left[- \left(\frac{c}{u} \right)^2 \left(\frac{f_t - (f_{n_1} + f_{n_2})}{f_{n_1} - f_{n_2}} \right)^2 \right].
 \end{aligned} \tag{4.2}$$

The experimental results of the line profile of the ^{85}Rb (F=3-3) transition are shown in Fig 4.3. As predicted by Eq. 4.2, the line width is proportional to the laser bandwidth. For bandwidths larger than 25 nm a neighbouring transition ^{87}Rb (F=2-2) starts to overlap with the ^{85}Rb (F=3-3) line shape. The solid lines in Fig. 3 are numerical calculations of Eq. 4.2 for different spectral bandwidths, while transit-time broadening is incorporated in τ_f . The exact line shape is sensitive to additional experimental conditions. For example, chromatic aberrations due to the various lenses in the setup need to be accounted for as the intensity at the focus is wavelength dependent (see caption Fig. 4.3). Using Eq. 4.2 as a fitting function is cumbersome for determining the line centre. However, Eq. 4.2 is a symmetric function. Therefore, fitting any other symmetric function to the data does not introduce a systematic error in determining the line centre. For this purpose we have used a simplified fitting function consisting of a sum of a single Gaussian and Lorentzian for each transition. In this model the widths of the Gaussian and Lorentzian functions are given as free parameters and are not physically meaningful. Nevertheless, this approach is computationally very fast and we verified that it does not lead to a systematic shift in the determination of the line centre. A typical data set including the fitting function and fit residuals is shown in Fig. 4.4. This trace was recorded with a laser bandwidth of 10 nm, which gives the best compromise between signal strength and residual Doppler broadening. The measured

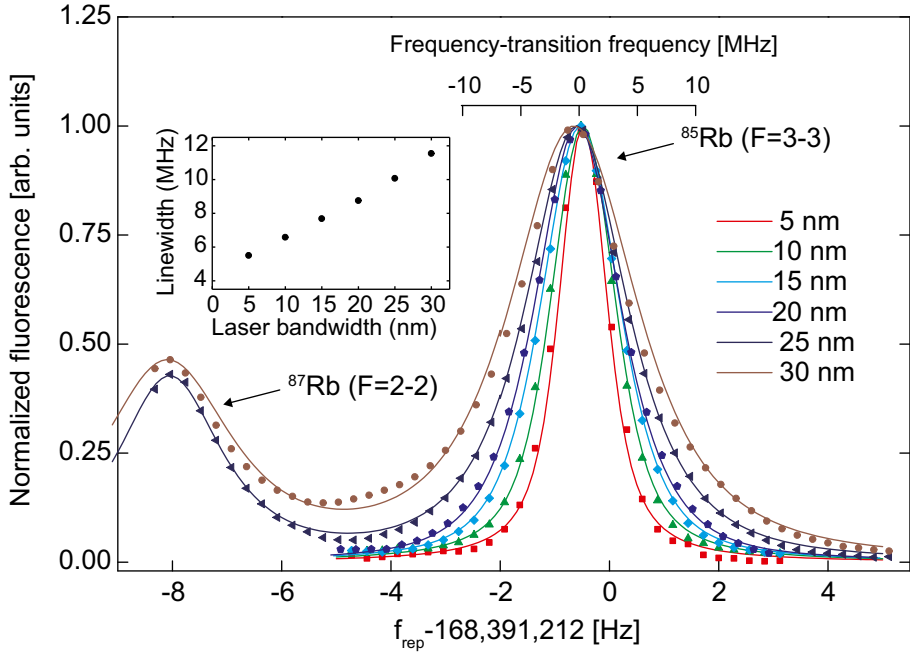


Figure 4.3: Multiple scans of background-free signal over a single transition. The absolute frequency scale presented above the traces is calculated from the comb equation. The solid lines are computed from Eq. 4.2 to show the validity of the line shape model. In these calculations a single Gaussian wavelength-dependent scaling function (FWHM 20 nm) of the intensity was used to account for chromatic aberration due to the lenses used in the experimental setup. Excitation with a larger bandwidth leads to a broader line width, which results in less accurate results and a possible systematic shift due to the overlap with neighbouring transitions. A larger bandwidth also has more optical power, which shifts the transition due to the AC Stark effect. The linear dependence between laser bandwidth and residual Doppler broadening is shown in the inset.

transition line width was 6 MHz FWHM (comparable to the 1.8 MHz natural line width), and the SNR allows a determination of the line centre to better than 1:1000 of the measured line width, limited by shot noise fluctuations. The structureless residuals validate that our model function is successful in accurately determining the line centre.

4.5 Spectroscopy and systematic effects

Before an absolute frequency determination of the individual transitions can be made, all possible systematic shifts need to be quantified and corrected for. Due to the low pulse energy (30-300 pJ) and peak intensity ($<50 \text{ MW/cm}^2$) strong field effects such as multiphoton ionization and self-phase modulation are negligible. The main systematic effects in the present work are pressure effects, magnetic (Zeeman) shift, and AC Stark shifts. Pressure shifts can manifest in two different ways. First, collisions between Rb atoms can shift the transition frequency as a linear function of the pressure in the vapour cell. Previous studies of this effect have shown that the pressure shift is equal to $-103.4(10.0) \text{ kHz/mTorr}$ [109]. As the pressure in our experiment was kept below $2 \times 10^{-5} \text{ mTorr}$, a shift of less than 2 kHz is expected. Impurities in the vapour cell can also lead to systematic shifts. This is more difficult to quantify as the pressure of impurities is hardly affected by changes in the temperature. We take a conservative upper limit for the pressure shift equal to 5 kHz. The shift due to external magnetic fields is small for the measured S to S transitions, as the linear Zeeman shift is zero. However, second-order Zeeman shift of a few kHz/G^2 needs to be taken into account. We apply a correction for the measured transition frequencies derived from calculations of the second-order Zeeman shift [111] due to the uncompensated earth's magnetic field. This shift is different for each transition, ranging from 0.5 to 1.2 kHz.

An additional systematic effect is due to the presence of a light field (AC Stark shift). This shift scales linearly with the average power of the laser [71]. In order to correct for this shift (a few kHz/mW for our experimental conditions) we have performed measurements at different optical powers and extrapolated to zero. This was done for 10 measurement sets of the 5S-7S ($F=3-3$) in ^{85}Rb , leading to an absolute transition frequency of $788\,795\,814\,061.8 \text{ kHz}$ with statistical and systematic uncertainties of 4 and 5 kHz respectively. The transition frequency was corrected for the above-mentioned systematic shifts, including smaller corrections for the second-order Doppler shift (-420 Hz at 60°C) and black body radiation shift (-630 Hz at 60°C). The statistical accuracy is an order of magnitude better than in previous studies of this transition [109].

We have also performed measurements of difference frequencies between the various hyperfine transitions by scanning over all four transitions (Fig. 4.2b) and extracting the difference frequencies. As both AC Stark shift and pressure shift are the same for all 4 transitions, the difference frequencies are insensitive to the laser intensity and gas pressure. The leading systematic uncertainty is then the second-order Zeeman shift which is corrected for in the same way as described above. By combining these relative measurements with the accurately calibrated ^{85}Rb ($F=3-3$) transition, we have determined the absolute

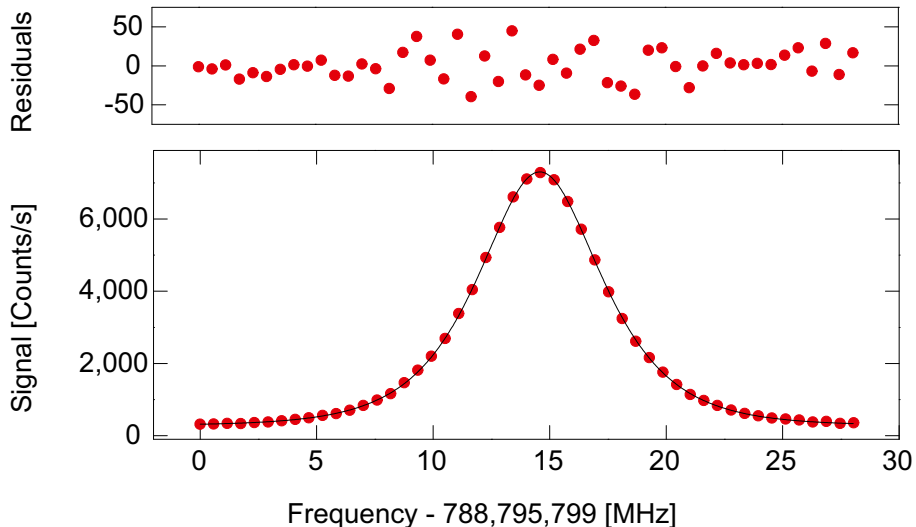


Figure 4.4: A typical recording of the $^{85}\text{Rb}(F=3-3)$ transition. The repetition rate of the FC is chosen such that this line has a maximum distance to the other 3 transitions. The excellent SNR allows determination of the line centre to about 1:1000 of the measured line width.

Table 4.1: A summary of the spectroscopy results. The values in parentheses are the statistical and systematic uncertainties. All values are given in kHz.

Transitions	
$^{85}\text{Rb}(F=3-3)$	788 795 814 061.8(4.0) _{stat} (5.1) _{sys}
$^{85}\text{Rb}(F=2-2)$	788 798 565 752.1(6.4) _{stat} (5.6) _{sys}
$^{87}\text{Rb}(F=2-2)$	788 794 768 940.1(7.2) _{stat} (5.2) _{sys}
$^{87}\text{Rb}(F=1-1)$	788 800 964 119.7(7.2) _{stat} (5.4) _{sys}
Hyperfine A constants	
$^{85}\text{Rb } 7\text{S}$	94 680.7(3.0) _{stat} (2.1) _{sys}
$^{87}\text{Rb } 7\text{S}$	319 751.8(5.0) _{stat} (0.9) _{sys}
Isotope shift	
$^{85}\text{Rb} - ^{87}\text{Rb}$	131 533.2(12.1) _{stat} (8.5) _{sys}

frequencies of all 4 transition, as well as the hyperfine A coefficients and the isotope shift of the upper states (the values of the ground state splittings are taken from [112]). The final results are summarized in Table 4.1.

4.6 Conclusion

In conclusion, we have demonstrated the elimination of Doppler-broadened background, using a simple pulse shaping setup consisting of a grating and two mirrors, which enables high-precision spectroscopy with fs pulses in a counterpropagating beam geometry. DFCS on room-temperature Rb gas was performed with up to a tenfold improvement of the absolute frequencies of 4 two-photon transitions. This technique provides a simple and robust method for high-precision spectroscopy using a single laser. The method is also compatible with XUV comb generation, which opens the perspective of Doppler-reduced two-photon precision measurements in the XUV.

Spatial and spectral coherent control with frequency combs

Quantum coherent control [25, 113, 26, 24, 114, 40] is a powerful tool for steering the outcome of quantum processes towards a desired final state, by accurate manipulation of quantum interference between multiple pathways. Although coherent control techniques have found applications in many fields of science [115, 116, 117, 118, 78, 119], the possibilities for spatial and high-resolution frequency control have remained limited. Here, we show that the use of counterpropagating broadband pulses enables the generation of fully controlled spatial excitation patterns. This spatial control approach also provides decoherence reduction, which allows the use of the high frequency resolution of an optical frequency comb [56, 55]. We exploit the counterpropagating geometry to perform spatially selective excitation of individual species in a multi-component gas mixture, as well as frequency determination of hyperfine constants of atomic rubidium with unprecedented accuracy. The combination of spectral and spatial coherent control adds a new dimension to coherent control with applications in e.g nonlinear spectroscopy, microscopy and high-precision frequency metrology.

5.1 Introduction

In traditional coherent control experiments pulse shaping techniques [73] are used to steer light-matter interaction by manipulating the relative phases between different quantum paths leading to the same final state. Numerous control schemes have been shown in the past to provide frequency control and selectivity with a resolution exceeding the bandwidth of the individual pulses by 2-3 orders of magnitude. The vast majority of these schemes rely on a two-photon interaction with a single broadband shaped pulse. Even though the laser systems used in these experiments produce trains of pulses, decoherence effects due to the atomic motion wash out the interference between different pulses, and therefore blur the underlying atomic structure. Spatially, the interaction with a single shaped pulse creates a signal that is practically identical along the whole beam path.

Here, we demonstrate how the control level of light-matter interaction is significantly enhanced by the interaction with multiple pulses. First, we show that the addition of a counterpropagating pulse changes the quantum interference and can even invert the properties of the excitation. In combination with pulse shaping techniques this geometry provides full spatial control and is able to produce complex excitation patterns over an extended region. Second, excitation from counterpropagating beams inherently reduces decoherence effects, allowing coherent accumulation of quantum interference over long pulse trains, even without the use of cooling techniques [67]. Combined with the excellent phase stability of an optical frequency comb, this enables high-resolution excitation which is able to resolve the smallest features of the atomic structure.

5.2 Theory

To gain insight in the properties of spatial control, we derive an analytical expression for the spatial excitation pattern. Consider the two-photon interaction of a simple two-level atom with a light field $E(t)$, where the two photons originate from counterpropagating ultrashort pulses. Atoms at different positions experience the two counterpropagating pulses at different times with a delay $t = 2z/c$ ($z = 0$ is the point where the unshaped pulses overlap and c is the speed of light). The excitation probability from counterpropagating pulses can be written in the following way (complete derivation in section 5.8):

$$S_{2p}(z) = \int d\omega' \int d\omega'' A(\omega')A(-\omega')A(\omega'')A(-\omega'') \times \exp \left[i \left\{ \phi(\omega') + \phi(-\omega') + \phi(\omega'') + \phi(-\omega'') + \frac{2z}{c}(\omega' - \omega'') \right\} \right] \quad (5.1)$$

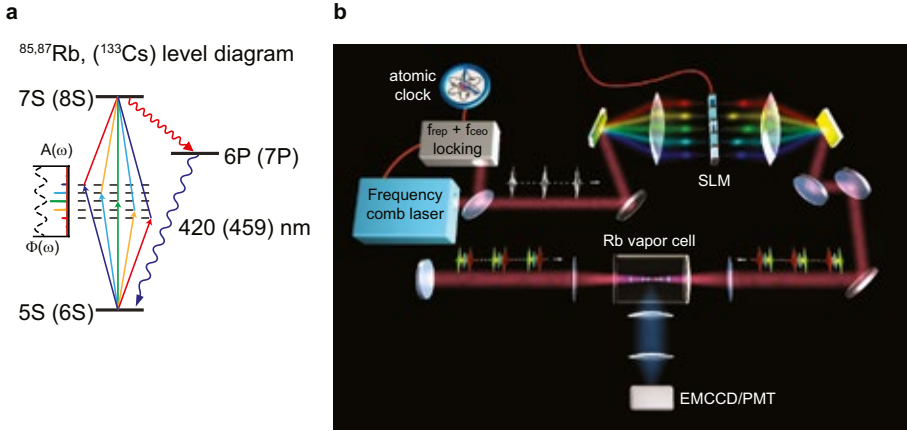


Figure 5.1: Level diagram and schematic of the experimental set-up. a, Energy level diagram of atomic rubidium (caesium). Pairs of frequency comb modes excite the 5S-7S (6S-8S) transition. Fluorescence from the 6P (7P) state at 420 nm (459 nm) is used for monitoring the excited state population. b, Schematic of the experimental set-up. Each pulse from a frequency comb laser is shaped using a spatial light modulator (SLM) in the Fourier plane of a zero-dispersion 2f-2f configuration. Every two consecutive pulses overlap in the middle of the vapour cell. The fluorescence pattern is imaged onto an electron-multiplying charge-coupled device (EMCCD) camera or a photomultiplier tube (PMT).

where $A(\omega)$ is the spectral amplitude and $\phi(\omega)$ is the spectral phase at a frequency ω of the laser field, relative to half the transition frequency ($\omega_0/2$). The appearance of the fields $A(\omega)$ and $A(-\omega)$ in the integral reflects the fact that many pairs of different spectral modes centred around $\omega_0/2$ are involved in the two-photon transition.

Some distinct properties of the excitation profile can be derived even without full evaluation of this integral. In the case of an anti-symmetric phase function ($\phi(\omega) = -\phi(-\omega)$), the phase dependent terms in the exponent of each integral cancel. The excitation probability will therefore be identical to the case of transform-limited pulses which is a similar behaviour as observed in the single beam configuration [38]. A new level of control is made possible by applying symmetric spectral phase masks, which results in the generation of complex spatial patterns. Remarkably, when Eq. 5.1 is integrated over the spatial dimension (simulating a position-insensitive detector), all phase terms drop out, resulting in optimal constructive interference. The spatial excitation pattern can thus be manipulated without affecting the total signal strength.

5.3 Setup

As a proof-of-principle we conducted measurements on various two-photon transitions in atomic rubidium and cesium (level diagrams are presented in Fig. 5.1a). The experimental setup is shown in Fig. 5.1b. Briefly, femtosecond pulses from a frequency comb laser are spectrally shaped in a standard phase-only $2f - 2f$ configuration. The shaped pulses are focused in a vapour cell containing either pure Rb or a Rb-Cs mixture. After passing the cell, the pulses are reflected back at a distance that matches the repetition frequency of the laser, so that every two consecutive pulses overlap in the middle of the vapour cell. Control over the atomic excitation is achieved by applying a spectral phase mask to the pulse shaper and tuning the frequency comb parameters f_{rep} (repetition frequency) and f_0 (carrier-envelope offset frequency) which determine the absolute frequencies of the frequency comb modes through the comb equation $f_n = f_0 + n \times f_{rep}$ [56, 55], where n is an integer. The excited state population is monitored by detecting the 420 nm (459 nm) fluorescence upon spontaneous decay via the 6P (7P) state in rubidium (caesium).

5.4 Spatial control with sinusoidal phase modulation

We first applied a harmonic spectral phase mask, $\phi(\omega) = \alpha \cos(\beta\omega + \varphi)$, where α is the modulation depth, β is the modulation frequency and φ is the modulation phase. We investigated the influence of this class of spectral phase masks on the excitation from single-sided and counterpropagating pulses. A pure Rb vapour cell was used, and the comb parameters were set to excite the $^{85}\text{Rb } 5S(F=3) \rightarrow 7S(F=3)$ transition. As a reference, a fluorescence image of the excitation pattern resulting from transform-limited pulses ($\alpha = 0$) is shown in Fig. 5.2a. Transform-limited pulses lead to optimal constructive interference of single-sided excitation, giving rise to a strong spatially-independent signal. The localised signal in the centre results from the spatial overlap of two counterpropagating transform-limited pulses.

A harmonic spectral phase mask alters the temporal intensity distribution of the pulses, breaking each pulse into a train of sub-pulses. In Fig. 5.2b a sine-modulated spectral phase ($\varphi = \pi/2$, anti-symmetric relative to $\omega_0/2$) is applied with modulation depth of $\alpha = 1.2$. An anti-symmetric spectral phase does not influence the single-sided excitation [38], which appears in our case as an unchanged, spatially independent background. We observe that the localised signal resulting from counterpropagating pulses is also unaffected by an anti-symmetric phase, as predicted from Eq. 5.1. Although the sub-pulses overlap in multiple regions in space, the quantum interference is only constructive in the centre.

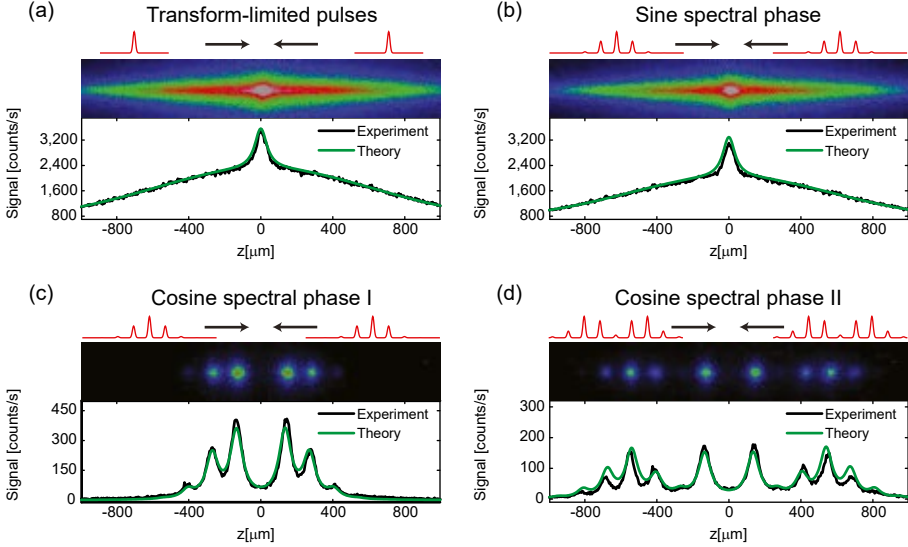


Figure 5.2: Experimental demonstration of spatial coherent control using four different phase masks. a-d, Transform-limited pulses (a), antisymmetric sine-modulated spectral phase ($\alpha=1.2$, $\beta=900$ fs, $\varphi=\pi/2$) (b), symmetric cosine-modulated spectral phase ($\alpha=1.2$, $\beta=900$ fs, $\varphi=0$) (c) and symmetric cosine-modulated spectral phase with a larger amplitude ($\alpha=2.76$, $\beta=900$ fs, $\varphi=0$) (d). For each figure we present the temporal intensity profile (depicted in red) of the counterpropagating pulses and the observed spatial excitation pattern. A cross-section of each fluorescence image is compared to a numerical evaluation of equation 5.1 (green line). The broadening of the data due to the imaging resolution and the atomic motion is taken into account in the theory by convolving all simulation curves with the same 80 nm full-width at half-maximum Lorentzian distribution. A correction for the non-uniform intensity due to the focusing geometry is derived by fitting the background with a single Gaussian distribution. The resulting correction (including a single scaling factor) is then applied to all theoretical curves.

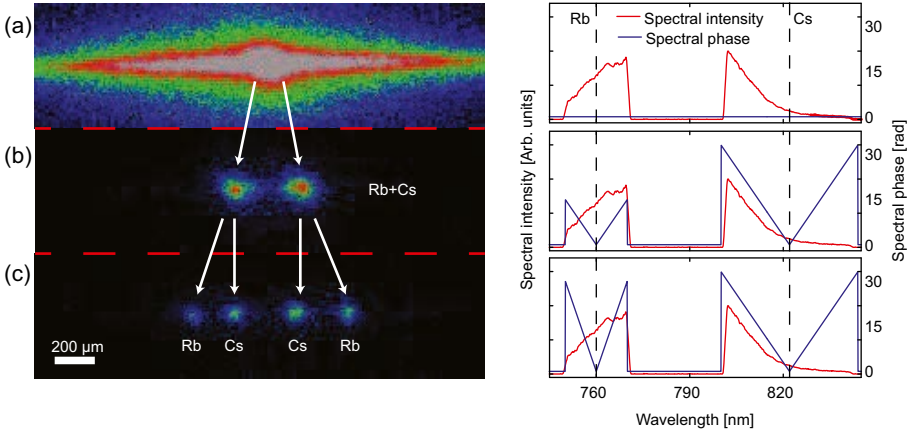


Figure 5.3: Spatial coherent control of different atomic species. a, Spatial excitation patterns using transform-limited pulses. b, Double V-shaped spectral phase mask ($\phi(\omega)=\alpha|\omega - \omega_0/2|$) with $\alpha=0.5$ ps for both spectral regions. c, Double V-shaped spectral phase mask with $\alpha=0.5$ ps for caesium and $\alpha=1.1$ ps for rubidium. All images were taken with the same comb parameters.

Figure 5.2c shows an image of the excitation pattern when applying a symmetric phase mask ($\varphi = 0$) with the same modulation depth and modulation frequency as in Fig. 5.2b. Even though the temporal intensity distributions of the interacting pulses for Figs. 5.2b and 5.2c are identical, the resulting spatial excitation patterns differ substantially. For this symmetric phase mask, the single-sided excitation is completely eliminated, which is why such pulses have been named “dark pulses” [38]. However, Fig. 5.2c shows that counter-propagating dark pulses actually give rise to a spatially structured two-photon excitation pattern where the sub-pulses overlap. We find that these counter-propagating dark pulses are not only not dark, but induce the same total excitation as transform-limited pulses.

Variation of the modulation depth can be used as a “switch” to turn the single-sided signal on and off, but also to control the relative brightness of the individual excitation regions. In Fig. 5.2d the modulation depth was set to $\alpha = 2.76$, where the single-sided signal is again completely eliminated. The fluorescence image displays additional excitation regions with different ratios between their relative intensities. In addition, the positions of the excitation regions can be controlled by varying the modulation frequency β (see section 5.8).

5.5 Spatial selectivity of atomic excitation

In the second set of measurements we illustrate the versatility of spatial coherent control by spatially separating the excitation of different atomic species. We use a Rb-Cs mixture vapour cell and tune the comb parameters to $f_0=25$ MHz and $f_{rep}=178,435,286$ Hz, for which both the $^{85}\text{Rb } 5S(F=3) \rightarrow 7S(F=3)$ transition in rubidium at 2×760 nm and the $^{133}\text{Cs } 6S(F=4) \rightarrow 8S(F=4)$ transition in caesium at 2×822 nm are simultaneously excited. Figure 5.3a shows the excitation profile with transform-limited pulses. The signal is dominated by single-sided excitation where no distinction between the atomic species can be made. Subsequently, we employ a V-shaped spectral phase mask ($\phi(\omega) = \alpha|\omega - \omega_0/2|$) that effectively eliminates the single-sided signal. By applying such a spectral phase mask to both spectral regions (centred around $\lambda_{\text{Rb}} = 760$ nm and $\lambda_{\text{Cs}} = 822$ nm), we create a background-free excitation pattern as seen in Fig. 5.3b. Changing the slope of the V-shaped phase masks, the excitation position of the individual species can be moved around independently. This results in controlled spatially separated excitation of rubidium and caesium atoms, as seen in Fig. 5.3c. We verify that the excitation within the various regions in Fig. 5.3c originates from different atomic species by scanning the frequency comb modes over the different atomic transitions. Such a scan reveals the hyperfine atomic structure, which is a unique fingerprint of the different atoms (for details see section 5.8).

5.6 Background-reduced spectroscopy

The combination of background-free signal with the reduction of Doppler-broadening [4, 69] is essential for performing high-precision direct frequency comb spectroscopy [64, 58, 62, 60, 59, 107]. These requirements are easily satisfied by using counterpropagating frequency comb pulses with a V-shaped spectral phase. The laser spectrum is clipped in the Fourier plane of the shaper in order to only excite the Rb atoms. In Fig. 5.4 the spatially integrated signal is shown as a function of the comb repetition frequency. The excellent signal to noise ratio enables us to determine the hyperfine A constants of the excited state in ^{85}Rb and ^{87}Rb to be 94,686(7) kHz and 319,713(30) kHz, respectively. Simultaneously measuring both isotopes also permits accurate determination of the isotope shift. We find the isotope shift of the $5S \rightarrow 7S$ transition to be 131,564(20) kHz. This presents the most accurate measurement of these values, outperforming other direct frequency comb measurements [59] and even CW laser measurements [109] (The analysis procedure and a comparison of our results with previous measurements are presented in section 5.8).

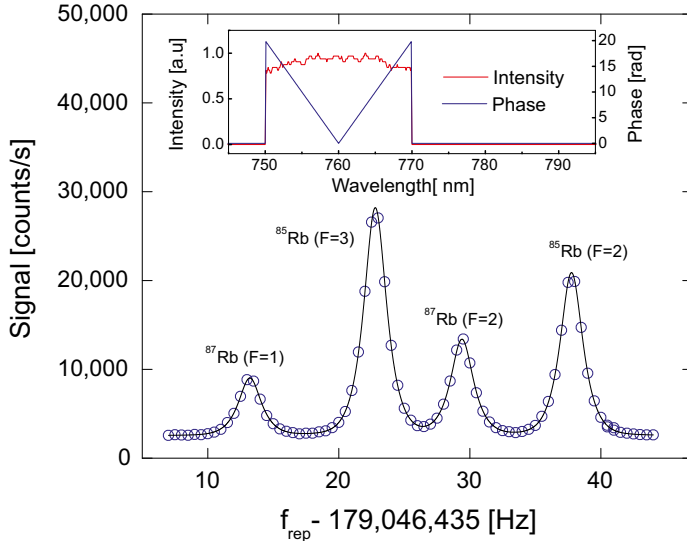


Figure 5.4: Direct frequency comb spectroscopy of atomic rubidium with spatial coherent control. Fluorescence signal induced by the four hyperfine transitions as a function of comb repetition frequency (f_0 is kept constant at 10 MHz, level structure as shown in Fig. 5.7). The spectrum and phase used for this measurement are shown in the inset, and the signal is measured with a position-insensitive photomultiplier. The various transitions are excited with different comb modes. A projection of the data on an absolute frequency axis is shown in Fig. 5.8.

5.7 Conclusion

The combination of spatial and spectral coherent control opens new possibilities for a wide range of applications including nonlinear spectroscopy, microscopy and high-precision frequency metrology. For example, selective excitation of specific ions in a trap can be achieved with high precision. The ability of spatial coherent control to excite different transitions at distinct positions in space can for instance be exploited for spatially-dependent chemical bond formation or dissociation. Additionally, shaping only one of the two counterpropagating pulses can be used as a type of pump-probe measurement where the delay between the pump and the probe is mapped to the spatial dimension. Combined with spatially sensitive detection, signal from all possible delays can be

acquired in a single shot. The combination of line by line shaping [120, 121] with our principle of spatial coherent control could lead to optical arbitrary waveform generation in space and time.

5.8 Supplementary information

Derivation of Eq. 5.1

The excitation probability of a two-photon transition from a single pulse can be written as [38]:

$$S_{1p}(z) = \left| \int d\omega' A(\omega') A(-\omega') e^{i(\phi(\omega') + \phi(-\omega'))} \right|^2 \quad (5.2)$$

In the present work we are interested in the excitation due to counterpropagating pulses. Atomic excitation occurs due to the perturbation of the atomic wave function by an electromagnetic field. The direction of the electromagnetic field does not affect the excitation probability (ignoring effects of momentum transfer). Therefore, at each point z the excitation probability is the same as copropagating pulses with a time delay $\Delta t = \frac{2z}{c}$. This time delay is incorporated by adding a linear spectral phase $\phi(\omega) \rightarrow \phi(\omega) \pm z\omega/c$. Equation 5.2 then becomes:

$$S_{sp}(z) = \left| \int d\omega' A(\omega') A(-\omega') e^{i(\phi(\omega') + \phi(-\omega') + 2\frac{\omega'z}{c})} \right|^2 \quad (5.3)$$

We rewrite Eq. 5.3 as a product of the integral and its complex conjugate and rearrange the integrals to acquire the following result:

$$S_{2p}(z) = \int d\omega' \int d\omega'' A(\omega') A(-\omega') A(\omega'') A(-\omega'') \times \exp \left[i \left\{ \phi(\omega') + \phi(-\omega') + \phi(\omega'') + \phi(-\omega'') + \frac{2z}{c}(\omega' - \omega'') \right\} \right]. \quad (5.4)$$

If this signal is observed with a position-insensitive detector, the total signal is found by integration of Eq. 5.4 over the spatial coordinate z . However, the last term in Eq.5.4 represents the definition of a delta distribution when integrating over z . Therefore only components where $\omega' = \omega''$ lead to a nonzero contribution in this case. The total signal is then equal to:

$$S_{total} = \int_{-\infty}^{\infty} dz S_{2p}(z) = \int_{-\infty}^{\infty} d\omega A(\omega)^2 A(-\omega)^2 \quad (5.5)$$

The consequence of this result is that the total (spatially integrated) signal due to counterpropagating pulses is independent of the specific form of the applied spectral phase.

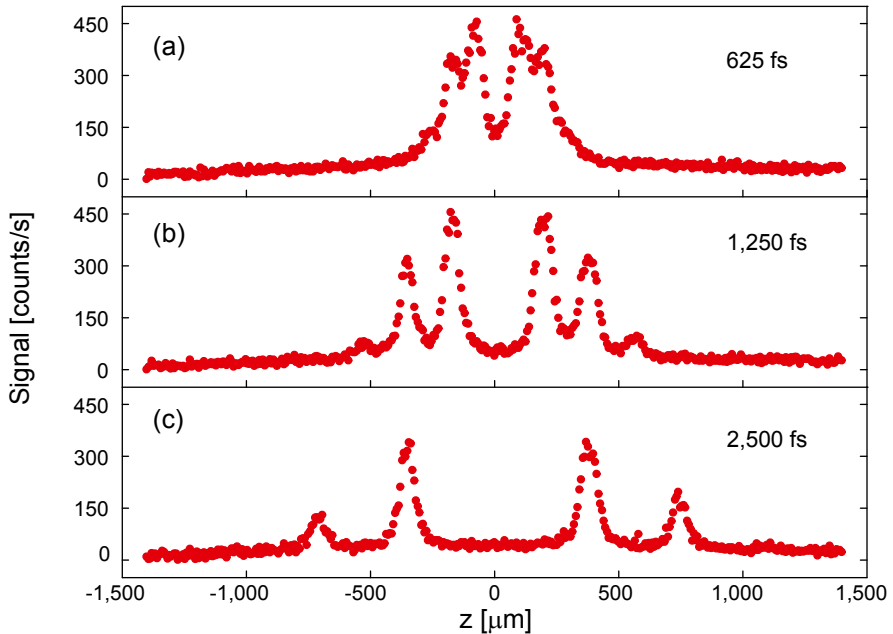


Figure 5.5: Influence of the modulation frequency on the spatial excitation pattern. The spectral phase mask applied to the pulses is of the form $\phi(\omega) = 1.2 \cos(\beta\omega)$. The modulation amplitude was set to 1.2 in order to eliminate the background from single-sided excitation. The modulation frequency is (a) 625 fs, (b) 1250 fs and (c) 2500 fs. All graphs were acquired by taking a line-out of fluorescence images, in the same way as in Fig. 5.3.

Variation of the modulation frequency

In this section we show how the excitation regions can be moved by changing the frequency of the phase modulation. We employ spectral phase masks of the form $\phi(\omega) = 1.2 \cos(\beta\omega)$ and use β as a control parameter. The amplitude was set to 1.2 for elimination of the single-sided excitation. This type of harmonic phase breaks the original pulses into sub-pulses separated by $\Delta z = \beta c$ where c is the speed of light. The counterpropagating sub-pulses in discrete spatial positions separated by $\beta c/2$.

The results are presented in Fig. 5.5. Each trace corresponds to a different modulation frequency and the data is measured by taking a line-out from the centre of fluorescence images as described in the main text. The distance between the interaction regions agrees very well with the expected values. The

height of the signal at the various regions is predicted not to depend on the modulation frequency. The reduction of signal for large values of β is simply explained by the decrease of intensity away from the focus of the two beams.

Spatially separated excitation of different atomic species

As mentioned in the main text, the image in Fig. 5.3c was taken when the comb parameters were set to excite both atomic species simultaneously. We have taken fluorescence images at different values of the repetition frequency (e.g. the images in Fig. 5.6). The images were divided into 4 regions where the atomic excitation takes place. As the laser repetition frequency was changed we observed the signal from regions 1+4 and 2+3 varying independently. Integration of regions 1+4 (red trace) and 2+3 (green trace) clearly shows that different atomic species are excited at different positions. We also identified the various transitions by comparison to their known absolute frequencies.

Analysis of the spectroscopy results

The atomic hyperfine constant A is defined through $E=A/2 (F(F+1)-I(I+1)-J(J+1))$ where I , J and F are the nuclear spin, atomic angular momentum and total angular momentum, respectively. E is the energy shift as a consequence of interaction between the atomic and nuclear angular momentum. Figure 5.7 shows the energy level diagram of the relevant transitions. We note that only transitions where $\Delta F=0$ are allowed due to atomic selection rules.

The energy splitting of the ground state of ^{85}Rb and ^{87}Rb has been previously measured with Hz level accuracy [112]. Therefore measuring the two allowed transitions for each isotope enables the determination of the energy splitting of the upper state and thus the hyperfine A constant. Knowledge of the hyperfine A constants can also be used to determine the transition isotope shift (see Fig. 5.7).

It is not necessary to measure the absolute transition frequencies individually as only the difference between the transition frequencies is in the end required here. This greatly reduces the sensitivity for systematic errors, because for the measured transition differences, the Zeeman, light and pressure shifts are expected to cancel well within the statistical measurement accuracy we achieved. Furthermore, frequency comb excitation is ideal for relative frequency measurements because different transitions are excited by different comb modes. While cw lasers have to be scanned over many GHz in order to measure different hyperfine transition, all the transitions are measured with a scan of tens of Hz of the comb repetition frequency. Such a scan is presented in Fig. 5.8 (upper panel). Because the absolute transition frequencies have been measured in the past with accuracy better than the comb mode spacing (f_{rep}), the mode numbers driving the transitions can be inferred. In Fig. 5.8 (lower panel) the

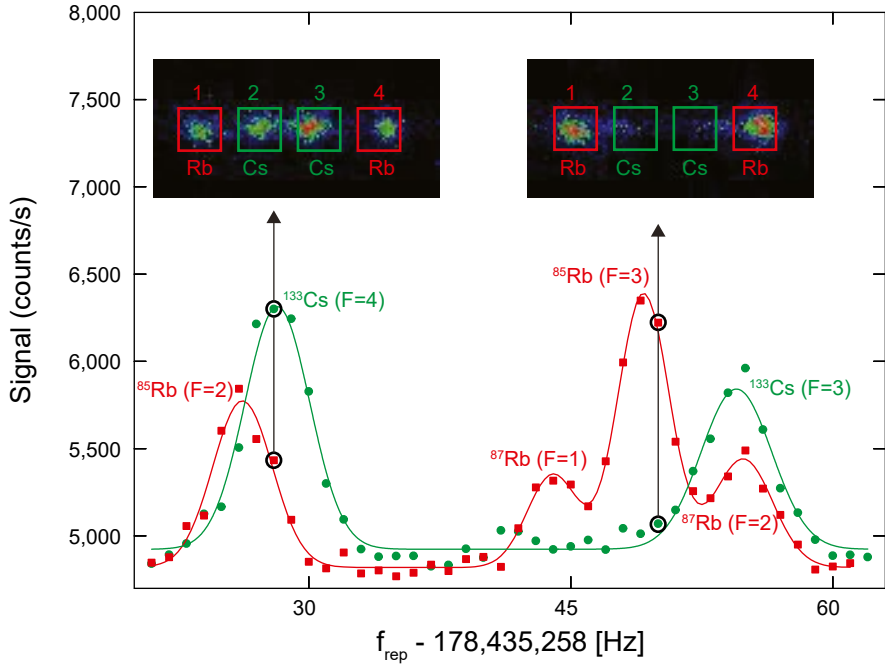


Figure 5.6: High-precision spatial and spectral control of multiple atomic species. (upper images) Spatial excitation patterns of specific hyperfine transitions in atomic rubidium and caesium. The two images were taken with two different comb repetition rates, as indicated by the black arrows. (graph) Integrated signal from regions 1+4 (red curve) and 2+3 (green curve) as a function of the repetition rate. The experimental conditions required a high gain of the EMCCD, resulting in strong background due to stray light. This constant background was subtracted from the fluorescence images for visualisation purposes.

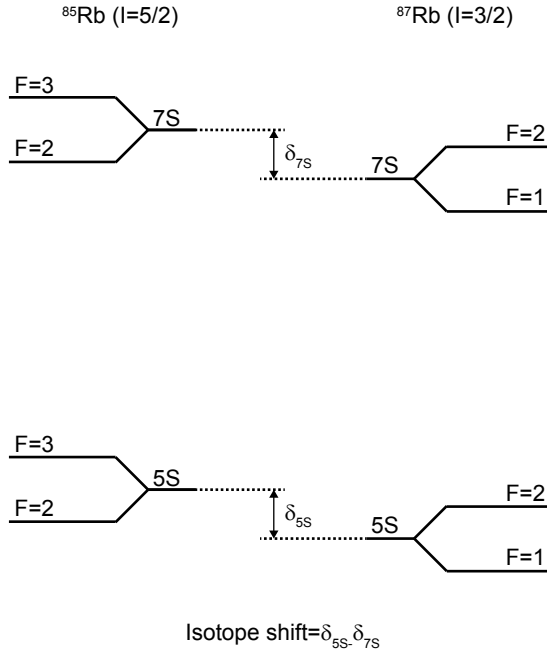


Figure 5.7: Energy level diagram of the measured hyperfine transitions in atomic rubidium.

results are shown on an absolute frequency axis. The measured linewidth of the individual transitions is about 8 MHz (compared to a Doppler width of 450 MHz). This is roughly 4 times broader than the natural linewidth (1.8 MHz), which can be explained by residual Doppler broadening due to excitation from mode pairs with unequal frequencies.

The analysis procedure consisted of fitting the 4 transitions simultaneously. The excellent signal to noise ratio permitted the determination of the transition frequencies better than 1/200 of the measured linewidths. As mentioned earlier, even though the absolute transition frequencies depend on the laser intensity (AC Stark shift, which can be at a level of 100 kHz at the highest power levels, depending on the focusing geometry) and applied magnetic field (Zeeman shift), these shifts are the same for all transitions such that the difference remains unchanged. We have tested this experimentally by repeated measurements at different light intensities (from 10 to 60 mW) and magnetic fields (up to about 2 Gauss). Also several different gas cells at different temperature were

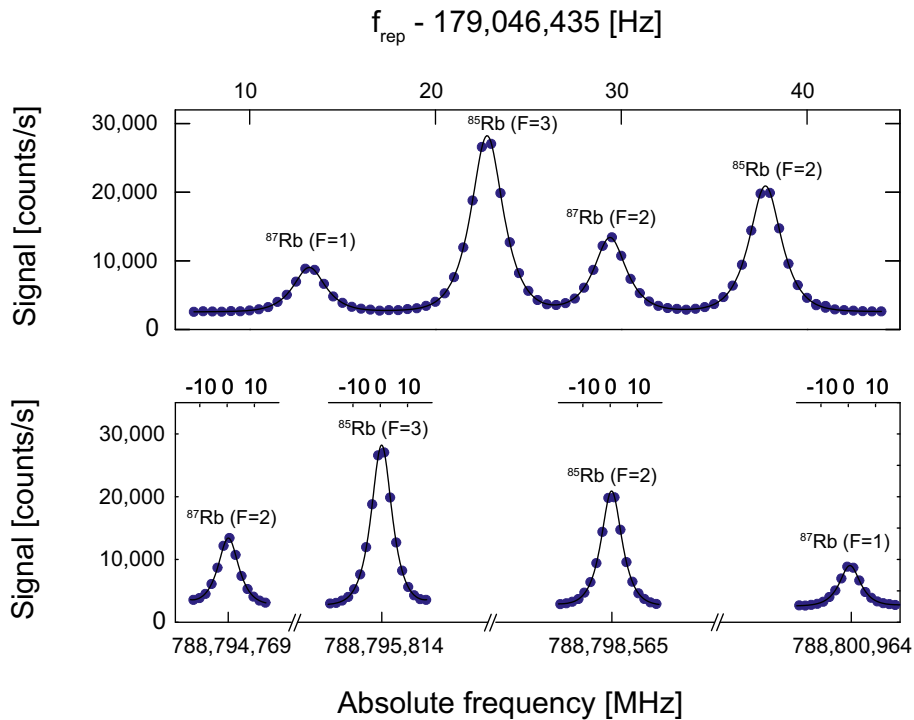


Figure 5.8: Frequency comb excitation. (upper panel) Integrated fluorescence as a function of the comb repetition frequency. (lower panel) The same data on an absolute frequency scale.

used to exclude (background) pressure effects. We observed no systematic shift within the statistical error of our measurements, therefore the error in hyperfine constants and isotope shift is based on the statistical error alone. The final results are summarised in table 5.1.

Table 5.1: Comparison of this work with previous measurements (all values in kHz). The various measurements schemes are: direct frequency comb resonantly-enhanced excitation by Marian et al. [59], CW laser excitation with equal photons by Chui et al. [109], and direct frequency comb excitation without intermediate resonant excitation (present work).

	Marian et al [59]	Chui et al [109]	Present work
^{85}Rb A constant	-	94,658(19)	94,686(7)
^{87}Rb A constant	319,702(65)	319,759(28)	319,713(30)
^{87}Rb - ^{85}Rb 5S-7S isotope shift	-	131,567(73)	131,564(20)

Counterpropagating resonant two-photon absorption

In this chapter we explore the possibilities of controlling the competition between resonant and nonresonant pathways in two-photon transitions. We identify that the resonant and nonresonant pathways behave differently when excited by counterpropagating frequency comb pulses, as they are influenced differently by the Doppler effect. This is used as a control parameter to manipulate the quantum interference between the various excitation pathways. The complex spatial excitation patterns that result from the counterpropagating frequency comb pulses are manipulated by applying a V-shaped phase mask. We show that such a spectral phase manipulation leads to a spatially dependent ratio between resonant and nonresonant pathways.

6.1 Introduction

Since the advent of laser spectroscopy, two-photon transitions have played an important role in improving measurement accuracy [13, 11]. Two-photon transitions can be thought to consist of two one-photon transitions that occur via an intermediate state. For the transition to take place, the sum of the two photons must match the energy difference between the ground state and the final state. Regarding the energy of the intermediate state, there are two distinct situations that also result in a different behaviour of the excitation. In the first case, called resonant two-photon excitation, the energy of one of the two photons matches the energy of the intermediate state. The atom is actually excited to the intermediate state before being excited to the final state. The time between absorbing the first and the second photons does not play an important role (as long as it is within the lifetime of the intermediate state). In the second case, called nonresonant two-photon excitation, the energy of the intermediate state does not match either one of the photons. The intermediate state is not actually populated in this process and the atom is directly excited to the upper state. Clearly, for this transition to happen, the two photons must overlap in time. An important property of nonresonant two-photon excitation is that the transition amplitude is inversely proportional to the energy mismatch between the photon energy and the energy of the intermediate state.

The reason that two-photon transitions have become so important in laser spectroscopy is the possibility to cancel first-order Doppler effects by using a counterpropagating excitation geometry, which enables an improved measurement accuracy. Liao and Bjorkholm [5, 105] have investigated the properties of two-photon transitions and the differences between resonant and nonresonant excitation, while other research groups have used two-photon transitions to perform high-accuracy Doppler-free spectroscopy [4, 100, 69, 70].

When driving two-photon transitions, the use of ultrashort pulses enables new and exciting possibilities. As ultrashort pulses contain a broad spectral bandwidth, it is therefore possible to simultaneously excite the transition with different combinations of frequencies to the same final state. The quantum interference between these pathways have shown to present remarkable characteristics and has been investigated by many different research groups [26, 24, 36]. One of the interesting questions in this field of research regards the nature of the competition between resonant and nonresonant pathways. Several papers have concentrated on this question [40, 94] and devised ways to manipulate this interaction. The difficulty in these kind of experiments is that the spectral resolution of both amplitude and phase is very poor, which makes it difficult to manipulate the resonant pathways without affecting the nonresonant pathways. In this chapter we explore the possibilities to perform coherent control exper-

iments by using counterpropagating frequency comb pulses to alter the interference between resonant and nonresonant pathways. The combination of the counterpropagating geometry and the use of a frequency comb provides high spectral resolution and the ability to change the ratio between the strength of the resonant and nonresonant pathways. This chapter is divided into 3 parts. In the first part we measure the spectral properties of the resonant and nonresonant excitation by scanning the frequency comb modes. In the second part we look into the spatial excitation pattern when both types of pathways are excited simultaneously. In the third part we combine the spectral and the spatial properties of the excitation to analyse the composition of the various pathways at different locations of the excitation pattern.

6.2 Experimental setup

For the experiments in this chapter we use a frequency comb laser which is based on a modelocked Ti:sapphire oscillator where the comb parameters are locked in the same way as described in chapter 5. The cavity dispersion is tuned for a broadband operation with a central wavelength around 760 nm and a bandwidth of about 120 nm FWHM. The comb pulses are shaped in a dispersion-free 4f pulse shaper where a spectral phase mask is applied in the form of $\phi(\omega) = \frac{\tau}{2}|\omega - \frac{\omega_c}{2}|$. After the pulse shaper the pulses are split and directed in a counterpropagating geometry to overlap spatially and temporally at the centre of a Rb-filled gas cell. The gas cell is heated to a temperature of about 80° C in order to increase the density and therefore the signal. The shaped comb pulses are used to excite the $5S \rightarrow 7S$ transition at 2×760 nm via the $5P_{1/2}$ intermediate resonance at 795 nm. To avoid excitation via other one-photon transitions, the spectrum is clipped at the Fourier plane of the pulse shaper to 2 regions of 15 nm width centred around 795 nm and 729 nm. The population excited to the 7S state is monitored by measuring the fluorescence via the 6P state (42 nm) with both a PMT and an EMCCD camera, which are placed perpendicular to the laser propagation direction. This enables us to measure the total signal, as well as the excitation pattern.

6.3 Part 1: Spectral properties of two-photon excitation

In the first part of this chapter we describe the spectral properties of the resonant and nonresonant pathways in two-photon transitions. In particular, we show that these pathways present a different behaviour when the transition is excited in the counterpropagating geometry compared to the copropagating geometry discussed in chapter 3. We use this as a control parameter to

tune the ratio between resonant and nonresonant pathways that are excited simultaneously.

Nonresonant pathways

We consider a 3-level atom with a ground, intermediate and upper-level denoted with (E_g, E_i, E_t) , respectively. The two-photon transition frequency is represented by ω_t while the transition frequency to the intermediate state is given by ω_i . If the two-photon transition is driven by two counterpropagating frequencies ω_1 and ω_2 then the resonance condition can be written as:

$$\omega_t = \omega_1 + \omega_2 + (\omega_1 - \omega_2)v/c, \quad (6.1)$$

where v is the velocity of the atom in the lab reference frame. If both frequencies originate from the same frequency comb then they are related to each other by the comb equation (Eq. 2.45). The resonance condition can then be written as:

$$\omega_t = 2\omega_0 + (n_1 + n_2)\omega_{rep} + (n_1 - n_2)\omega_{rep}v/c. \quad (6.2)$$

For a low density isotropic gas in a cell that is kept at a constant temperature, the two-photon excitation spectrum is expected to be a Gaussian with a FWHM of:

$$\Delta\omega_{FWHM} = 2\sqrt{\ln 2} \omega_{rep}|n_1 - n_2|v_m/c, \quad (6.3)$$

where $v_m = \sqrt{2k_B T/M}$ is the most probable velocity of atoms with mass M at temperature T . So far we considered only a single pair of frequency comb modes. In practice all combinations of mode numbers must be taken into consideration in order to calculate the complete excitation spectrum. This has been done in chapter 4 for the case that the intermediate state frequency ω_i is far away from the laser spectrum. In that case all pairs of frequencies contribute equally to the transition amplitude. However, in the situation considered in this chapter, the laser spectrum covers the frequency ω_i . In Chapter 3 we have seen that the contribution of a frequency pair to the transition amplitude increases when the frequency of one of the photons gets closer to ω_i . In practice, the dominance of a narrow band around ω_i will be so strong that the laser spectrum can be approximated by assuming a spectrum near ω_i with a few nanometers of bandwidth. For all pairs of frequencies within this bandwidth, the residual Doppler width (Eq. 6.3) is practically the same. The resulting excitation profile is expected to be a single Gaussian where the mode numbers n_1 and n_2 satisfy:

$$\begin{aligned} n_1 &\approx \omega_i/\omega_{rep} \\ n_2 &\approx (\omega_t - \omega_i)/\omega_{rep} \end{aligned} \quad (6.4)$$

A simulation of the excitation profile due to the nonresonant pathways is presented in Fig. 6.1a, for the $^{85}\text{Rb}(5\text{S} [F=3] \rightarrow 7\text{S} [F=3])$ transition. The repetition

frequency of the laser was chosen at ≈ 125 MHz to match the experimental conditions of the results that will be shown later. In the figure there are two broad resonances visible, each one corresponding to a different combination of comb modes that satisfy the resonance condition. The width of the broad resonance, as defined in Eq. 6.3, is equal to 46.7 MHz, which is more than 10 times broader than the natural line width. This shows that the residual Doppler effect is the dominating broadening effect. The width is a direct consequence of the frequency difference between ω_i and $\omega_t - \omega_i$, and cannot be strongly influenced experimentally. Even though the width of each resonance is fixed, the overlap between neighbouring peaks can be changed. This can be done by increasing the repetition frequency of the comb laser. For example, if f_{rep} is increased to 250 MHz then the separation between the peaks is doubled. For the experiment described in this chapter the repetition frequency was chosen such that there is minimal overlap between consecutive peaks.

Resonant pathways

In the process of resonant (stepwise) two-photon excitation, the atom actually undergoes two separate excitation processes with two distinct resonance conditions. For the excitation to take place, the frequency of one of the photons needs to be resonant with the transition to the intermediate state. At the same time, the second photon must be resonant with the transition from the intermediate state to the upper state. In the case of counterpropagating photons (ω_1, ω_2) the resonance conditions can be written as:

$$\begin{aligned}\omega_i &= \omega_1(1 + v/c), \\ \omega_t &= \omega_1 + \omega_2 + (\omega_1 - \omega_2)v/c.\end{aligned}\tag{6.5}$$

Following the same step as in the previous section, if the two photons originate from the same frequency comb then their frequencies are related through the comb equation. The resonance conditions are then:

$$\begin{aligned}\omega_i &= (\omega_0 + n_1\omega_{rep})(1 + v/c), \\ \omega_t &= 2\omega_0 + (n_1 + n_2)\omega_{rep} + \omega_{rep}(n_1 - n_2)v/c.\end{aligned}\tag{6.6}$$

The stepwise excitation can be understood in the following way. The Doppler width of the $5S \rightarrow 5P$ transition in Rb, at around room temperature, is about 1 GHz. Therefore, different velocity classes will be excited to the intermediate level by different modes of the frequency comb propagating from one direction. At the same time, frequency comb modes of the counterpropagating beam will only be resonant for specific velocity classes from the intermediate state to the final state. Due to the large frequency mismatch between these counterpropagating photons, only one velocity class can be excited for each value of

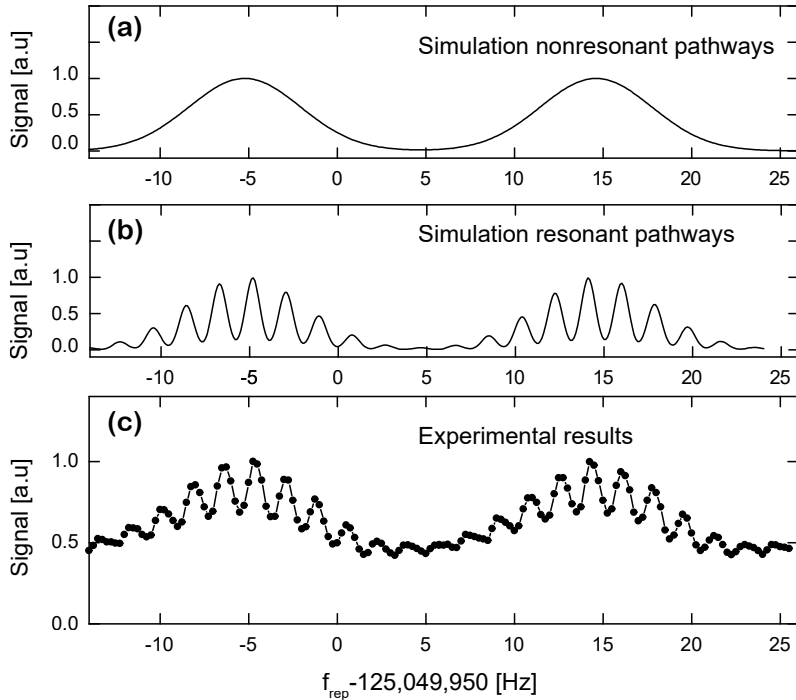


Figure 6.1: Resonant and nonresonant pathways in two-photon transitions. (a) a simulation of the excitation due to nonresonant pathways. (b) a simulation of the resonant pathways. (c) the experimental results.

ω_{rep} . We therefore expect that a short scan of the repetition frequency will result in a series of peaks, each of them representing the resonance of a different velocity class and with a different pair of counterpropagating photons. The difference in repetition frequency between two peak can be calculated by solving the resonance condition in Eq. 6.6, and reads [122]:

$$\Delta\omega_r \approx \left(\frac{n_1 - n_2}{n_1 n_2} \right) \frac{\omega_r}{2}. \quad (6.7)$$

A numerical simulation of the excitation profile due to the resonant pathways is given in Fig. 6.1b. For this simulation we have used the same parameters as the ones used in the previous section. The position of the peaks were found by solving the resonance condition in Eq. 6.6 and the width of each peak was set to correspond with the natural linewidth of the intermediate level

(theoretically the linewidth depends on the lifetime of both the intermediate (27 ns) and the final states (88 ns), however the lifetime of the intermediate state is much shorter and therefore will dominate). Finally, the strength of each peak represents the fraction of atoms in the specific velocity class.

We note that in both the resonant and nonresonant cases the y -axis was arbitrarily chosen. In the figure we set them both to the same height but this was just for visualization purposes. Therefore, our analysis does not provide information about which pathway will be dominant in a real measurement.

Experimental results

To test the analysis presented above we performed measurements of the $5S \rightarrow 5P \rightarrow 7S$ transition in rubidium vapour. The spectrum of the frequency comb was limited to two regions around 795 nm and 728 nm in order to avoid the excitation of other transitions. We performed a scan of the comb repetition frequency over a range of 50 Hz, while f_{CEO} was kept constant at 10 MHz. The result of this measurement is shown in Fig 6.1c. Both the overall structure and the position of the individual peaks correspond very well to the numerical simulation.

One of the primary goals of this measurement was to experimentally determine the relative contribution to the excitation between the resonant and nonresonant pathway. At first sight the experimental result seems to indicate that the ratio is approximately 1:1. However, this can be misleading. Due to the overlap between neighbouring peaks it is unclear whether the broad resonance is a result of the nonresonant pathways or the overlap between peaks. For example, in the simulation shown in Fig. 6.1b, if we increase the width of the peaks by 10% then the simulated signal would look very much like the experimental results, which means that the contribution of the resonant pathway would be dominant. In order to get an unambiguous result the measurement should be repeated with a higher repetition frequency (to increase the separation between the peaks). However, this required an extensive change to our setup which was unrealistic within the time frame of this project. A future measurement with an adapted setup should easily show which pathway dominates the signal. Nevertheless, even if not perfect, it is clear that changing the repetition frequency around the central peak is a good control parameter to change the ratio between resonant and nonresonant contributions to the total excitation.

6.4 Part 2: Spatial properties of the excitation pattern

In the first part of this chapter we have looked into the spectral properties of the excitation using a position-independent detector, therefore integrating the signal over the whole interaction region. Now we are going to look at the spatial

properties of the excitation by imaging the excitation pattern onto a camera. To model the expected spatial excitation pattern of the resonant two-photon transition we use the insight gained in chapter 3, where we have investigated the signal produced by two time-delayed pulses. We have shown that a scan of the time delay between the pulses is equivalent to a single shot of the spatial excitation in the counterpropagating geometry. Therefore we can use Eq. 3.8 to simulate the spatial excitation pattern by substituting the temporal parameter T with z/c , where c is the velocity of light. This equation represents the 4 combinations of photon pairs that add up to the transition frequency. There are, however, some modifications we need to apply to this equation. The reason is that it applies to a single pair of counterpropagating pulses and therefore does not take into account the mode structure of the frequency comb, nor the behaviour of the excitation due to the Doppler effect. The first modification is to ignore the terms that represent two photons coming from the same pulse, as they are not Doppler-reduced and result only in a constant background that is independent of the comb parameters. The second modification concerns the fact that this equation is derived for a single pair of counterpropagating pulses and therefore does not take into account the mode structure of the frequency comb. In order to incorporate the control parameter of the ratio between the resonant and nonresonant pathways we multiply the resonant contribution by a global scaling factor β , which allows us change the ratio between the various pathways. This is in line with the result of the previous section. The equation for the expected spatial excitation pattern can now be written as:

$$\begin{aligned}
 |a_f|^2(z) &\propto |a_1 + a_2|^2, \\
 a_1 &= i\pi A(\omega_i)A(\omega_0 - \omega_i) \cos((\omega_t/2 - \omega_i)z/c) e^{i2\tau|\frac{\omega_t}{2} - \omega_i|}, \\
 a_2 &= \beta \int \frac{d\omega}{\omega_i - \omega} A(\omega)A(\omega_t - \omega) \cos((\omega_t/2 - \omega)z/c) e^{i2\tau|\frac{\omega_t}{2} - \omega|}.
 \end{aligned} \tag{6.8}$$

We note that the modifications we made to this equations are phenomenological. The results shown in the remainder of this section will show whether these modifications are justified.

For the following measurement the comb parameters were set such that the central peak within the Doppler-broadened envelope in Fig. 6.1 is excited. This means that both resonant and nonresonant pathways are equally excited and we can set $\beta = 1$. Figure 6.2(a,b,c) shows 3 camera images of the excitation patterns that were recorded using a V-shaped spectral phase mask with $\tau = -600, 0, 600$ fs. From these images we have extracted a horizontal lineout and plotted the results in Fig. 6.2d. These results are compared to numerical simulation based on Eq. 6.8, which are shown in Fig. 6.2(e). The numerical simulation takes into account that the signal decreases due to the reduced intensity for positions away from the focus of the laser beams. We see that in

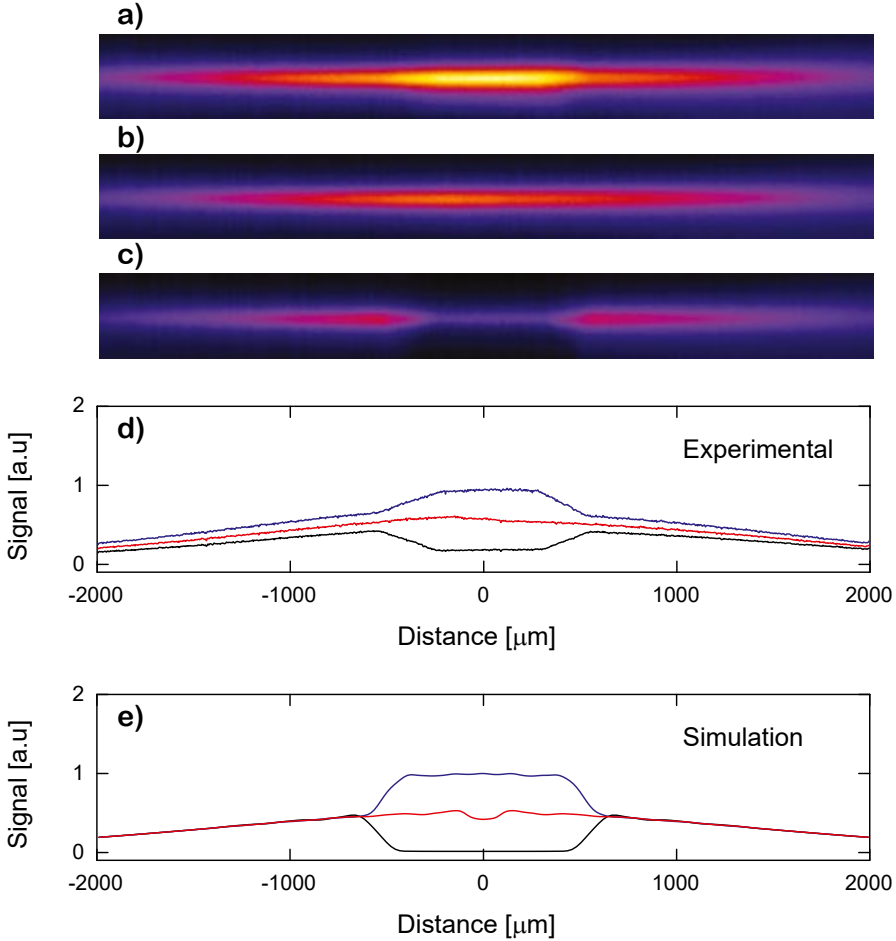


Figure 6.2: Spatial excitation patterns in stepwise two-photon transitions. The 3 images were taken with the parameters $\tau=665$ fs (a), $\tau=0$ fs (b), $\tau=-665$ fs (c). For each image a horizontal lineout is taken from the center of the image and is plotted in (d), which also gives the scale of the images. (e) The experimental data is compared to a numerical simulation based on Eq. 6.8. For this simulation we took into consideration the focusing condition and the spatial resolution of the EMCCD camera.

the case of transform-limited pulses the excitation profile is flat. This is a somewhat counterintuitive result as one might expect an enhancement of the signal at the region where the pulses overlap. However, due to the quantum interference between resonant and nonresonant pathways the effect of pulse overlap does not necessarily play a role in the overall excitation (this property was already identified in Chapter 3). When a V-shaped spectral phase mask is applied we see that only the central region is affected. Furthermore, the sign of the phase mask will either significantly increase or will strongly reduce the signal in that region. The width of this region depends on the slope of the phase mask, which determines the time delay between the red and blue subpulses. The only visual difference between the experimental results and the numerical simulation appears for the positive V-shaped phase, where the signal in the centre is increased. The numerical simulation displays a strong oscillation whereas in the measurement no oscillations are observed. This discrepancy is attributed to the spatial resolution of the EMCCD camera which is incapable of imaging features on the micrometer scale. Otherwise the agreement between measurement and simulation is excellent.

The next step is to see in what way does the spatial excitation pattern changes when the comb parameters are set such that the resonant pathway is not excited. We therefore tuned the comb parameters to be exactly in between two resonant peaks and repeated the steps mentioned in the previous paragraph. The results were, to within the accuracy obtained by our setup, identical to the previous measurement. This is unexpected, as the decreasing contribution of the resonant pathway is expected to change the spatial pattern. To gain a better understanding of these results we performed numerical simulations using Eq. 6.8 with different values of β . Figure 6.3 shows the result of this numerical simulation for a negative V-phase and with β set to 100%, 50% and 0%. This result clearly shows that a reduction of 50% lowers the contrast of the signal but does not alter the general shape of the spatial pattern (we note again that the fast oscillations are not visible experimentally due to the spatial resolution of the imaging system). Only when the resonant contribution approaches 0% we see a real change in the shape of the spatial pattern, which becomes a constant pattern. This result is a strong indication that the resonant peaks in Fig. 6.1 have a significant overlap, and we are thus unable to completely tune down the resonant pathway.

6.5 Part 3: Spectral properties at different spatial locations

In the last set of measurements we combine the spectral and spatial properties of the excitation to investigate the competition between resonant and

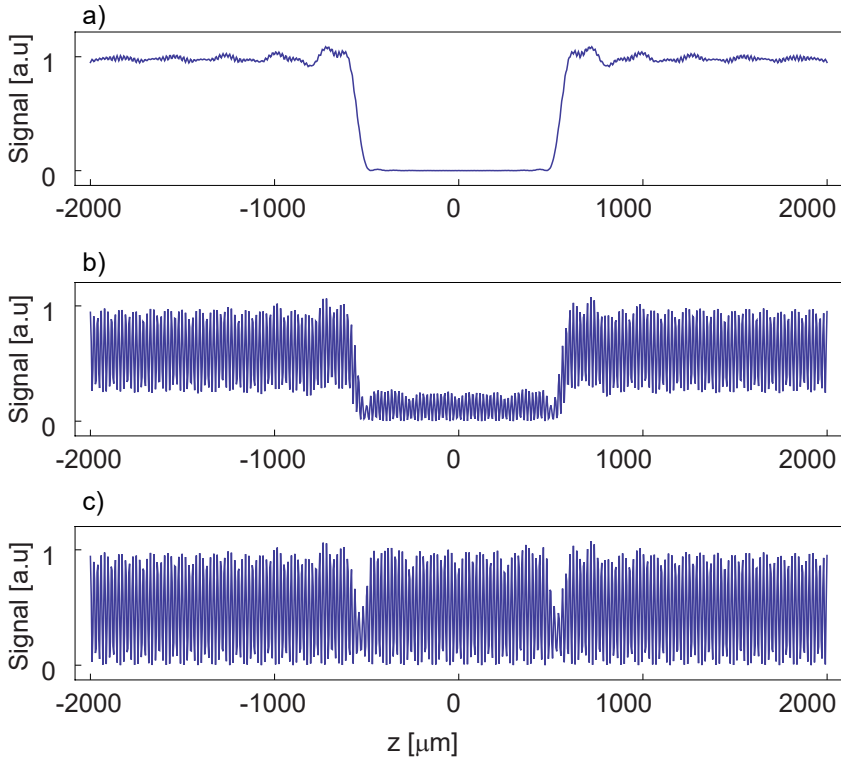


Figure 6.3: A simulation of the expected spatial excitation pattern for a negative V-shaped spectral phase mask. The simulation is based on Eq. 6.8 and shows the change in signal when the contribution of the resonant pathway is decreased. The scaling factor β is equal to: a) 1, b) 0.5, c) 0.01.

nonresonant pathways at different locations along the overlap region of the counterpropagating beams. For this measurement we recorded images of the spatial excitation pattern (using the EMCCD camera) while scanning the repetition frequency of the laser. We then integrate the signal over a small region of the excitation patterns and plot the result as a function of the repetition frequency. We performed this measurement for both positive and negative V-phase, as shown in Fig. 6.4. The camera image at the top of each graph is to indicate the shape of the spectral phase mask (positive or negative) and to show which parts of the image were integrated.

In the previous section we have seen that a V-shaped phase mask only changes the shape of the excitation pattern in the centre of the excitation pattern. We therefore begin by looking at the integrated signal in a region away from the centre. From the green trace in Fig. 6.4 we indeed see that the ratio between the height of the resonant peaks and the broad nonresonant peak is the same. Within the measurement accuracy this ratio is found to be 2.5 for both images. However, when looking at the signal at the centre of the images there is a clear difference between a positive and a negative V-shaped phase mask. For a negative phase mask (upper panel) we see that the height of the resonant peaks stays the same while the broad nonresonant peak is completely eliminated. In fact, the signal is even lower than expected. It is not clear whether this is a measurement error or an artefact. In any case, it is clear that for a negative V-shaped phase the contribution of the resonant pathways is dominant. For a positive phase mask (lower panel) we see a strong enhancement of the signal. The red trace in Fig. 6.4b shows that the contrast of the resonant peaks becomes smaller when compared to the broad nonresonant peak. This is a strong indication that the contribution of the nonresonant pathways becomes dominant when a positive V-shaped phase mask is applied.

6.6 Conclusion

In this chapter we have investigated the interplay between resonant and non-resonant pathways in two-photon transitions when driving the transition with counterpropagating frequency comb pulses. We found that these different pathways present a different behaviour when subjected to Doppler reduction due to the counterpropagating geometry. This can be used as a control parameter to reduce the contribution of the resonant pathway, therefore controlling the ratio between the two pathways. However, due to the choice of repetition frequency in our experiment the resonant peaks were not completely separated and we could not set the comb parameters to completely eliminate the resonant pathway. This is more of a technical consideration than a fundamental limitation and could be overcome using a laser system that operates at a higher repeti-

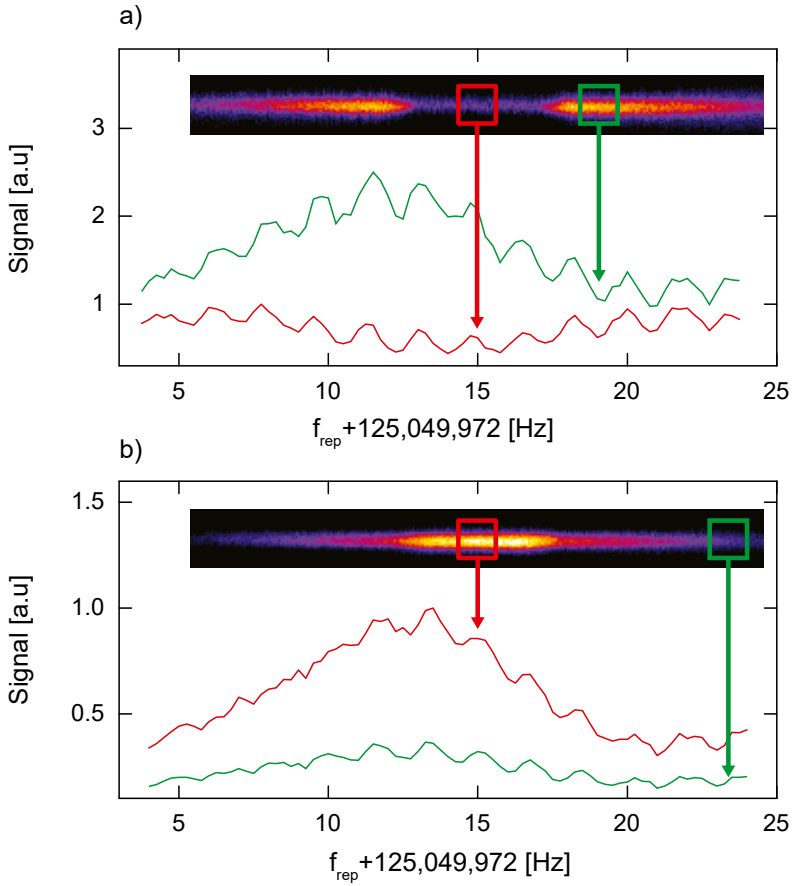


Figure 6.4: Spectral properties of the two-photon excitation in specific locations of the excitation pattern. For each value of the repetition frequency an image of the excitation pattern is recorded and the signal is integrated over a small region, either at the centre or at the edge of the image. The result is shown for (a) a negative V-shaped phase with $\tau = -667$ fs and (b) for a positive V-shaped phase with $\tau = +667$ fs.

tion frequency. For the transition used in our work we recommend a repetition frequency of about 250 MHz, which will ensure a complete separation between the resonant peaks.

We have also investigated the shape of the excitation pattern when applying a V-shaped phase mask. Due to the limitation described in the previous paragraph we were unable to measure a difference in the excitation pattern when changing the ratio between the resonant and the nonresonant pathways. We believe that the behaviour predicted by our model is correct and by conducting the experiment at a higher repetition frequency will show that when the resonant pathways are completely eliminated, the spatial pattern becomes flat, as our simulation illustrates in Fig. 6.3c.

Periodic Spectral Phase Modulation: an Alternative Parametrisation for Coherent Control Experiments

In this chapter we present a method for the generation of complex pulse sequences by using periodic spectral phase modulation. An analytical expression is derived for the temporal profile of such pulse sequences, which relates the temporal amplitudes and phases of the subpulses to the Fourier components of the periodic phase mask. We consider two families of periodic phase masks, namely, when a single period is an odd or even function, and discuss the differences between the resulting pulse sequences. The generalisation of the single sinusoidal phase mask adds more degrees of freedom to many existing coherent control experiments. This method can also be used as an alternative parametrisation for investigating quantum coherent control landscapes, which is illustrated for the process of nonresonant two-photon absorption.

7.1 Introduction

The generation and manipulation of ultrashort (femtosecond) laser pulses has opened new possibilities in studying and controlling light-matter interaction. Such pulses provide excellent temporal resolution that enables the investigation of the dynamics of molecular processes with high temporal resolution [123]. Simultaneously, due to the Fourier relation, such pulses exhibit a broad spectral coverage. This enables the simultaneous excitation of a quantum system via different pathways. In the field of coherent quantum control [30, 124, 25] shaping of femtosecond pulses is employed to steer a system to a desired final state by means of constructive and destructive quantum interferences between pathways leading to the same final state. Pulse shaping techniques are mainly based on a frequency domain manipulation using a spatial light modulator placed in the Fourier plane of a zero dispersion 4f grating-based configuration [73]. This provides programmable spectral phase masks [125] that change the temporal properties of the pulse without affecting the total energy. Similar schemes also allow shaping of the amplitude and polarization of the driving field [79, 80].

An important step in designing any coherent control experiment is to determine the appropriate control parameters [126]. Searching through all possible spectral masks is not only experimentally impractical but also difficult to interpret physically. Parametrisation of the spectral mask according to a physically relevant function basis can reduce the number of dimensions of the experimental search and assist in understanding the underlying control mechanism. Even though the manipulation is conducted in the frequency domain, understanding the temporal waveform provides valuable information about the dynamics of the system [127]. For example, allowing a single parameter to control the chirp rate (quadratic phase) has been shown to either strongly enhance or completely eliminate the two-photon absorption (TPA) signal. This behaviour was explained by the dependence of the time-dependent instantaneous frequency of chirped pulses [93, 40]. More control parameters allow investigation of control landscapes with more general properties of the control mechanisms. Many of the experimental realizations of control landscapes were demonstrated with parametrisation of chirp orders [94, 128, 129].

An alternative parametrisation is a sinusoidal spectral phase of the form $\varphi(\omega) = A \sin[\omega T + \phi]$, where the control parameters A , T and ϕ determine the modulation amplitude, period and phase, respectively. It has been previously shown [130] that such a spectral phase mask results in a sequence of equally spaced subpulses, where the shape of the envelope of each subpulse is the same as the unmodulated pulse. This parametrisation was employed to various systems from controlling biological systems [78], selective excitation of molecular vibrational levels [131] to the spatial control of atomic excitation [108].

In this paper we generalize the concept of a single sinusoidal spectral phase modulation to arbitrary periodic phase masks. We derive an analytical expression for the temporal amplitude and phase profiles of the resulting pulse sequences. The derivation is based on the Fourier expansion of periodic functions where a single period is an even or an odd function. These two families of phase masks present unique properties compared to the case of a single sinusoidal phase mask. These properties can be exploited for enhanced controllability and provide an alternative parametrisation for investigating control landscapes.

7.2 Sinusoidal spectral phase

For sake of comparison we briefly summarize the properties of a pulse sequence when applying a single sinusoidal phase mask (for a detailed derivation see Ref. [41]). In the time domain this corresponds to a sequence of subpulses separated by time T . The temporal amplitude of the n^{th} subpulse is $|J_n(A)|$, where $J_n(A)$ is the Bessel function of the first kind of order n . The temporal phase displays different patterns for even and odd phase masks, where the symmetry is defined with respect to the pulse carrier frequency ω_0 . This symmetry plays an important role in coherent control experiments as pulse sequences with the same amplitude profiles but different temporal phase patterns can lead to strikingly different outcomes [38, 108].

7.3 Periodic spectral phase with even functions

In ultrafast optics [132] the (positive frequency) electric field of a short pulse with carrier frequency ω_0 is written as $E_{in}^+(t) = \mathcal{E}_{in}^+(t)e^{i\omega_0 t}$. The envelope function $\mathcal{E}_{in}^+(t)$ encompasses both the amplitude and the nonlinear phase of the pulse and is generally a complex function. The generation of pulse sequences occurs when a periodic spectral phase mask of the form

$$\varphi(\omega) = \sum_{k=1}^r a_k \cos[kT(\omega - \omega_{ref})], \quad (7.1)$$

with periodicity $\frac{2\pi}{T}$, is applied to a spectrum $E_{in}^+(\omega)$ (initially assumed to be Fourier-limited). The output field can be written as:

$$\begin{aligned} E_{out}(\omega) &= E_{in}^+(\omega) e^{i \sum_{k=1}^r a_k \cos[kT(\omega - \omega_{ref})]} \\ &= E_{in}^+(\omega) \prod_{k=1}^r e^{i a_k \cos[kT(\omega - \omega_{ref})]}, \end{aligned} \quad (7.2)$$

7. PERIODIC SPECTRAL PHASE MODULATION: AN ALTERNATIVE PARAMETRISATION FOR COHERENT CONTROL EXPERIMENTS

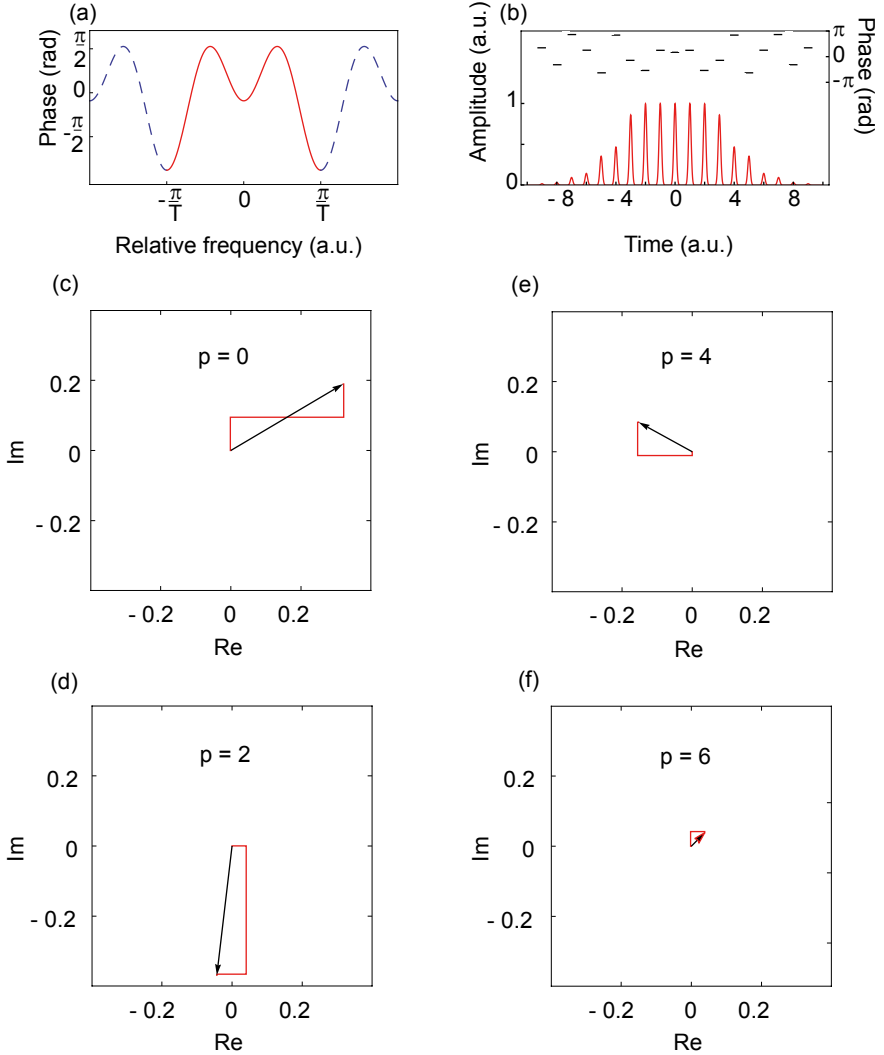


Figure 7.1: Generation of pulse sequences by a periodic phase-only mask where a single period is an even function. (a) A periodic spectral phase mask as defined in Eq. 7.1 with $a = \{1.24, -1.53\}$ and $\Delta\omega = 0$. (b) The amplitude and phase patterns generated by this phase mask. (c),(d),(e),(f) Vector representation of the total pulse amplitude and phase (black arrows) of the 0th, 2nd, 4th and 6th subpulses, respectively. The red lines represent all the contributions, as defined in Eq. 7.7, to each subpulse.

where ω_{ref} determines the origin of the phase modulation. In order to find an expression for the temporal waveform we need to perform a Fourier transformation of Eq. 7.2. Before this can be done the expression needs to be simplified. The first step is to use the Jacobi-Anger relation

$$e^{iA \cos(\theta)} = \sum_{n=-\infty}^{\infty} i^n J_n(A) e^{in\theta}. \quad (7.3)$$

Inserting Eq. 7.3 into Eq. 7.2 leads to:

$$E_{out}^+(\omega) = E_{in}^+(\omega) \prod_{k=1}^r \left[\sum_{n=-\infty}^{\infty} i^n J_n(a_k) e^{inkT(\omega - \omega_{ref})} \right]. \quad (7.4)$$

As a second step we rearrange the terms by writing the product of sums as a sum of products, resulting in

$$E_{out}^+(\omega) = \sum_{n_1, \dots, n_r = -\infty}^{\infty} \left[\prod_{k=1}^r i^{n_k} J_{n_k}(a_k) \right] \times e^{iT(\omega - \omega_{ref}) \sum_{k=1}^r n_k k} E_{in}^+(\omega). \quad (7.5)$$

Grouping these terms together allows us to apply the Fourier transformation to each term individually. The temporal profile of the shaped pulse now reads

$$E_{out}^+(t) = e^{i\omega_0 t} \sum_{n_1, \dots, n_r = -\infty}^{\infty} \left(\prod_{k=1}^r i^{n_k} J_{n_k}(a_k) \right) \times \left(e^{i\Delta\omega T \sum n_k k} \right) \times \mathcal{E}_{in}^+(t + T \sum n_k k), \quad (7.6)$$

where $\Delta\omega = \omega_0 - \omega_{ref}$ is the frequency detuning between the periodic phase mask and the laser carrier frequency. Each term in Eq. 7.6 corresponds to a set of the indices $\{n_1, \dots, n_r\}$, and represents a time-delayed scaled replica of the original pulse. It is characterized by the complex envelope function

$$\mathcal{E}_{out}^+(t, n_1, \dots, n_r) = \left(\prod_{k=1}^r i^{n_k} J_{n_k}(a_k) \right) \times \left(e^{i\Delta\omega T \sum n_k k} \right) \times \mathcal{E}_{in}^+(t + T \sum n_k k), \quad (7.7)$$

7. PERIODIC SPECTRAL PHASE MODULATION: AN ALTERNATIVE PARAMETRISATION FOR COHERENT CONTROL EXPERIMENTS

which defines the amplitude and phase for each subpulse. Provided that T is larger than the pulse duration of the unmodulated pulse, Eq. 7.6 represents a sequence of well separated subpulses where the p^{th} subpulse is computed by summing over all terms for which

$$\sum n_k k = p. \quad (7.8)$$

An example of a periodic spectral phase mask with two amplitude parameters $a_k = \{1.24, -1.53\}$ and $\Delta\omega = 0$ is shown in Fig. 7.1a. The corresponding pulse sequence, as given by Eq. 7.6, is plotted in Fig. 7.1b where the summation over the indices n_k is truncated to include only the terms where $-10 < n_k < 10$. A vector representation of the individual terms leading to the same subpulse are shown in Fig. 7.1(c-f) for a number of selected subpulses. As clearly shown in the figure, only a small number of terms actually contributes significantly to the total amplitude. The amplitude pattern of the pulse sequence in Fig. 7.1b is symmetric with respect to $t=0$. This is a general property of pulse sequences generated by a periodic phase mask where a single period is an even function. To understand this we note that Eq. 7.6 consists of pairs of terms with $\{n_k\}$ and $\{n'_k\} = (-1) \cdot \{n_k\}$ contributing to the p^{th} and $-p^{\text{th}}$ subpulse, respectively. The amplitudes of these two terms are equal due to the relation $J_{-n}(x) = (-1)^n J_n(x)$. The same argument holds for the temporal phase pattern, provided that $\Delta\omega = 0$. As can be seen from Eq. 7.7 a nonzero $\Delta\omega$ adds a phase to each subpulse that is linear with respect to the pulse number p . While varying $\Delta\omega$ the vectors in Figs. 7.1(c-f) rotate, leaving the amplitude of the subpulses unchanged. Naturally, after $\Delta\omega$ is changed by a full period the original phase pattern is recovered.

7.4 Periodic spectral phase with odd functions

So far we considered periodic phase masks where a single period is an even function. We now turn to the case where the periodic phase mask is composed of odd functions

$$\varphi(\omega) = \sum_{k=1}^r a_k \sin [kT(\omega - \omega_{ref})]. \quad (7.9)$$

The derivation of the time domain waveform resulting from this spectral phase mask is similar to the one presented above, with one distinct difference. The Jacobi-Anger relation for odd sinusoidal functions is

$$e^{iA \sin(\theta)} = \sum_{n=-\infty}^{\infty} J_n(A) e^{in\theta}. \quad (7.10)$$

Following the same steps as in Eq. 7.4 and Eq. 7.5 we find the time domain electric field to be

$$\begin{aligned}
 E_{out}^+(t) = e^{i\omega_0 t} & \sum_{n_1 \dots n_r = -\infty}^{\infty} \left(\prod_{k=1}^r J_{n_k}(a_k) \right) \\
 & \times \left(e^{-i\Delta\omega T \sum n_k k} \right) \\
 & \times \mathcal{E}_{in}^+(t + T \sum n_k k).
 \end{aligned} \tag{7.11}$$

As in the previous case, this leads to a sequence of subpulses where each subpulse is computed by summing over all complex envelope contributions

$$\begin{aligned}
 \mathcal{E}_{out}^+(t, n_1, \dots, n_r) = & \left(\prod_{k=1}^r J_{n_k}(a_k) \right) \\
 & \times \left(e^{i\Delta\omega T \sum n_k k} \right) \\
 & \times \mathcal{E}_{in}^+(t + T \sum n_k k).
 \end{aligned} \tag{7.12}$$

for which $\sum n_k k = p$.

Equations 7.6 and 7.11 are almost identical. However, the pulse sequences generated by odd and even base functions exhibit markedly different properties. Most notable, the absence of the i^{n_k} in Eq. 7.12 means that the amplitudes of the p^{th} and $-p^{th}$ subpulses are no longer necessarily equal. The possibility to generate asymmetric pulse sequences is illustrated in Fig. 7.2 for the Fourier coefficients $a_k = \{1.4, 0.4\}$ and $\Delta\omega = 0$. In this example a linear increase in amplitude between consecutive subpulses is clearly visible, but other sequences are possible by optimizing the values of the Fourier coefficients for a specific goal. An additional difference from the case of an even phase mask is that the complex envelope is a real function with temporal phase being only 0 or π . A nonzero $\Delta\omega$ has the same influence as explained above.

7.5 Coherent control with periodic functions - Nonresonant TPA

Parametrisation of the spectral phase into a base of physically relevant functions has been employed for the investigation of the general properties of control landscapes [133, 134]. In order to illustrate how periodic spectral phase masks provide a viable parametrisation for coherent control experiments we consider the process of nonresonant TPA. In this scheme a two-photon transition is excited by pairs of frequencies where no intermediate one-photon resonances lie

7. PERIODIC SPECTRAL PHASE MODULATION: AN ALTERNATIVE PARAMETRISATION FOR COHERENT CONTROL EXPERIMENTS

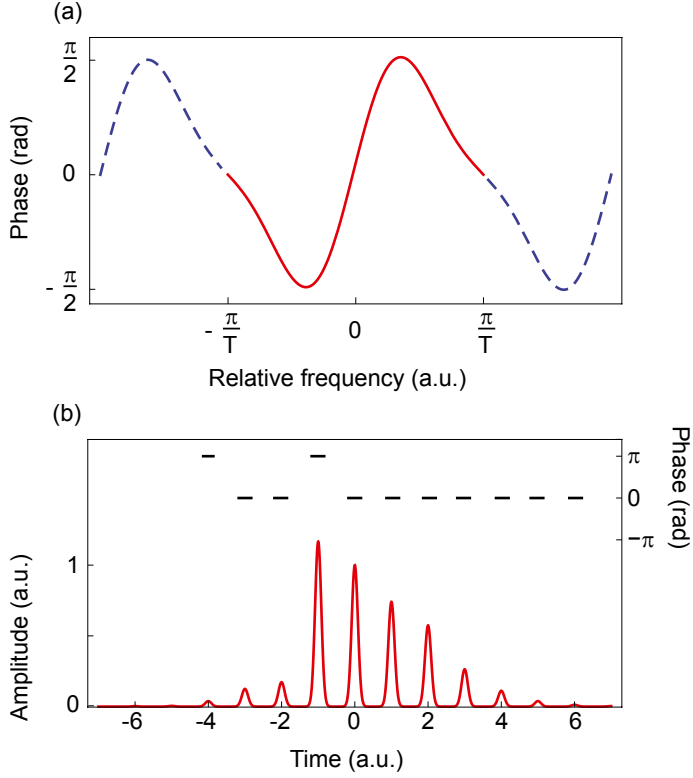


Figure 7.2: Generation of asymmetric pulse sequences with an odd spectral phase mask. (a) A spectral phase mask as defined in Eq. 7.9, with $a = \{1.4, 0.4\}$ and $\Delta\omega = 0$. (b) The resulting temporal amplitude and phase patterns.

within the laser bandwidth. In the weak-field regime, the transition probability is proportional to the integral

$$S = \left| \int d\omega A\left(\frac{\omega_t}{2} + \omega\right) A\left(\frac{\omega_t}{2} - \omega\right) \times e^{[i(\varphi(\frac{\omega_t}{2} + \omega) + \varphi(\frac{\omega_t}{2} - \omega))]} \right|^2, \quad (7.13)$$

where $A(\omega)$ and $\varphi(\omega)$ are the spectral amplitude and phase of the driving field and ω_t is the two-photon transition frequency. Meshulach *et al* [38] have shown that the two-photon transition rate can be completely suppressed by a specific choice of pulse sequences. These so-called "dark pulses" are acquired

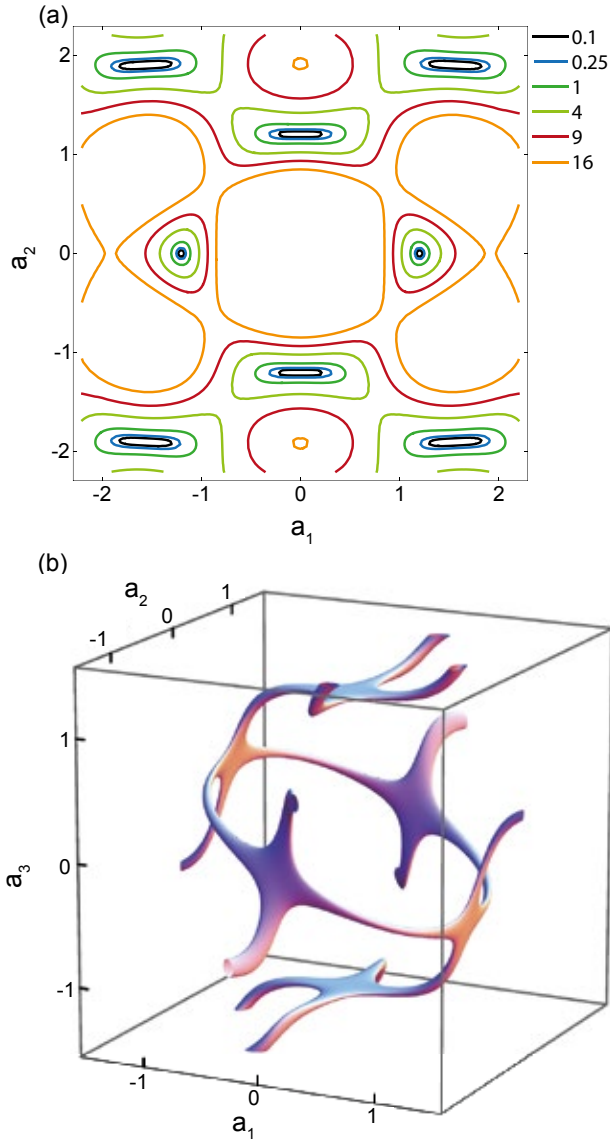


Figure 7.3: Control landscape of nonresonant TPA. (a) Various level sets in a two-dimensional plot. The control parameters are the first two Fourier coefficients of the periodic spectral phase mask. The values indicated in the legend represent a percentage of the signal level acquired with transform-limited pulses. (b) A 3D contour plot of 0.1% excitation level shows that all dark pulses are connected, displaying a unique topology of the control landscape.⁹⁵

7. PERIODIC SPECTRAL PHASE MODULATION: AN ALTERNATIVE PARAMETRISATION FOR COHERENT CONTROL EXPERIMENTS

by a sinusoidal phase when the modulation amplitude A satisfies $J_0(2A) = 0$ and the phase mask is an even function with respect to half of the transition frequency (odd phase masks do not influence the transition probability [38]). The calculation of a multi-dimensional control landscape of this process can be achieved by inserting Eq. 7.1 into Eq. 7.13 and computing the integral for each point of the parameter space. This is however a difficult computational task even for a powerful computer. Alternatively, we can use our previous derivation to considerably simplify the expression for the transition probability. Using the same steps as in Eq. 7.4 and 7.5 we find that the transition probability can be written as

$$S = \left| \sum_{n_1, \dots, n_r = -\infty}^{\infty} \prod_{k=1}^r (i^{n_k} J_{n_k}(2a_k)) \times \int d\omega A\left(\frac{\omega_t}{2} + \omega\right) A\left(\frac{\omega_t}{2} - \omega\right) e^{-iT\omega \sum_k n_k k} \right|^2. \quad (7.14)$$

From this equation we can identify that for each set of parameters $\{n_1, n_2, \dots, n_r\}$ the factor in front of the integral is the same as the amplitude of a specific subpulse in Eq. 7.7, albeit with a doubled modulation amplitude. Furthermore, the exponent in the integral contains an expression identical to the definition of the pulse number p in Eq. 7.8. In the case of well separated subpulses the integrand in Eq. 7.14 oscillates rapidly, leading to negligible contribution to the excitation. Therefore, only terms for which $\sum n_k k = 0$ are nonzero which means that the transition probability depends solely on the intensity of the central subpulse. This surprising property reduces the calculation of the transition probability to computing the temporal amplitude of the central subpulse, leading to a dramatic decrease in required computational power.

We use this method to visualize the control landscape of nonresonant TPA. Figure 7.3a displays a two-dimensional contour plot where the two control parameters are the first two coefficients of the Fourier series in Eq. 7.1. Each contour represents a collection of pulse shapes that lead to the same yield and is termed a "level set" [128]. This control landscape exhibits multiple distinct solutions for zero excitation (dark pulses). Interestingly, the situation changes dramatically when allowing for an additional control parameter as seen in Fig. 7.3b. This figure shows that all dark pulse solutions are connected in a nontrivial way. In the present case the level sets are open surfaces exhibiting a markedly different topology than previous work on control landscapes where level sets were shown to form closed surfaces [128, 135]. This comparison verifies that the topology of the control landscape strongly depends on the applied parametrisation and also demonstrates that our method can be used as a valuable alternative for existing studies of control landscapes.

7.6 Conclusion

In conclusion we have introduced a new class of spectral phase masks for coherent control experiments, namely, arbitrary periodic phase functions. An analytical derivation of the temporal waveform is presented, that relates the Fourier coefficients of the periodic spectral phase to the temporal amplitudes and phases of the resulting subpulses. These pulse sequences exhibit new characteristics that are unattainable with a single sinusoidal spectral phase mask, such as nearly equal intensities of the subpulses and asymmetric pulse sequences. Our method is shown to simplify the calculation of nonresonant TPA and enables fast computation of multidimensional control landscapes. The added degrees of freedom provided by our method can benefit existing coherent control experiments that have used a single sinusoidal phase mask, and can also be used as an alternative parametrisation for investigating control landscapes.

Bibliography

- [1] T. H. Maiman, “Stimulated optical radiation in ruby,” *Nature*, vol. 187, p. 493, 1960.
- [2] A. Javan, W. R. Bennett, and D. R. Herriott, “Population inversion and continuous optical maser oscillation in a gas discharge containing a He-Ne mixture,” *Physical Review Letters*, vol. 6, p. 106, 1961.
- [3] T. Hänsch, I. Shahin, and A. Schawlow, “High-resolution saturation spectroscopy of the sodium d lines with a pulsed tunable dye laser,” *Physical Review Letters*, vol. 27, p. 707, 1971.
- [4] T. Hänsch, K. Harvey, G. Meisel, and A. Schawlow, “Two-photon spectroscopy of Na 3s-4d without Doppler broadening using a cw dye laser,” *Optics Communications*, vol. 11, p. 50, 1974.
- [5] J. Bjorkholm and P. Liao, “Resonant enhancement of two-photon absorption in sodium vapor,” *Physical Review Letters*, vol. 33, p. 128, 1974.
- [6] M. Salour and C. Cohen-Tannoudji, “Observation of Ramsey’s Interference Fringes in the Profile of Doppler-Free Two-Photon Resonances,” *Physical Review Letters*, vol. 38, p. 757, 1977.
- [7] M. Snadden, A. Bell, E. Riis, and A. Ferguson, “Two-photon spectroscopy of laser-cooled Rb using a mode-locked laser,” *Optics communications*, vol. 125, p. 70, 1996.
- [8] R. van Rooij, J. S. Borbely, J. Simonet, M. D. Hoogerland, K. S. E. Eikema, R. A. Rozendaal, and W. Vassen, “Frequency Metrology in Quantum Degenerate Helium: Direct Measurement of the $2^3S_1 \rightarrow 2^1S_0$ Transition,” *Science*, vol. 333, p. 196, 2011.
- [9] R. P. M. J. W. Notermans and W. Vassen, “High-precision spectroscopy of the forbidden $2^3S_1 \rightarrow 2^1P_1$ transition in quantum degenerate metastable helium,” *Physical Review Letters*, vol. 112, p. 253002, 2014.
- [10] M. Weitz, A. Huber, F. Schmidt-Kaler, D. Leibfried, W. Vassen, C. Zimmermann, K. Pachucki, T. W. Hansch, L. Julien, and F. Biraben,

- “Precision-Measurement of the 1s Ground-State Lamb Shift in Atomic-Hydrogen and Deuterium by Frequency Comparison,” *Physical Review A*, vol. 52, p. 2664, 1995.
- [11] C. G. Parthey, A. Matveev, J. Alnis, B. Bernhardt, A. Beyer, R. Holzwarth, A. Maistrou, R. Pohl, K. Predehl, T. Udem, T. Wilken, N. Kolachevsky, M. Abgrall, D. Rovera, C. Salomon, P. Laurent, and T. W. Hänsch, “Improved Measurement of the Hydrogen $1S \rightarrow 2S$ Transition Frequency,” *Physical Review Letters*, vol. 107, p. 203001, 2011.
- [12] K. S. E. Eikema, W. Ubachs, W. Vassen, and W. Hogervorst, “Lamb shift measurement in the $1t^1S$ ground state of helium,” *Physical Review A*, vol. 55, p. 1866, 1997.
- [13] S. Bergeson, A. Balakrishnan, K. Baldwin, T. Lucatorto, J. Marangos, T. McIlrath, T. O’Brian, S. Rolston, C. Sansonetti, J. Wen, N. Westbrook, C. Cheng, and E. Eyler, “Measurement of the He Ground State Lamb Shift via the Two-Photon 1^1S - 2^1S Transition,” *Physical Review Letters*, vol. 80, p. 3475, 1998.
- [14] S. A. Diddams, T. Udem, J. C. Bergquist, E. A. Curtis, R. E. Drullinger, L. Hollberg, W. M. Itano, W. D. Lee, C. W. Oates, K. R. Vogel, and D. J. Wineland, “An optical clock based on a single trapped $^{199}\text{Hg}^+$ ion,” *Science*, vol. 293, p. 825, 2001.
- [15] C. W. Chou, D. B. Hume, J. C. J. Koelemeij, D. J. Wineland, and T. Rosenband, “Frequency comparison of two high-accuracy Al^+ optical clocks,” *Physical Review Letters*, vol. 104, p. 070802, 2010.
- [16] A. D. Ludlow, T. Zelevinsky, G. K. Campbell, S. Blatt, M. M. Boyd, M. H. G. de Miranda, M. J. Martin, J. W. Thomsen, S. M. Foreman, J. Ye, T. M. Fortier, J. E. Stalnaker, S. A. Diddams, Y. Le Coq, Z. W. Barber, N. Poli, N. D. Lemke, K. M. Beck, and C. W. Oates, “Sr lattice clock at 1×10^{-16} fractional uncertainty by remote optical evaluation with a Ca clock,” *Science*, vol. 319, p. 1805, 2008.
- [17] B. J. Bloom, T. L. Nicholson, J. R. Williams, S. L. Campbell, M. Bishof, X. Zhang, W. Zhang, S. L. Bromley, and J. Ye, “An optical lattice clock with accuracy and stability at the 10^{-18} level,” *Nature*, vol. 506, p. 71, 2014.
- [18] N. Huntemann, B. Lipphardt, C. Tamm, V. Gerginov, S. Weyers, and E. Peik, “Improved limit on a temporal variation of m_p/m_e from comparisons of Yb^+ and Cs atomic clocks,” *Physical Review Letters*, vol. 113, 2014.

-
- [19] R. M. Godun, P. B. R. Nisbet-Jones, J. M. Jones, S. A. King, L. A. M. Johnson, H. S. Margolis, K. Szymaniec, S. N. Lea, K. Bongs, and P. Gill, "Frequency ratio of two optical clock transitions in $^{171}\text{Yb}^+$ and constraints on the time variation of fundamental constants," *Physical Review Letters*, vol. 113, p. 210801, 2014.
- [20] A. Derevianko and M. Pospelov, "Hunting for topological dark matter with atomic clocks," *Nature Physics*, vol. 10, p. 933, 2014.
- [21] A. H. Zewail, "Laser selective chemistry - is it possible?," *Physics Today*, vol. 33, p. 27, 1980.
- [22] N. Bloembergen and A. H. Zewail, "Energy redistribution in isolated molecules and the questions of mode-selective laser chemistry revisited," *J. Phys. Chem.*, vol. 88, p. 5459, 1984.
- [23] A. H. Zewail, "Femtochemistry: Recent Progress in Studies of Dynamics and Control of Reactions and Their Transition States," *The Journal of Physical Chemistry*, vol. 100, p. 12701, 1996.
- [24] C. Brif, R. Chakrabarti, and H. Rabitz, "Control of quantum phenomena: past, present and future," *New Journal of Physics*, vol. 12, p. 075008, 2010.
- [25] W. S. Warren, H. Rabitz, and M. Dahleh, "Coherent Control of Quantum Dynamics : The Dream Is Alive," *Science*, vol. 259, p. 1581, 1993.
- [26] Y. Silberberg, "Quantum coherent control for nonlinear spectroscopy and microscopy," *Annual review of physical chemistry*, vol. 60, p. 277, 2009.
- [27] M. Wollenhaupt, V. Engel, and T. Baumert, "Femtosecond laser photoelectron spectroscopy on atoms and small molecules: prototype studies in quantum control.," *Annual review of physical chemistry*, vol. 56, p. 25, 2005.
- [28] P. Brumer and M. Shapiro, "Control of unimolecular reactions using coherent light," *Chemical Physics Letters*, vol. 126, p. 541, 1986.
- [29] M. Shapiro, J. W. Hepburn, and P. Brumer, "Simplified laser control of unimolecular reactions: Simultaneous (ω_1, ω_3) excitation," *Chemical Physics Letters*, vol. 149, p. 451, 1988.
- [30] D. J. Tannor and S. A. Rice, "Control of selectivity of chemical reaction via control of wave packet evolution," *The Journal of Chemical Physics*, vol. 83, p. 5013, 1985.

- [31] D. J. Tannor, R. Kosloff, and S. a. Rice, "Coherent pulse sequence induced control of selectivity of reactions: Exact quantum mechanical calculations," *The Journal of Chemical Physics*, vol. 85, p. 5805, 1986.
- [32] C. Chen, Y. Y. Yin, and D. S. Elliott, "Interference between optical transitions," *Physical Review Letters*, vol. 64, p. 507, 1990.
- [33] D. W. Schumacher, F. Weihe, H. G. Muller, and P. H. Bucksbaum, "Phase dependence of intense field ionization: A study using two colors," *Physical Review Letters*, vol. 73, p. 1344, 1994.
- [34] Y. Y. Yin, C. Chen, D. S. Elliott, and A. V. Smith, "Asymmetric photoelectron angular distributions from interfering photoionization processes," *Physical Review Letters*, vol. 69, p. 2353, 1992.
- [35] T. Baumert, M. Grosser, R. Thalweiser, and G. Gerber, "Femtosecond time-resolved molecular multiphoton ionization: The Na₂ system," *Physical Review Letters*, vol. 67, p. 3753, 1991.
- [36] A. Monmayrant, S. Weber, and B. Chatel, "A newcomer's guide to ultra-short pulse shaping and characterization," *Journal of Physics B: Atomic, Molecular and Optical Physics*, vol. 43, p. 103001, 2010.
- [37] A. M. Weiner, "Ultrafast optical pulse shaping: A tutorial review," *Optics Communications*, vol. 284, p. 3669, 2011.
- [38] D. Meshulach and Y. Silberberg, "Coherent quantum control of two-photon transitions by a femtosecond laser pulse," *Nature*, vol. 396, p. 239, 1998.
- [39] N. Dudovich, B. Dayan, S. Gallagher Faeder, and Y. Silberberg, "Transform-Limited Pulses Are Not Optimal for Resonant Multiphoton Transitions," *Physical Review Letters*, vol. 86, p. 47, 2001.
- [40] B. Chatel, J. Degert, S. Stock, and B. Girard, "Competition between sequential and direct paths in a two-photon transition," *Physical Review A*, vol. 68, p. 041402, 2003.
- [41] M. Wollenhaupt, A. Präkelt, C. Sarpe-Tudoran, D. Liese, T. Bayer, and T. Baumert, "Femtosecond strong-field quantum control with sinusoidally phase-modulated pulses," *Physical Review A*, vol. 73, p. 063409, 2006.
- [42] B. D. Bruner, H. Suchowski, N. V. Vitanov, and Y. Silberberg, "Strong-field spatiotemporal ultrafast coherent control in three-level atoms," *Physical Review A*, vol. 81, p. 063410, 2010.

-
- [43] M. Krug, T. Bayer, M. Wollenhaupt, C. Sarpe-Tudoran, T. Baumert, S. S. Ivanov, and N. V. Vitanov, "Coherent strong-field control of multiple states by a single chirped femtosecond laser pulse," *New Journal of Physics*, vol. 11, p. 105051, 2011.
- [44] C. Trallero-Herrero, D. Cardoza, T. Weinacht, and J. Cohen, "Coherent control of strong field multiphoton absorption in the presence of dynamic Stark shifts," *Physical Review A*, vol. 71, p. 013423, 2005.
- [45] S. Clow, C. Trallero-Herrero, T. Bergeman, and T. Weinacht, "Strong Field Multiphoton Inversion of a Three-Level System Using Shaped Ultrafast Laser Pulses," *Physical Review Letters*, vol. 100, p. 233603, 2008.
- [46] D. Oron, E. Tal, and Y. Silberberg, "Scanningless depth-resolved microscopy," *Optics express*, vol. 13, p. 1468, 2005.
- [47] E. Papagiakoumou, V. de Sars, V. Emiliani, and D. Oron, "Temporal focusing with spatially modulated excitation," *Optics express*, vol. 17, p. 5391, 2009.
- [48] H. Suchowski, D. Oron, and Y. Silberberg, "Generation of a dark nonlinear focus by spatio-temporal coherent control," *Optics Communications*, vol. 264, p. 482, 2006.
- [49] H. R. Telle, D. Meschede, and T. W. Hänsch, "Realization of a new concept for visible frequency division: phase locking of harmonic and sum frequencies.," *Optics letters*, vol. 15, p. 532, 1990.
- [50] T. Udem, A. Huber, B. Gross, J. Reichert, M. Prevedelli, M. Weitz, and T. W. Hänsch, "Phase-Coherent Measurement of the Hydrogen 1S-2S Transition Frequency with an Optical Frequency Interval Divider Chain," *Phys. Rev. Lett.*, vol. 79, p. 2646, 1997.
- [51] C. Schwob, L. Jozefowski, B. de Beauvoir, L. Hilico, F. Nez, L. Julien, F. Biraben, O. Acaf, J.-J. Zondy, and A. Clairon, "Optical Frequency Measurement of the 2s-12d Transitions in Hydrogen and Deuterium: Rydberg Constant and Lamb Shift Determinations," *Phys. Rev. Lett.*, vol. 82, p. 4960, 1999.
- [52] T. Udem, J. Reichert, R. Holzwarth, and T. Hänsch, "Absolute Optical Frequency Measurement of the Cesium D_1 Line with a Mode-Locked Laser," *Physical Review Letters*, vol. 82, p. 3568, 1999.
- [53] J. Reichert, R. Holzwarth, T. Udem, and T. W. Hänsch, "Measuring the frequency of light with mode-locked lasers," *Optics Communications*, vol. 172, p. 59, 1999.

- [54] S. Diddams, D. Jones, J. Ye, S. Cundiff, J. Hall, J. Ranka, R. Windeler, R. Holzwarth, T. Udem, and T. Hänsch, "Direct Link between Microwave and Optical Frequencies with a 300 THz Femtosecond Laser Comb," *Physical Review Letters*, vol. 84, p. 5102, 2000.
- [55] D. J. Jones, S. A. Diddams, J. K. Ranka, A. Stentz, R. S. Windeler, J. L. Hall, and S. T. Cundiff, "Carrier-Envelope Phase Control of Femtosecond Mode-Locked Lasers and Direct Optical Frequency Synthesis," *Science*, vol. 288, p. 635, 2000.
- [56] R. Holzwarth, T. Udem, T. Hänsch, J. Knight, W. Wadsworth, and P. Russell, "Optical Frequency Synthesizer for Precision Spectroscopy," *Physical Review Letters*, vol. 85, p. 2264, 2000.
- [57] F. Krausz, "Attosecond physics," *Reviews of Modern Physics*, vol. 81, p. 163, 2009.
- [58] A. Marian, M. C. Stowe, J. R. Lawall, D. Felinto, and J. Ye, "United time-frequency spectroscopy for dynamics and global structure.," *Science*, vol. 306, p. 2063, 2004.
- [59] A. Marian, M. C. Stowe, D. Felinto, and J. Ye, "Direct Frequency Comb Measurements of Absolute Optical Frequencies and Population Transfer Dynamics," *Physical Review Letters*, vol. 95, p. 023001, 2005.
- [60] V. Gerginov, C. E. Tanner, S. A. Diddams, A. Bartels, and L. Hollberg, "High-resolution spectroscopy with a femtosecond laser frequency comb," *Optics Letters*, vol. 30, p. 1734, 2005.
- [61] J. E. Stalnaker, V. Mbele, V. Gerginov, T. M. Fortier, S. A. Diddams, L. Hollberg, and C. E. Tanner, "Femtosecond frequency comb measurement of absolute frequencies and hyperfine coupling constants in cesium vapor," *Physical Review A*, vol. 81, p. 043840, 2010.
- [62] A. L. Wolf, S. A. van den Berg, W. Ubachs, and K. S. E. Eikema, "Direct Frequency Comb Spectroscopy of Trapped Ions," *Physical Review Letters*, vol. 102, p. 223901, 2009.
- [63] S. A. Diddams, L. Hollberg, and V. Mbele, "Molecular fingerprinting with the resolved modes of a femtosecond laser frequency comb.," *Nature*, vol. 445, p. 627, 2007.
- [64] S. Witte, R. T. Zinkstok, W. Ubachs, W. Hogervorst, and K. S. E. Eikema, "Deep-ultraviolet quantum interference metrology with ultrashort laser pulses.," *Science*, vol. 307, p. 400, 2005.

-
- [65] A. Cingöz, D. C. Yost, T. K. Allison, A. Ruehl, M. E. Fermann, I. Hartl, and J. Ye, “Direct frequency comb spectroscopy in the extreme ultraviolet,” *Nature*, vol. 482, p. 68, 2012.
- [66] M. Stowe, F. Cruz, A. Marian, and J. Ye, “High Resolution Atomic Coherent Control via Spectral Phase Manipulation of an Optical Frequency Comb,” *Physical Review Letters*, vol. 96, p. 153001, 2006.
- [67] M. Stowe, A. Pe’er, and J. Ye, “Control of Four-Level Quantum Coherence via Discrete Spectral Shaping of an Optical Frequency Comb,” *Physical Review Letters*, vol. 100, p. 203001, 2008.
- [68] S. Reinhardt, E. Peters, T. W. Hänsch, and T. Udem, “Two-photon direct frequency comb spectroscopy with chirped pulses,” *Physical Review A*, vol. 81, p. 033427, 2010.
- [69] M. Levenson and N. Bloembergen, “Observation of Two-Photon Absorption without Doppler Broadening on the 3S-5S Transition in Sodium Vapor,” *Physical Review Letters*, vol. 32, p. 645, 1974.
- [70] F. Biraben, B. Cagnac, and G. Grynberg, “Experimental Evidence of Two-Photon Transition without Doppler Broadening,” *Physical Review Letters*, vol. 32, p. 643, 1974.
- [71] P. Fendel, S. D. Bergeson, T. Udem, and T. W. Hänsch, “Two-photon frequency comb spectroscopy of the 6s-8s transition in cesium,” *Optics Letters*, vol. 32, p. 701, 2007.
- [72] J. Morgenweg, I. Barmes, and K. S. E. Eikema, “Ramsey-comb spectroscopy with intense ultrashort laser pulses,” *Nature Physics*, vol. 10, p. 30, 2013.
- [73] A. M. Weiner, “Femtosecond pulse shaping using spatial light modulators,” *Review of Scientific Instruments*, vol. 71, p. 1929, 2000.
- [74] D. Yelin, D. Meshulach, and Y. Silberberg, “Adaptive femtosecond pulse compression,” *Optics letters*, vol. 22, p. 1793, 1997.
- [75] R. Judson and H. Rabitz, “Teaching lasers to control molecules,” *Physical Review Letters*, vol. 68, p. 1500, 1992.
- [76] T. Baumert, T. Brixner, V. Seyfried, M. Strehle, and G. Gerber, “Femtosecond pulse shaping by an evolutionary algorithm with feedback,” *Applied Physics B: Lasers and Optics*, vol. 65, p. 779, 1997.

- [77] A. Assion, "Control of Chemical Reactions by Feedback-Optimized Phase-Shaped Femtosecond Laser Pulses," *Science*, vol. 282, p. 919, 1998.
- [78] J. L. Herek, W. Wohlleben, R. J. Cogdell, D. Zeidler, and M. Motzkus, "Quantum control of energy flow in light harvesting.," *Nature*, vol. 417, p. 533, 2002.
- [79] T. Brixner and G. Gerber, "Femtosecond polarization pulse shaping.," *Optics letters*, vol. 26, p. 557, 2001.
- [80] T. Brixner, G. Krampert, T. Pfeifer, R. Selle, G. Gerber, M. Wollenhaupt, O. Graefe, C. Horn, D. Liese, and T. Baumert, "Quantum Control by Ultrafast Polarization Shaping," *Physical Review Letters*, vol. 92, p. 208301, 2004.
- [81] L. Polachek, D. Oron, and Y. Silberberg, "Full control of the spectral polarization of ultrashort pulses.," *Optics Letters*, vol. 31, p. 631, 2006.
- [82] E. Frumker and Y. Silberberg, "Phase and amplitude pulse shaping with two-dimensional phase-only spatial light modulators," *Journal of the Optical Society of America B*, vol. 24, p. 2940, 2007.
- [83] R. Ell, U. Morgner, F. X. Kärtner, J. G. Fujimoto, E. P. Ippen, V. Scheuer, G. Angelow, T. Tschudi, M. J. Lederer, A. Boiko, and B. Luther-Davies, "Generation of 5-fs pulses and octave-spanning spectra directly from a Ti:sapphire laser.," *Optics letters*, vol. 26, p. 373, 2001.
- [84] L.-J. Chen, A. J. Benedick, J. R. Birge, M. Y. Sander, and F. Kärtner, "Octave-spanning, dual-output 2.166 GHz Ti:sapphire laser.," *Optics express*, vol. 16, p. 20699, 2008.
- [85] T. A. Birks, J. C. Knight, P. S. Russell, and D. M. Atkin, "All-silica single-mode optical fiber with photonic crystal cladding," *Optics Letters*, vol. 22, p. 484, 1997.
- [86] N. G. Broderick, T. M. Monro, P. J. Bennett, and D. J. Richardson, "Nonlinearity in holey optical fibers: measurement and future opportunities.," *Optics letters*, vol. 24, p. 1395, 1999.
- [87] J. K. Ranka, R. S. Windeler, and a. J. Stentz, "Visible continuum generation in air-silica microstructure optical fibers with anomalous dispersion at 800 nm.," *Optics letters*, vol. 25, p. 25, 2000.
- [88] A. Baltuska, T. Udem, M. Uiberacker, M. Hentschel, E. Goulielmakis, C. Gohle, R. Holzwarth, V. S. Yakovlev, A. Scrinzi, T. W. Hänsch, and F. Krausz, "Attosecond control of electronic processes by intense light fields.," *Nature*, vol. 421, p. 611, 2003.

-
- [89] I. Coddington, W. C. Swann, L. Nenadovic, and N. R. Newbury, “Rapid and precise absolute distance measurements at long range,” *Nature Photonics*, vol. 3, p. 351, 2009.
- [90] M. Shapiro, “Real-Time Dependence of Photodissociation and Continuum Raman Experiments,” *J. Phys. Chem*, vol. 97, p. 7396, 1993.
- [91] D. Meshulach and Y. Silberberg, “Coherent quantum control of multiphoton transitions by shaped ultrashort optical pulses,” *Physical Review A*, vol. 60, p. 1287, 1999.
- [92] A. Präkelt, M. Wollenhaupt, C. Sarpe-Tudoran, and T. Baumert, “Phase control of a two-photon transition with shaped femtosecond laser-pulse sequences,” *Physical Review A*, vol. 70, p. 063407, 2004.
- [93] B. Broers, H. van Linden van den Heuvell, and L. Noordam, “Efficient population transfer in a three-level ladder system by frequency-swept ultrashort laser pulses,” *Physical Review Letters*, vol. 69, p. 2062, 1992.
- [94] B. Chatel, J. Degert, and B. Girard, “Role of quadratic and cubic spectral phases in ladder climbing with ultrashort pulses,” *Physical Review A*, vol. 70, p. 053414, 2004.
- [95] M. Bellini, A. Bartoli, and T. W. Hänsch, “Two-photon Fourier spectroscopy with femtosecond light pulses,” *Optics letters*, vol. 22, p. 540, 1997.
- [96] V. Blanchet, C. Nicole, M.-A. Bouchene, and B. Girard, “Temporal Coherent Control in Two-Photon Transitions: From Optical Interferences to Quantum Interferences,” *Physical Review Letters*, vol. 78, p. 2716, 1997.
- [97] L. Vasilenko, V. Chebotayev, and A. Shishaev, “Line Shape of Two-Photon Absorption in a Standing-Wave Field in a Gas,” *Jetp Letters*, vol. 12, p. 113, 1970.
- [98] P. J. Mohr, B. N. Taylor, and D. B. Newell, “CODATA recommended values of the fundamental physical constants: 2006,” *Reviews of Modern Physics*, vol. 80, p. 633, 2008.
- [99] M. Fischer, N. Kolachevsky, M. Zimmermann, R. Holzwarth, T. Udem, T. W. Hänsch, M. Abgrall, J. Grunert, I. Maksimovic, S. Bize, H. Marion, F. P. D. Santos, P. Lemonde, G. Santarelli, P. Laurent, A. Clairon, C. Salomon, M. Haas, U. D. Jentschura, and C. H. Keitel, “New Limits on the Drift of Fundamental Constants from Laboratory Measurements,” *Physical Review Letters*, vol. 92, p. 230802, 2004.

- [100] T. Hänsch, S. Lee, R. Wallenstein, and C. Wieman, “Doppler-Free Two-Photon Spectroscopy of Hydrogen 1S-2S,” *Physical Review Letters*, vol. 34, p. 307, 1975.
- [101] G. D. Dickenson, M. L. Niu, E. J. Salumbides, J. Komasa, K. S. E. Eikema, K. Pachucki, and W. Ubachs, “Fundamental Vibration of Molecular Hydrogen,” *Physical Review Letters*, vol. 110, p. 193601, 2013.
- [102] V. Meyer, S. Bagayev, P. Baird, P. Bakule, M. Boshier, A. Breitrück, S. Cornish, S. Dychkov, G. Eaton, A. Grossmann, D. Hübl, V. Hughes, K. Jungmann, I. Lane, Y.-W. Liu, D. Lucas, Y. Matyugin, J. Merkel, G. zu Putlitz, I. Reinhard, P. Sandars, R. Santra, P. Schmidt, C. Scott, W. Toner, M. Towrie, K. Träger, L. Willmann, and V. Yakhontov, “Measurement of the 1s-2s Energy Interval in Muonium,” *Physical Review Letters*, vol. 84, p. 1136, 2000.
- [103] T. Rosenband, D. B. Hume, P. O. Schmidt, C. W. Chou, A. Brusch, L. Lorini, W. H. Oskay, R. E. Drullinger, T. M. Fortier, J. E. Stalnaker, S. A. Diddams, W. C. Swann, N. R. Newbury, W. M. Itano, D. J. Wineland, and J. C. Bergquist, “Frequency ratio of Al^+ and Hg^+ single-ion optical clocks; metrology at the 17th decimal place.,” *Science*, vol. 319, p. 1808, 2008.
- [104] D. Z. Kandula, C. Gohle, T. J. Pinkert, W. Ubachs, and K. S. E. Eikema, “Extreme Ultraviolet Frequency Comb Metrology,” *Physical Review Letters*, vol. 105, p. 063001, 2010.
- [105] J. Bjorkholm and P. Liao, “Line shape and strength of two-photon absorption in an atomic vapor with a resonant or nearly resonant intermediate state,” *Physical Review A*, vol. 14, p. 751, 1976.
- [106] Y. V. Baklanov and V. P. Chebotayev, “Narrow resonances of two-photon absorption of super-narrow pulses in a gas,” *Applied Physics*, vol. 12, p. 97, 1977.
- [107] A. Ozawa and Y. Kobayashi, “Chirped-pulse direct frequency-comb spectroscopy of two-photon transitions,” *Physical Review A*, vol. 86, p. 022514, 2012.
- [108] I. Barmes, S. Witte, and K. S. E. Eikema, “Spatial and spectral coherent control with frequency combs,” *Nature Photonics*, vol. 7, p. 38, 2012.
- [109] H.-C. Chui, M.-S. Ko, Y.-W. Liu, J.-T. Shy, J.-L. Peng, and H. Ahn, “Absolute frequency measurement of rubidium 5S-7S two-photon transitions with a femtosecond laser comb,” *Optics Letters*, vol. 30, p. 842, 2005.

-
- [110] M. Stowe, M. Thorpe, A. Pe'er, J. Ye, J. Stalnaker, V. Gerginov, and S. Diddams, "Direct frequency comb spectroscopy," *Advances In Atomic, Molecular, and Optical Physics*, vol. 55, p. 1, 2008.
- [111] R.-B. Li, L. Zhou, J. Wang, and M.-S. Zhan, "Measurement of the quadratic Zeeman shift of ^{85}Rb hyperfine sublevels using stimulated Raman transitions," *Optics Communications*, vol. 282, p. 1340, 2009.
- [112] E. Arimondo, M. Inguscio, and P. Violino, "Experimental determinations of the hyperfine structure in the alkali atoms," *Reviews of Modern Physics*, vol. 49, p. 31, 1977.
- [113] A. M. Weiner, D. E. Leaird, G. P. Wiederrecht, and K. A. Nelson, "Femtosecond pulse sequences used for optical manipulation of molecular motion.," *Science*, vol. 247, p. 1317, 1990.
- [114] B. Broers, H. van Linden van den Heuvell, and L. Noordam, "Large interference effects of small chirp observed in two-photon absorption," *Optics Communications*, vol. 91, p. 57, 1992.
- [115] R. Bartels, S. Backus, E. Zeek, L. Misoguti, G. Vdovin, I. Christov, M. Murnane, and H. Kapteyn, "Shaped-pulse optimization of coherent emission of high-harmonic soft X-rays," *Nature*, vol. 406, p. 164, 2000.
- [116] J. M. Dela Cruz, I. Pastirk, M. Comstock, V. V. Lozovoy, and M. Dantus, "Use of coherent control methods through scattering biological tissue to achieve functional imaging.," *Proceedings of the National Academy of Sciences of the United States of America*, vol. 101, p. 16996, 2004.
- [117] E. Papagiakoumou, F. Anselmi, A. Bègue, V. De Sars, J. Glückstad, E. Y. Isacoff, and V. Emiliani, "Scanless two-photon excitation of channelrhodopsin-2," *Nature Methods*, vol. 7, p. 848, 2010.
- [118] V. I. Prokhorenko, A. M. Nagy, S. A. Waschuk, L. S. Brown, R. R. Birge, and R. J. D. Miller, "Coherent control of retinal isomerization in bacteriorhodopsin.," *Science*, vol. 313, p. 1257, 2006.
- [119] P. Nuernberger, D. Wolpert, H. Weiss, and G. Gerber, "Femtosecond quantum control of molecular bond formation," *Proceedings of the National Academy of Sciences of the United States of America*, vol. 107, p. 10366, 2010.
- [120] S. T. Cundiff and A. M. Weiner, "Optical arbitrary waveform generation," *Nature Photonics*, vol. 4, p. 760, 2010.

- [121] M. S. Kirchner and S. A. Diddams, "Grism-based pulse shaper for line-by-line control of more than 600 optical frequency comb lines.," *Optics letters*, vol. 35, p. 3264, 2010.
- [122] J. E. Stalnaker, S. L. Chen, M. E. Rowan, K. Nguyen, T. Pradhananga, C. A. Palm, and D. F. J. Kimball, "Velocity-selective direct frequency-comb spectroscopy of atomic vapors," *Physical Review A*, vol. 86, p. 033832, 2012.
- [123] A. H. Zewail, "Femtochemistry: Atomic-Scale Dynamics of the Chemical Bond ," *The Journal of Physical Chemistry A*, vol. 104, p. 5660, 2000.
- [124] P. Brumer and M. Shapiro, "Laser control of molecular processes.," *Annual review of physical chemistry*, vol. 43, p. 257, 1992.
- [125] A. M. Weiner, D. E. Leaird, J. S. Patel, and J. R. Wullert, "Programmable femtosecond pulse shaping by use of a multielement liquid-crystal phase modulator," *Optics Letters*, vol. 15, p. 326, 1990.
- [126] F. Langhojer, D. Cardoza, M. Baertschy, and T. Weinacht, "Gaining mechanistic insight from closed loop learning control: the importance of basis in searching the phase space.," *The Journal of chemical physics*, vol. 122, p. 14102, 2005.
- [127] C. Trallero-Herrero, J. Cohen, and T. Weinacht, "Strong-Field Atomic Phase Matching," *Physical Review Letters*, vol. 96, p. 063603, 2006.
- [128] J. Roslund, M. Roth, and H. Rabitz, "Laboratory observation of quantum control level sets," *Physical Review A*, vol. 74, p. 043414, 2006.
- [129] P. van der Walle, H. Offerhaus, J. Herek, and A. Jafarpour, "Tailoring a coherent control solution landscape by linear transforms of spectral phase basis," *Optics Express*, vol. 18, p. 973, 2010.
- [130] M. Wollenhaupt, A. Präkelt, C. Sarpe-Tudoran, D. Liese, and T. Baumert, "Quantum control and quantum control landscapes using intense shaped femtosecond pulses," *Journal of Modern Optics*, vol. 52, p. 2187, 2005.
- [131] N. Dudovich, D. Oron, and Y. Silberberg, "Single-pulse coherently controlled nonlinear Raman spectroscopy and microscopy.," *Nature*, vol. 418, p. 512, 2002.
- [132] F. Träger, ed., *Springer Handbook of Lasers and Optics*. New York, NY: Springer New York, 2007.

- [133] H. A. Rabitz, M. M. Hsieh, and C. M. Rosenthal, “Quantum optimally controlled transition landscapes,” *Science*, vol. 303, p. 1998, 2004.
- [134] T. Bayer, M. Wollenhaupt, and T. Baumert, “Strong-field control landscapes of coherent electronic excitation,” *Journal of Physics B: Atomic, Molecular and Optical Physics*, vol. 41, p. 074007, 2008.
- [135] J. Roslund and H. Rabitz, “Experimental quantum control landscapes: Inherent monotonicity and artificial structure,” *Physical Review A*, vol. 80, p. 013408, 2009.

List of Publications

- T. J. Pinkert, D. Z. Kandula, C. Gohle, I. Barmes, J. Morgenweg, and K. S. E. Eikema, Widely tunable extreme UV frequency comb generation, *Optics Express* **36**, 2026 (2011).
- I. Barmes, S. Witte, and K. S. E. Eikema, Spatial and spectral coherent control with frequency combs, *Nature Photonics* **7**, 38 (2012).
- I. Barmes, S. Witte, and K. S. E. Eikema, High-Precision Spectroscopy with Counterpropagating Femtosecond Pulses, *Physical Review Letters* **111**, 023007 (2013).
- J. Morgenweg I. Barmes, and K. S. E. Eikema, Ramsey-comb spectroscopy with intense ultrashort laser pulses, *Nature Physics* **10**, 30 (2014).

Summary

The invention of the laser has provided scientists with an excellent tool to measure and control atomic and molecular systems. In the early days of laser physics, cw and pulsed lasers were used for different types of applications. Using a single-mode laser, scientists were able to measure the absolute frequency of atomic and molecular transitions with extreme precision. This has led to the development of state-of-the-art atomic clocks and stringent tests of fundamental theories. On the other hand, so called mode-locked lasers provide a broad spectral range and a short pulse duration, which can be used to achieve a high temporal resolution. Together with pulse shaping techniques, broadband pulses can be used to control and manipulate excitation of atoms and molecules through quantum interference effects. At the turn of the 21th century, a new type of mode-locked laser was invented that brought these two worlds together. Named after its spectral properties, it is called a frequency comb laser. It emits a spectrum of equidistant modes (like a comb), which interfere such that the intensity of the output looks like an infinite train of regular ultrashort pulses. In this way one can combine the properties of a broad bandwidth of ultrashort pulses with high spectral resolution.

In the work presented in this thesis we make use of the unique properties of the frequency comb laser to control and manipulate the excitation of atomic transitions. Our method involves the excitation of atomic transitions in a counterpropagating geometry with shaped comb pulses. The broad bandwidth of these pulses allows us to excite the transition via multiple quantum pathways, and the control over the shape of the pulses via the spectral phase enables the manipulation of the quantum interference between the various pathways. Exciting these transitions in a counterpropagating geometry not only results in high-precision spectroscopy measurements, but also enables high-resolution control over resonant and nonresonant pathways. A more detailed motivation for our work is presented in Chapter 1.

Chapter 2 provides a solid theoretical background of the methods used in this thesis. We start with the propagation of electromagnetic waves in vacuum and linear media, and derive how ultrashort laser pulses are affected by propagating through dispersive materials. We continue with other pulse shaping techniques and derive the temporal and spectral properties of shaped pulses when applying sinusoidal and a V-shaped spectral phase masks. The discussion is then extended from single pulses to pulse trains and we discuss how the

coherent addition of ultrashort pulses results in a comb of equidistant narrow modes. This theory chapter is concluded with a mathematical description of light-matter interaction for two and three level atoms and a discussion of the differences between resonant and nonresonant two-photon absorption (TPA). The main experimental result of this thesis is the manipulation of two-photon signal when excited by counterpropagating frequency comb pulses. To predict the influence of pulse shaping on the two-photon signal we use the analogy between excitation in a copropagating and counterpropagating geometries. In Chapter 3 we investigate the effect of pulse shaping on the signal in the copropagating geometry for resonant and nonresonant TPA. A V-shaped spectral phase mask is applied, which splits each pulse into a red and blue subpulse. We show that the time delay between the pulse pair, and the time delay between the red and blue subpulses have a strong influence on both the overall shape and the oscillation of the signal. We also discuss the contributions of photon pairs from different pulses (and subpulses) and how the interference between these pathways leads to the total signal. The insights gained from these results are used in later chapters to model the counterpropagating signal.

In Chapter 4 we use pulse shaping on counterpropagating frequency comb pulses in order to reduce the dominant Doppler-broadened background. We show that applying a V-shaped phase mask completely eliminates the background signal and therefore results in an excellent signal-to-noise ratio. The usability of this technique is illustrated by performing high-precision spectroscopy on the $5S \rightarrow 7S$ transition in Rb, with about one order of magnitude improved frequency accuracy compared to previous measurements.

In Chapter 5 we generalize the concept presented in the previous chapter to arbitrary pulse shapes. We extend the model from Chapter 3 to the counterpropagating geometry and derive an equation to predict the excitation pattern resulting from counterpropagating shaped pulses. This equation reveals a number of intriguing symmetry properties of the signal, which we experimentally demonstrate by applying a sinusoidal spectral phase mask. It is shown that small changes in the spectral phase mask lead to dramatically different excitation patterns, with excellent agreement between the experimental results and the numerical simulations.

For nonresonant TPA all pairs of frequencies that participate in the excitation have approximately the same weight in the transition amplitude. However, in resonant TPA, pairs of photons where one of the photons has a frequency near an intermediate state lead to a larger excitation amplitude. Moreover, the contribution of the resonant pathway (a pair of photons that is also resonant with the intermediate state) has a phase shift with respect to the nonresonant pathways. When excited in the counterpropagating geometry the different pathways also behave differently to the Doppler effect. In Chapter 6 we discuss these aspects and experimentally show that the frequency comb parameters can be

used to discriminate between resonant and nonresonant pathways. By applying a V-shaped spectral phase mask we show that the quantum interference between the resonant and nonresonant pathways becomes spatially dependent. In coherent control experiments the spectral phase mask can potentially have hundreds of degrees of freedom and can assume almost any shape. Searching in such a high-dimensional space is impractical and does not necessarily provide useful insights about the physical system. The phase mask is therefore usually parameterized into a function with a limited set of control parameters, such as the V-shaped phase and the sinusoidal phase used in this thesis. In Chapter 7 we extend the concept of sinusoidal phase masks to arbitrary periodic phase modulation. We show that any periodic spectral phase mask results in a sequence of subpulses where the amplitude of the subpulses depends on the coefficients of the Fourier decomposition of the periodic function. This approach provides a larger set of control parameters for searching through a high-dimensional control landscape. This is illustrated by calculating the non-resonant TPA signal with 2 and 3 control parameters where we show how adding control parameters provides a better understanding of the control landscape.

Samenvatting

De ontwikkeling van de laser heeft onderzoekers in de gelegenheid gesteld om atomaire en moleculaire systemen te meten en manipuleren. In de vroege jaren van laserfysica werden cw en gepulseerde lasers gebruikt voor verschillende toepassingen. Aan de ene kant, met het gebruik van een single-mode laser, konden onderzoekers de absolute frequentie van atomaire en moleculaire overgangen met zeer hoge nauwkeurigheid bepalen. Dit heeft geleid tot de ontwikkeling van atoomklokken en nauwkeurige testen van fundamentele theorieën. Aan de andere kant produceren de zogenaamde mode-locked lasers een grote bandbreedte en een korte pulstijd, die gebruikt kunnen worden om een hoge temporele resolutie te bereiken. Gecombineerd met "pulse-shaping" technieken kunnen deze breedbandige pulsen, door middel van quantum-interferentie, gebruikt worden om de excitatie van atomen en moleculen te manipuleren. In het begin van de 21e eeuw is een nieuw type mode-locked laser gerealiseerd die deze twee werelden samenbracht. De output van deze zogenaamde frequentiekam laser is een reeks van pulsen die op zo'n manier met elkaar interfereren dat het spectrum van deze laser een verzameling van equidistante modes bevat. Hierdoor kunnen wetenschappers de eigenschappen van breedbandige lasers combineren met hoge spectrale resolutie.

In dit proefschrift maken we gebruik van de unieke eigenschappen van de frequentiekam om de excitatie van atomaire overgangen te manipuleren. In onze methode worden atomaire overgangen geëxciteerd door "shaped" femtoseconde pulsen uit tegengestelde richtingen. De grote bandbreedte van deze pulsen zorgt ervoor dat de overgang tegelijk geëxciteerd wordt via meerdere quantum-paden. Verder zorgt de toepassing van spectrale fasemanipulatie voor controle over de quantum-interferentie van de verschillende mogelijke paden. Het exciteren van deze overgangen in een tegengestelde (counterpropagating) geometrie resulteerde zowel in hoge-precisie spectroscopie als "quantum control" met hoge resolutie. Een gedetailleerde onderbouwing van ons werk wordt in hoofdstuk 1 gepresenteerd.

Hoofdstuk 2 bevat de theoretische achtergrond voor de methoden die gebruikt worden in dit proefschrift. We beginnen met de voortbeweging van elektromagnetische golven in vacuüm en lineaire media. Hiervoor wordt wiskundig afgeleid hoe ultrakorte laserpulsen beïnvloed worden als gevolg van de voortbeweging door dispersieve materialen. Vervolgens worden andere vormen van spectrale fase-manipulatie beschreven zoals de sinusoidale en V-vormige spectrale fase

en de resulterende temporele eigenschappen. We breiden deze analyse uit naar lange reeksen van pulsen en laten zien hoe de coherente toevoeging van pulsen resulteert in een kam van equidistante smalle modes. Dit theoriehoofdstuk wordt afgesloten met een wiskundige beschrijving van de interactie tussen licht en materie in 2- en 3-niveau atomen en een discussie over het verschil tussen resonante en niet-resonante twee-foton absorptie (TPA).

Het belangrijkste experimentele resultaat van dit proefschrift is de manipulatie van het twee-foton signaal wanneer het geëxciteerd wordt door frequentiekam pulsen uit tegengestelde richtingen. Om de invloed van de gevormde pulsen op het twee-foton signaal te voorspellen, gebruiken we een analogie tussen excitatie in verschillende propagatie geometrieën. In hoofdstuk 3 bestuderen we het effect van "pulse-shaping" op excitatie door puls-paren die in dezelfde richting bewegen voor resonante en niet-resonante TPA. Een V-vormige spectrale fase wordt toegepast, waardoor elke puls opgesplitst wordt in een "rode" en "blauwe" subpuls. We laten zien dat de vertraging tussen de pulsparen en de vertraging tussen de "rode" en "blauwe" subpulsen een sterke invloed hebben op zowel de algehele vorm als de oscillatie van het signaal. We bespreken ook de bijdrage van fotonparen van verschillende pulsen (en subpulsen) en hoe de interferentie tussen deze paden tot het totale signaal leiden. Het inzicht verkregen uit deze resultaten wordt in verdere hoofdstukken gebruikt om een model te ontwikkelen voor de excitatie door frequentiekampulsen uit tegengestelde richtingen.

In hoofdstuk 4 gebruiken we "pulse-shaping" op frequentiekam pulsen uit tegengestelde richtingen om de dominante Doppler-verbrede achtergrond (ruis) te reduceren. We laten zien dat het aanbrengen van een V-vormige spectrale fase het achtergrondsignaal volledig elimineert en derhalve resulteert in een uitstekende signaal/ruis verhouding. De bruikbaarheid van deze techniek wordt gedemonstreerd door hoge-precisie spectroscopie uit te voeren op de $5S \rightarrow 7S$ overgang in Rb. Daarbij werd een verbetering van de nauwkeurigheid van het bepalen van de absolute frequentie gerealiseerd met een factor 10, vergeleken met eerdere metingen.

In hoofdstuk 5 wordt het principe uit hoofdstuk 4 gegeneraliseerd voor pulsen met een willekeurige vorm. Het model dat in hoofdstuk 3 gepresenteerd is, wordt aangepast voor pulsen uit tegengestelde richtingen. De voorspelling van het TPA signaal onthult een aantal intrigerende symmetrie-eigenschappen van het signaal, die we experimenteel demonstreren door een sinusoidale spectrale fase aan te brengen. We laten zien dat kleine veranderingen in de spectrale fase tot drastische verschillende excitatiepatronen leiden, met een uitstekende overeenstemming tussen de experimentele resultaten en de numerieke simulaties.

In het geval van niet-resonante TPA hebben alle frequentieparen die deelnemen in de excitatie ongeveer hetzelfde aandeel in de transitie amplitude. Daar-

entegen, in resonante TPA leiden de fotonparen waar een van de fotonen een frequentie heeft vlak bij een tussenresonantie, tot een grotere excitatie amplitude. Bovendien heeft de bijdrage van het resonante pad (een fotonpaar dat ook resonant is met de tussenresonantie) en faseverschuiving ten opzichte van de niet-resonante paden. In de situatie van pulsen uit tegengestelde richtingen reageren de verschillende paden ook anders op het Doppler-effect. In hoofdstuk 6 bespreken we deze aspecten en laten we experimenteel zien dat de parameters van de frequentiekam gebruikt kunnen worden om onderscheid te maken tussen de resonante en niet-resonante paden. Door een V-vormige spectrale fase toe te passen, laten we zien dat de quantum interferentie tussen de resonante en niet-resonante paden plaats afhankelijk wordt.

In coherent control experimenten kan de spectrale fase mogelijk honderden vrijheidsgraden hebben. Het zoeken in zo'n hoog dimensionale ruimte is onpraktisch en geeft niet noodzakelijkerwijze meer inzicht over het fysische systeem. Daarom wordt de spectrale fase vaak geparametriseerd tot een functie met een beperkt aantal vrijheidsgraden, zoals de V-vormige fase en de sinusoidale fase gebruikt in dit proefschrift. In hoofdstuk 7 wordt het concept van sinusoidale fase uitgebreid tot arbitraire periodieke fasemodulatie. We laten zien dat iedere periodieke spectrale fase resulteert in een reeks van subpulsen waarvan de amplitude van de subpulsen afhankelijk is van de coëfficiënten van de Fourier transformatie van de periodieke functie. Deze benadering biedt een groter aantal controleparameters voor het zoeken door een hoog-dimensionaal landschap. Dit wordt geïllustreerd door de berekening van het niet-resonante TPA signaal met 2 en 3 controleparameters, waar we laten zien hoe de toevoeging van controleparameters beter inzicht geeft in het controlelandschap.

Acknowledgements

First and foremost I would like to thank my promotor Kjeld Eikema. Kjeld, to me you are what science is all about. Endless curiosity, perseverance and an uncompromising drive to figure out how things work. I feel privileged to have been a part of your team and hope that I've contributed to your "Master Plan" without pushing you over the edge (as you frequently, jokingly I hope, said). I want to thank you for allowing me to start my Ph.D later than planned due to all kind of circumstances and giving me the freedom to find my own path. I've learned a great deal from you and I wish you all the best in your future adventures.

A big thank you to my copromotor Stefan Witte who guided me and showed me the way around the lab (by the way I hope you don't mind that I abused your pulse shaper for low-intensity applications). You were next to me at some of the important moments of my Ph.D period. I remember how we were both amazed seeing the signal from the sinusoidal phase for the first time. Definitely an image that will stay with me for a long time, and important enough to put on the back of my thesis. Oh, and by the way thank you for making the cover of my thesis so cool.

I was part of the Atomic Physics group in a very special time. The group was expanding rapidly and producing fascinating scientific output. I would like to thank Wim Ubachs and the other senior members of the group for creating an atmosphere where young researchers can learn and be continuously challenged. This has attracted people from many different countries to come to Amsterdam and be part of this group. We had great fun in the labs, meeting rooms, pubs and ski slopes. I'm very happy that many of you remain my friends even though you live on the other side of the world.

Last but not least I want to thank my family and friends for their support. Listening to me going on and on about lasers, atoms and other stuff you don't care about.

To Raïna, my love, the mother of my children and my future wife. What I have to say to you I will say a day after my defense.

